THESIS FOR THE DEGREE OF DOCTOR OF PHILOSOPHY

Nanofluidic Scattering Microscopy and Spectroscopy for Single Particle Catalysis

BJÖRN ALTENBURGER

CHALMERS
UNIVERSITY OF TECHNOLOGY

Department of Physics

CHALMERS UNIVERSITY OF TECHNOLOGY

Gothenburg, Sweden 2024

Department of Physics
Chalmers University of Technology
SE-412 96 Gothenburg
Sweden
Telephone + 46 (0)31-772 1000

Cover:
Artistic rendering of an array of parallel nanochannels, each decorated with a lithographic gold nanoparticle. Fluorescein, borohydride and water molecules flow over the nanoparticles. Incident white light is scattered at a different color from the nanochannel before and after the particle.

Nanofluidic Scattering Microscopy and Spectroscopy for Single Particle Catalysis

Björn Altenburger
Department of Physics
Chalmers University of Technology

ABSTRACT

Nanoparticles are a fundamental asset in modern society, and a cornerstone in global industries where they contribute significantly to the path towards sustainable energy and products. Their ability to facilitate and steer chemical reactions is studied in the field of heterogeneous catalysis, where these tiny particles are characterized regarding their activity and selectivity. However, the characterization is often conducted on large ensembles of particles, thereby disregarding their structural heterogeneity, which possibly leads to erroneous structure-function correlations. Since it is one goal of catalysis research to find "superparticles" with exceptional performance, the need for dedicated single particle studies where the influence of, e.g., shape, size and surface structure is investigated in detail, is obvious.

Methods like fluorescence microscopy, X-ray diffraction/scattering, electron microscopy and plasmonic sensing are commonly used for single particle investigations in catalysis. These methods detect electrons or photons that carry information either on the reactant molecules, the product molecules, changes to the catalyst particle itself or the particle surrounding. However, none of these methods provides direct single particle activity information without either using plasmonic enhancement effects that may also impact the studied reaction itself and limit the range of catalyst materials that can be studied, or using fluorescence that limits reaction conditions to ultralow concentrations and to a narrow range of reactions.

The overarching goal of the work presented in this thesis has been to develop an optical microscopy technique that can quantitatively measure catalytic activity, and in the longer term even selectivity, of a single nanoparticle, without the limitations of existing single particle techniques. At the core of this method - Nanofluidic Scattering Microscopy - are nanofluidic channels that can accurately control the transport of molecules to and from a single, catalytically active, particle localized inside a channel. As a second key trait, the unique light scattering properties of nanochannels render them highly sensitive to refractive index changes of the fluid inside them. Hence, when a catalytic reaction alters the molecular composition of the fluid in a nanochannel, its light scattering characteristics change and reveal in this way the catalytic performance of the nanoparticle, which here is demonstrated for H_2O_2 decomposition over on single Pt particles. Furthermore, resolving the scattered light spectrally, as I do in Nanofluidic Scattering Spectroscopy, spectral fingerprints of a catalytic reaction can be resolved, as demonstrated for the catalytic reduction of fluorescein on a single Au nanoparticle.

In the wake of these developments, I also have developed a new fluidic platform, chip holder and microscopy setup to harness the full potential of micro- and nanofluidics in combination with optical microscopy and spectroscopy applied to single particle catalysis investigations.

Keywords: single particle catalysis, dark-field scattering microscopy, heterogeneous catalysis, microfluidics, nanofluidics, spectroscopy, setup development

IV

All we have to decide is what to do with the time

that is given us.

J.R.R. Tolkien, *The Fellowship of the Ring*

LIST OF APPENDED PAPERS

This thesis is the basis for the work presented in the following papers:

Paper I

Nanofluidic Scattering Microscopy of Single Colloidal Platinum Nanoparticle H_2O_2 Decomposition Catalysis

Björn Altenburger, Carl Andersson, Sune Levin, Fredrik Westerlund, Joachim Fritzsche, and Christoph Langhammer

ACS Nano 2023, 17, 21, 21030–21043.

Paper II

Vis Spectroscopy of Liquid Solutes from Femto- to Attoliter Volumes inside a Single Nanofluidic Channel

Björn Altenburger, Joachim Fritzsche, and Christoph Langhammer

Under revision after first peer-review for publication in ACS Nano

Paper III

Femtoliter Batch Reactors for Nanofluidic Scattering Spectroscopy Analysis of Catalytic Reactions on Single Nanoparticles

Björn Altenburger, Joachim Fritzsche, and Christoph Langhammer

In Manuscript

Paper IV

A temperature-controlled chip holder with integrated electrodes for nanofluidic scattering spectroscopy on highly integrated nanofluidic systems

Björn Altenburger, Joachim Fritzsche, and Christoph Langhammer

In Manuscript

MY CONTRIBUTION TO APPENDED PAPERS

Paper I

I performed all nanofluidic scattering microscopy experiments together with the corresponding data evaluation and wrote the first draft of the manuscript.

Paper II

I designed the fluidic chip layout and performed the nanofluidic scattering spectroscopy experiments. In addition, I did the data evaluation and wrote the first draft of the manuscript.

Paper III

I designed the fluidic chip and developed the concept of the nanochannel batch reactor. I performed the corresponding experiments, did the data evaluation and wrote the first draft of the manuscript.

Paper IV

I designed the new fluidic chuck and chip in correspondence with the manufacturer and assembled the experimental setup. I did the experiments and data evaluation and wrote the first draft of the manuscript.

x

TABLE OF CONTENTS

1 INTRODUCTION

Catalysis is for many maybe an unknown word at first. However, after some thought it is often connected to the three-way catalytic converter installed on every gasoline fueled combustion engine driven vehicle[1]. Interestingly also this very thought itself is only possible thanks to catalysis, since catalytic processes occur constantly in the bodies of living organisms, like ourselves, performed by enzymes[2]. Unbeknownst to this fact, humans have performed controlled chemical reactions since ancient times. It is only since rather recently[3] in terms of human history that we discovered that certain forms of matter can greatly facilitate a reaction without being consumed or integrated in the products formed. This key property of a catalyst material that has coined the term "Catalysis" [4]. The word itself is derived from the Greek "κατα-λύειν" which can be translated as "to unbind" or "to take down", thereby describing what a catalyst does on a molecular level, as it opens up molecular bonds and binds species (temporally) to its surface. By doing so, it provides a reaction path for the direct reaction between two molecules. This alternative path often requires less energy and thereby accelerates the chemical reaction or even alters the outcome of the reaction in terms of products formed by changing the so-called reaction selectivity.

Since its humble beginnings in the late 18th century, catalysis has today developed into a large global industry. Estimates from 2023 put the global catalyst market size in the range of \$31 billion[5], and the corresponding catalytic products make up around 90% of the products of the chemical industry as a whole[6]. The most prominent and impactful industrial catalytic process is without doubt the binding of atmospheric nitrogen[7] (N_2) into ammonia (NH_3) by the Haber-Bosch process, which forms the basis of artificial fertilizer that has enabled the massive growth in human population in the last century. In addition to the aforementioned catalytic converters that remove toxic species from exhaust fumes of combustion processes, catalytic reactions are critical for the production of fuels and fine chemicals that find application in, e.g. medicine or plastics. Finally, catalysis is also a key ingredient in carbon-free energy (storage) technologies, such as synthetic fuels, batteries or hydrogen energy technologies[8].

The core of all these technical applications is always the catalyst material itself, which often is a metal in the solid state, while the reactants are in the gas or liquid phase. This distinguishes so-called heterogeneous catalysis from homogeneous catalysis[9], where the catalyst is in the same phase as the reactants, as it is the case for enzymatic reactions in solution. The metals used for catalysts require special chemical properties that facilitate the specific reaction at hand, as for example Iron (Fe) is used in the above-mentioned Haber-Bosch process. Even more precious and rare metals, such as Platinum (Pt), Palladium (Pd) or Rhodium (Rh) are more often employed as catalysts. However, since their total amount in the earth's crust is limited and the corresponding extraction process is resource intensive[10], it is essential that these metals are used effectively. Since it is the surface of the catalyst where the catalytic reaction occurs, a widely used approach to maximize this surface, while at the same time minimizing the total mass of catalyst material, is to deploy the catalyst in nanoparticle form. This means that the active catalyst material is dispersed into particles smaller or much smaller than 100 nm, or sometimes even into single atoms, on a support surface, which often is an oxide[11]. Such nanoparticles can be made either by carving them from the bulk using, e.g., laser ablation or

nanolithography techniques (top-down methods) or by synthesizing them from atoms or molecules using colloidal synthesis routes (bottom-up methods), as nicely summarized by Jamkhande et al.[12] Either way, the result is an *ensemble* of a very large number of catalyst nanoparticles either on a surface or in solution, that can be tailored for the desired catalytic reaction. While such ensembles indeed have been effectively used industrially for a very long time, it is also clear that there is further potential for improvement from the perspective that nanoparticle ensembles typically are characterized by significant levels of heterogeneity between particles in terms of size, structure, strain and even composition if also alloys are considered. This may be very relevant since certain reactions, for example, are facile over corner or edge sites on the particles[13], while others are facile over certain crystalline planes or terraces[14], and for some reactions, it is the very specific interplay between different types of sites[15] that is key. This, in turn, means that only a small(er) sub-fraction of particles in the ensemble actually functions optimally for a rection at hand, while (a large) sub-fraction may be less effective or not effective at all – or even create the wrong unwanted product since also selectivity of a catalytic reaction often is structure-sensitive[16]. Furthermore, also specific effects emerging at the nanoscale, such as electronic confinement effects[17], localized surface plasmon resonance (LSPR)[18] or the ratio of reactant binding to reactant releasing sites[19] may vary widely across different particle types. It is, thus, clear that both understanding which type of particle that works the best for a specific reaction and subsequently producing catalyst materials that feature these specific particles to the largest possible extent offers an avenue to greatly improve the performance of a catalyst, as well as optimize the use of the often scarce raw materials.

So, how then to approach then the optimization of nanoparticle catalysts from the perspective outlined above? The answer is conceptually simple but experimentally challenging: single particle catalysis. This emerging research field focuses on the investigation of individual nanoparticles with different experimental techniques with the ultimate goal to directly link single particle structure and composition with atomic resolution with catalyst activity and selectivity. The experimental methods used today in single particle catalysis research employ ubiquitously electromagnetic waves that range from infrared (IR) radiation to electrons and that carry information on either the chemical state of the particle, its surface or surrounding, or on the reactants involved in the catalytic reaction over the particle and the products formed. One powerful class of experimental techniques to study the nanoscopic realm of catalysts *in situ* uses X-ray synchrotron radiation since the short wavelength can resolve small structures[20] (5 nm to 10 nm) and the used high-energy X-ray photons are compatible with the atmospheric (or above) pressures of the catalytic reactor. Examples of widely used synchrotron-based techniques are scanning-transmission X-ray microscopy (STXM) and quick scan X-ray absorption fine structure (QXAFS)[21,22]. Furthermore, Bragg Coherent Diffraction imaging (BCDI) has recently emerged as method to create 3D images of crystalline nanomaterials[23]. Being based on transmissive X-rays, these methods can resolve the inner structure of complex catalyst materials. This concerns the tiny pores and the metal nanoparticle distribution inside the material, that can be assessed with nanometer spatial resolution[22]. The drawback with synchrotron methods is the extensive infrastructure that is needed to generate the radiation. Furthermore, they reveal only the structure of the catalyst or its chemical (oxidation) state but not their activity at the same time. Therefore, it is often used in concert with mass spectrometry, but this proves difficult at the level of the single nanoparticle due to low sensitivity.

Another noteworthy example of an experimental method for single particle catalysis observation is exploiting the fluorescence emission of (single) molecules[24] to reveal chemical reactions on the surface of single nanoparticles, sometimes even with sub-particle spatial resolution[25–28]. This approach is relatively new to chemistry but has been used in biology for decades[24] to study the processes within cells and organelles and earned Stefan Hell the Nobel prize in 2014. While the required experimental setup is relatively simple compared to a synchrotron experiment, the main limiting factors for (super resolution) fluorescence microscopy in single particle catalysis is the limitation to a very small of number specific reactions that either form a fluorescent product or during which reactant fluorescence is extinct. It is also limited to, from a technical catalysis perspective, unrealistically low reactant concentrations to ensure single molecular resolution in the super resolution version of fluorescence microscopy.

An additional family of single particle catalysis techniques focuses on the nanoparticles themselves since they are the catalytically active part and therefore the entities of interest to be investigated. However, it turns out that they also - at the same time - can play the part of the observer of a catalytic process that takes place on their surface[29]. This is enabled by an optical phenomenon called localized surface plasmon resonance (LSPR)[29–31], a coherent collective oscillation of the electrons of the particle that has its resonance frequency in the UV-vis-NIR spectral range, depending on the size, shape and composition of the particle, as well as the particles' intimate surroundings. The resonance frequency of the LSPR is for example sensitive to the oxidation state of a metal nanoparticle, which can be used to monitor the surface state of single catalyst nanoparticles[30,32–34] by tracking shifts in resonance frequency with high precision[35] using dark-field scattering microscopy[29,36]. However, this plasmonic nanospectroscopy and imaging concept does not provide information about the activity of the catalyst particle. In an attempt to alleviate this problem, earlier work in our group has combined LSPR with online gas-phase quadrupole mass spectrometry (QMS) from particles localized in tiny nanofluidic reactors[30,32,33]. Unfortunately, however, the QMS readout was limited to a few hundred nanoparticles since it did not provide the sensitivity to resolve the product formed on individual particles. However, the rise of deep-learning approaches to data evaluation has very recently put single particle reaction product assessment with QMS within reach, as very recently demonstrated by a colleague in our group[37].

The plasmon oscillation of metal nanoparticles can also be used to enhance the Raman absorption of molecules in their close vicinity, as it is done in plasmon- or tip-enhanced Raman spectroscopy (PERS and TERS, respectively)[38,39] that, as one example, has been used to investigate the photocatalytic processes of nitrothiophenol on Au surfaces[40]. One of the main drawbacks and limitations of PERS and TERS is that the enhancing plasmonic particle or tip must also serve as the catalyst, which limits the catalyst materials available severely since essentially only Ag and Au would provide a strong enough Raman-enhancing effect. To overcome this limitation, a solution was developed whereby the Raman-enhancing (Au) nanoparticle is isolated by a passive shell, in analogy to indirect nanoplasmonic sensing[34,41], in what has come to be known as Shell-Isolated Nanoparticle-Enhanced Raman Spectroscopy (SHINERS)[21]. This method has for example been successfully used for the investigation of the oxygen reduction reaction on high-index Pt surfaces where evidence of OH and OOH intermediates was found[42]. Despite this significant advance SHINERS has provided to Raman-based single particle catalysis, it is still limited by the fact that a passive and bulky (compared

to the catalyst particles) observer nanoparticle must be used, which may quite significantly impact the catalyst formulation and thus potentially the catalytic properties. Furthermore, SHINERS-type "antenna-reactor complexes", where a plasmonic antenna is placed close to catalyst nanoparticles, are widely explored in plasmon-mediated catalysis to enhance and steer catalytic reactions by light[43–46]. This highlights a risk of plasmon enhanced Raman spectroscopy methods, namely that the plasmonic effect used to probe the catalytic reaction at the same time also might (dramatically) impact it and, therefore, lead to wrong conclusions.

Another class of experimental methods widely used to investigate catalysis at the single nanoparticle level are electron microscopy approaches[20,47–49]. These methods focus on elucidating the (dynamics of) catalyst particle structure and (oxidation) state, and offer atomic resolution under certain conditions. At the early stages, scanning electron microscopy (SEM) and transmission electron microscopy (TEM) are used to study catalysts before and after reaction. The development of differentially pumped microscopes, sample cells and specialized holders have enabled the investigation of single particles at high pressures[50–52] (environmental TEM, ETEM) and even in the liquid phase[53,54]. They have, for example, revealed the oscillating behavior of Pt[55] or Pd[56] nanoparticles during reaction and monitored the dynamics of single atoms[57]. However, as the key limitations, electron microscopy methods can only investigate one particle at a time, and they do not provide information about (single particle) catalyst activity or selectivity. For further reading on single particle methods in catalysis, I suggest the excellent review by Sambur and Chen[58] or refer to the short overview given in **Chapter 2**.

To summarize, existing single particle methods generally investigate a certain aspect of the entire picture and require in most cases quite specific (and idealized) conditions and/or samples to work. This limitation is not different for catalysis experiments performed in the ensemble regime in general. Some experiments are often hampered by the, so called, "pressure and materials gaps" in catalysis, which means that it is experimentally challenging to investigate a catalyst at work with high spatial resolution in terms of (i) pressure of the surrounding environment (which in industrial reactors may reach tens or hundreds of bar) and (ii) the structural complexity of industrial catalyst materials. Hence, during the past decade or so, great efforts have been made to develop experimental methods that can investigate a catalyst at work, i.e., "*operando*", which means that they can probe the catalyst while it is converting reactants in real reaction conditions[26,47,58–61]. Again, focusing on single particle catalysis, in the current state of the art, only very limited efforts have been reported that enable the *operando* study of single particles. The few existing ones are concerned with ETEM[52] as described above, fluorescence (de)activation[62] and plasmonic nanospectroscopy[31]. As the final challenge referring to the materials gap, industrial catalyst nanoparticles are often in the sub-10 nm size range[63–65], both because this optimizes the volume/surface ration and because catalytic properties may become size dependent[66]

Consequently, the "holy grail" of single particle catalysis is to be able to scrutinize a single catalyst nanoparticle of technically relevant size and the catalytic reaction that occurs on its surface under real reaction conditions. To the best of my knowledge, this has not yet been achieved due to the lack of experimental method(s) that provide the necessary spatial and temporal resolution in combination with the required chemical sensitivity. Hence, my thesis work is aimed at pursuing this "holy grail" by developing a radically new experimental method that can meet the key boundary conditions: (i) single particle resolution, (ii) real reaction

conditions, (iii) no auxiliary techniques limiting the applicability, i.e., no use of plasmonic enhancements or fluorescence.

At the core of the method that I have developed to address this challenge are nanofluidic channels that can localize and isolate individual nanoparticles, as explained in detail in **Chapter 4**. The interaction between the channels and visible light is explained in detail in **Chapter 3**. Conceptually, this new optical microscopy approach is on one hand based on the fact that the refractive index (RI) of any fluid will change if its molecular composition is changed[67], for example by a chemical reaction between constituents of the fluid. On the other hand, it is based on nanofluidic systems and our expertise to use them to both manipulate and control fluids and single nanoparticles at the nanoscale in the context of single particle catalysis[32,33,68–71]. Finally, it builds on our recent discovery of the unique optical properties of nanofluidic systems fabricated into chemically very inert SiO_2 that already have enabled the label-free size and mass determination of single biomolecules using what we call "Nanofluidic Scattering Microscopy"[70] or "NSM", whose physics I describe in detail in **Chapter 2**.

In brief, the first key feature of NSM is that the used nanochannels´ geometrical cross section is smaller than any wavelength in the visible light spectral range, and that these channels thus scatter visible light very efficiently in the Mie-regime. The scattering is owing to the RI contrast between the solid material that hosts the channels and their interior, which is either a gas or a liquid. The second key feature is that the scattering intensity of a nanochannel depends on the RI difference between channel walls and channel interior. Hence, it was the core hypothesis of my work that reactants that are flushed into a nanochannel and react on a catalytically active particle localized inside that channel will change their molecular structure and thus molecular polarizability, which translates into a RI-change of the fluid in the channel. Accordingly, this RI change is expected to give rise to a change in the light scattering signature of the nanochannel, which is measurable in the context of NSM, and thus should make it possible to monitor the catalytic reaction and determine its rate, since this rate is proportional to the measured RI change (**Figure 1**).
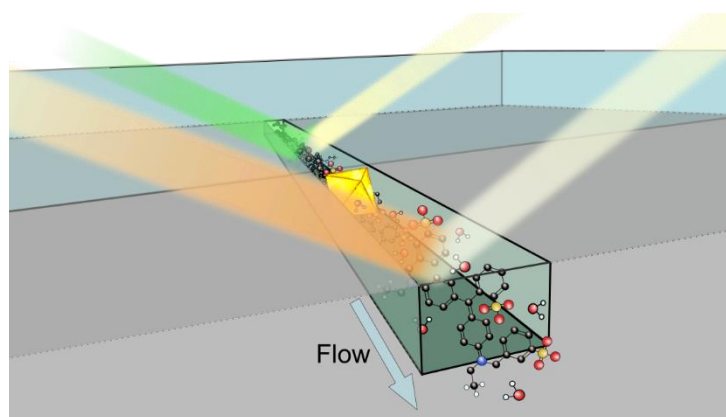

Figure 1. *Artist´s rendition of nanofluidic scattering microscopy for the monitoring of the catalytic activity of a single nanoparticle localized inside a nanofluidic channel. Due to a reaction-induced RI difference in the liquid in the channel up- and downstream of the catalyst particle, the light scattering intensity from the channel is different in these regions and thereby enables measurements of reactant conversion and thus particle activity.*

I have verified this hypothesis in **Paper I** on the example of hydrogen peroxide (H_2O_2) decomposition on single colloidal Pt nanoparticles trapped inside nanochannels.

Since the NSM approach is, in principle, compatible with a wide range of reactant types and concentrations, as well as reaction pressures, it promises to enable single particle catalysis studies at technically relevant *operando* reaction conditions. Furthermore, there are no (or at least very few) boundary conditions on the reaction itself, that is, it does for example not need to be fluorescent. This means in principle that experiments with an almost unlimited number of catalytic reactions and catalyst materials could be possible. Other conceptual benefits of executing (single particle) catalysis experiments inside nanofluidic channels include: (i) that single particles are isolated in their respective nanochannel, such that any crosstalk between particles, e.g., via reactant concentration gradients or spill-over effects to the support material, is avoided; (ii) that arrangements of many parallel nanochannels on a chip and in the field of view of an optical microscope enables the study of many single nanoparticles at the same time, while they all are isolated in their respective nanochannel; (iii) that due to the tiny dimensions of the nanochannels, they efficiently prevent extensive dilution of the small number of product molecules formed on single catalyst nanoparticles, and therefore maximize the RI contrast induced by the reaction. This, in turn, maximizes the chance that the conversion over a single nanoparticle can be experimentally measured, with the ultimate dream being particles in the sub-10 nm range.

Since NSM is an optical microscopy technique, it also offers the possibility to be further enhanced by implementing spectroscopic readout, that is, to measure the (white) light scattered from a nanochannel not in an integrated fashion but spectrally resolved. This would add the great benefit of accessing the wealth of information contained in a scattering spectrum (rather than a simple intensity image), that includes spectral fingerprints of molecules that are widely used in, e.g., UV-vis spectroscopy at the macroscopic scale. I demonstrate and discuss that this is indeed possible in detail in **Paper II** and **Chapter 2**, where I introduce what we call "Nanofluidic Scattering Spectroscopy" (NSS). I then apply NSS in **Paper III** to study the catalytic decomposition of fluorescein with sodium borohydride on the surface of a single Au nanoparticle, by also developing a transient, i.e., reversibly opened and closed, nanofluidic batch reactor that enables the trapping of reaction products in femtoliter volumes and enables their real time spectroscopic analysis using NSS. Finally, motivated by the experimentally verified hypothesis and great potential of NMS/NSS for single particle catalysis, I have developed a multifunctional fluidic chip holder with integrated electrodes and temperature control, optimized for advanced fluidic and optical microscopy operations by means of 12 inlet points, and compatible with 1 cm x 1 cm fluidic chips, which enable high-yield nanofabrication of up to 12 chips per 4-inch wafer (**Paper IV**).

1.1 Structure and Content of this Thesis

This thesis provides the background to put the experimental results presented in the attached scientific papers into a wider context. The four attached papers describe major steps in developing NSM/NSS as a novel experimental approach for single particle catalysis. These steps are: (i) Establishing NSM as a viable technique for single particle catalysis studies (**Paper**

I), (ii) Extending the scope of NSM by developing NSS and showcasing its ability to measure solute concentrations and their spectral fingerprints (**Paper II**). (iii) Applying NSS in concert with fluidic control to implement nanoscale single nanoparticle batch reactors with spectroscopic readout of a catalytic reaction (**Paper III**). (iv) Developing a multifunctional experimental setup to extend the experimental possibilities (**Paper IV**).

As a second aspect, my thesis also aims at summarizing additional results and insights obtained along the way, which were essential for the overall scientific progress made, but that are not included in the papers. In this way, I hope to supply valuable material for future generation scientists in the field. The thesis follows, in principle, the chronological development of my work outlined above, but also orients itself along the different levels of length-scales scale relevant to my work.

Chapter 2 is therefore dedicated to the smallest scale, as it describes first the principles of heterogeneous catalysis on surfaces, which happen at the Ångström level, before moving on to nanoparticles and their use as catalysts. The various single particle catalysis techniques briefly described in the introduction are summarized, and NSM/NSS is put into perspective. I also briefly discuss two catalytic reactions relevant to my work, i.e., H_2O_2 decomposition on Pt and the decomposition of dyes over Au nanoparticles in the presence of sodium borohydride ($NaBH_4$).

Chapter 3 zooms out into the realm of nanochannels and their function as single particle catalytic reactors, and as tool for detection of catalytic reaction product thanks to their specific optical properties. After introducing dark-field microcopy as method to peek into the nanoscale, I discuss analytically the light scattering properties of a nanochannel using Mie-theory. This leads to the mathematical expression governing the scattering intensity and its relation to the RI difference between the nanochannel and its surroundings. This theoretical foundation of the NSM method is then extended by introducing the Kramers-Kronig relation to understand the wavelength-dependence of light scattering from a nanochannel in the context of NSS.

Chapter 4 approaches the microscale as it is dedicated to micro- and nanofluidics. It provides a discussion of the origin of microfluidics and how it evolved into nanofluidics. It also explains the importance of designing fluidic chip holders, since they critically connect the micro- and nanofluidic systems with the macroscopic world, and thereby make it available for practical use. Additionally, some of the challenges involved when experimentally working with nanofluidics are discussed in detail, such as clogging and interference effects in dark-field microscopy/spectroscopy from certain surfaces.

Chapter 5 is fully dedicated to my work of developing a multifunctional fluidic chip holder with integrated electrodes and temperature control, and the corresponding microscope setup optimized for NSM/NSS experiments in the context of single particle catalysis.

2 HETEROGENOUS CATALYSIS ON NANOPARTICLES

It seems appropriate to perform research that deals with catalysis here in Sweden, as it was the home country of Jacob Berzelius who coined the term "catalysis" in 1835. He described it as "a well-known derivation in chemistry, call[ing] it the bodies *catalytic force* and the decomposition of bodies by this force *catalysis*"[4]. However, the very first known description of a chemical reaction that employs the catalytic principle is given by Elizabeth Fulhame in her essay from 1794, where she was investigating oxidation reactions and discovered that many of these reactions required water to be present and involved, but also that it is regenerated and detectable afterwards[3]. This is one part of the modern definition of a catalyst, i.e., a substance that is involved in a chemical reaction without being consumed by it. The other part of the definition is that this substance facilitates or enables a specific reaction by influencing the rate at which the involved species are transformed[72].

Catalysts are distinguished according to the phase in which the reaction products and the catalyst are in. Homogeneous catalysis concerns processes where the catalyst and the reaction products are in the same phase, which often is the liquid phase. This kind of catalytic process is ubiquitously found in nature, where enzymes in aqueous solutions perform a wide range of vital functions[2]. However, man-made homogeneous catalysis processes are also part of contemporary research and technology. For example, the synthesis of pharmaceuticals is reliant on homogeneous catalysis[73,74] or metal complexes in the liquid phase are used as photosensitizers in conjunction with catalysts in various reactions[75]. However, a major part of today's applied catalysis is performed with heterogeneous catalysts, that is, catalyst materials in the solid state with reactants delivered to them in the liquid or gas phase.

There are many prominent examples how heterogenous catalysis has influenced human development, most notable is, of course, the Haber-Bosch process[7,76] first developed in 1909. With this process, it was possible to bind atmospheric nitrogen to ammonia, thereby providing much needed agricultural fertilizer for an ever-growing population, but also providing at the same time the basis for highly destructive explosives[77]. In addition, heterogeneous catalysts are also essential for the synthesis of medicines, fuels and polymers, and help to create cleaner air by converting combustion products into non-toxic species (but – unfortunately – also CO_2)[6].

2.1 Catalysis on Surfaces

Given the great importance of heterogeneous catalysis in the contemporary industry landscape, it is understandable that a large portion of the current research in catalysis is dedicated towards comprehension and improvement of heterogeneous catalysts. Since these catalysts are in the solid state, it is their surface that primarily comes in contact with the reactants and products. To describe a model reaction over such a surface, I have depicted the basic principle in **Figure 2**.
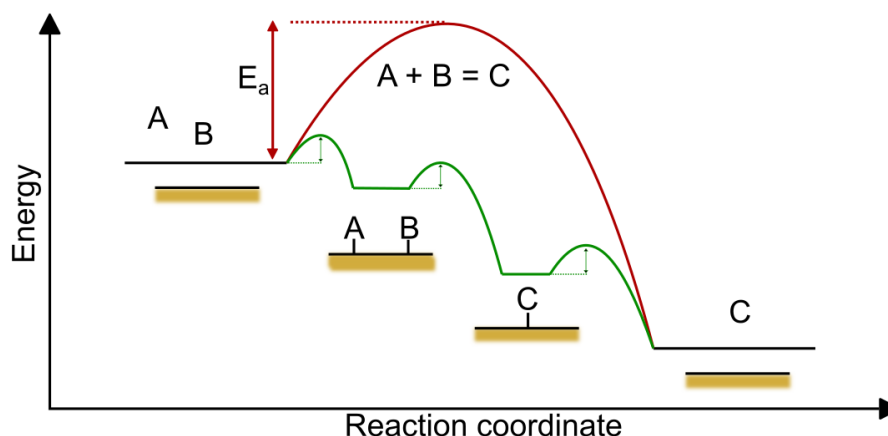
Figure 2. *Principle of heterogeneous catalysis. Two reactants A and B need to overcome an activation energy barrier E_a to reach an energetically favorable state in which they have reacted to product C. Due to this high barrier without catalyst (red path), the reaction rate is very low. A catalytic surface in the proximity can provide an alternative reaction pathway (green path) that includes several steps but with greatly lowered activation energies. The final product remains the same, as does the catalyst after the reaction.*

Here, two species A and B could reach an energetically favorable state C, which is the combination of A and B. In the liquid or gas phase, this reaction can occur, but the conversion is very slow as a large activation energy barrier E_a is inhibiting the reaction. This is a basic principle of chemistry and has been described by another famous Swedish researcher, Svante Arrhenius, who proposed in 1889 that the rate of a chemical reaction is proportional to the inverse exponential of the activation energy[78], $r \sim e^{-\frac{E_a}{k_b T}}$. From this relation it is clear that the rate of a reaction can be increased by increasing the temperature or by lowering the activation barrier, where the latter can be provided by a catalyst. If species A and B are now in close proximity to a suitable catalytic surface, it may be relatively easy for them to adsorb onto the surface when the energy barrier to do so is small. Once adsorbed on the catalyst, intramolecular bonds might be broken in the reactant molecules while at the same time new bonds with the catalyst surface are formed. In between these intermediate states is a very short-lived, activated state of the molecules, the "transition state", from which the next (energetically lower) intermediate state can be reached. As the key point, the barrier height to reach the transition state(s) on the catalyst surface is (much) lower than the barrier for direct reaction between A and B in solution or gas phase, which explains why a catalyst can facilitate a reaction on its surface. Once the new species have been formed in this way, what remains to close the, so-called, catalytic cycle, is that they leave/desorb from the surface to provide space for new reactants to bind to the catalyst surface. This is, thus, a critical step because if the products stay on the surface, they block it for new reaction cycles by "poisoning" the surface. One of the main goals of catalyst material development is therefore to find the catalysts that bind the reactants strong enough to break their bonds and, thus, enable the formation of the product, while not binding the products too strongly, such that they will not desorb from the surface. This principle is named after Paul Sabatier[79] who received the Nobel prize for his work on catalytic hydrogenation[80].

2.2 Single Particle Catalysis

The catalytic surface introduced above is not a uniform construct. It consists of various arrangements of surface atoms that may not even be the same element, e.g. in an alloy[81]. As shown in **Figure 3**, all surface atoms have a lower coordination (lower number of nearest neighbors) than an atom in the bulk of the material. Depending on where exactly a specific atom is situated, the coordination number may change from site to site. It is this interplay of high (many neighboring atoms) and low (few neighboring atoms) coordinated sites that dictates the binding energies for atomic and molecular species on the catalyst surface and consequently the energy landscape of the overall reaction[6].
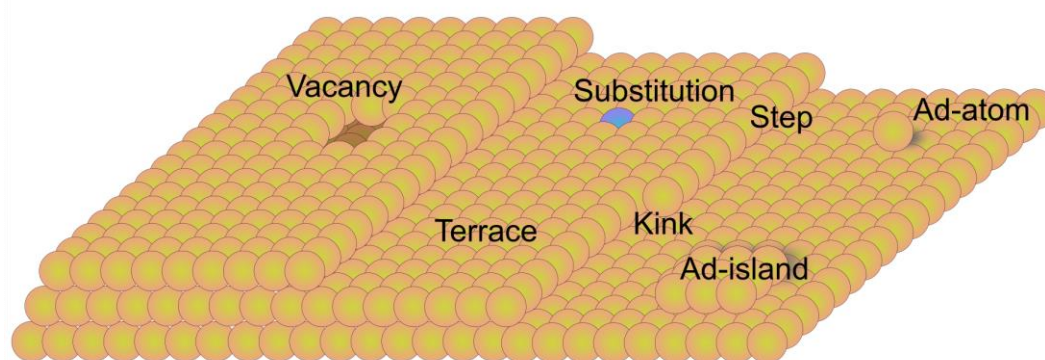

Figure 3. *Different surface sites on a catalyst surface. A catalytic surface consists of the same type of atoms as the bulk material but in various configurations in terms of coordination. In a facet plane (terrace) of a low-energy surface, such as (111) or (100), the coordination of each atom is relatively high when compared to kinks, steps or exposed island or ad-atoms. Substitutions, as found in alloys, can create energetically special sites*[11].

Here, nanoparticles provide interesting opportunities as they can be produced in a wide range of shapes, with different types of surface sites exposed. Consequently, nanoparticles are offering the possibility to tailor them to specific catalytic reactions. Furthermore, the distribution of the catalyst material into a myriad of nanoparticles with a high surface to volume ratio makes effective use of the often very rare and expensive (noble) metals that are widely used as catalysts. These metals often belong to the Pt group (Pt, Pd, Rh, Ru, Os, Ir)[82]. Apart from the purely geometrical advantages of catalytic nanoparticles, the physical and chemical properties also change when down-scaling to the nanometer regime[83]. In terms of chemistry, it is not only the great, yet diverse, number of surface sites a nanoparticle has to offer. Connected to this is also the work function, i.e. the energy needed for the extraction of an electron from the metal particle, that is strongly influenced by the position and shape of the valence band and the charged species on the surface[84,85]. Delocalized electrons in confined spaces can additionally cause size-dependent band-gaps[86] and plasmon oscillations, causing enhanced light absorption or scattering[44,87]. Furthermore, effects induced by the support used for the nanoparticles may play a greater role[88] because of spill-over effects[33,89,90]. Finally, in the realm of metal nanoparticles also other physical effects can be observed, such as the already mentioned plasmonic resonance[34].

2.2.1 Aim and Background

The importance of single particle investigations in catalysis

It is clear that catalytic nanoparticles are of utmost importance to the chemical industry, exemplified by the sales volume of catalysts was estimated to be up to $19 billion[88] in 2013 and has increased to $31.09 billion[5] in 2023. For the aforementioned Haber-Bosch process, a catalyst based on ubiquitous iron[77] is used, but many other every-day applications of catalysts contain a substantial amount of more (if not most) precious metals. For example, the average catalytic converter of a car contains around 290 ppm Rh, 720 ppm Pt and 1560 ppm Pd, such that each car carries nearly 2 g of Pt group metals[91]. The scarcity and with that the price of these very rare metals make it clear that they must be used with maximum efficiency. This is challenging to achieve since there was and, in some cases, still is a lack of fundamental understanding of the catalytic processes occurring on the surface of these metal nanoparticles. A further aspect is that these catalytic particles are produced in large quantities. This means that they can show great diversity in size and shape, as shown in **Figure 4,** and with that potentially in function.
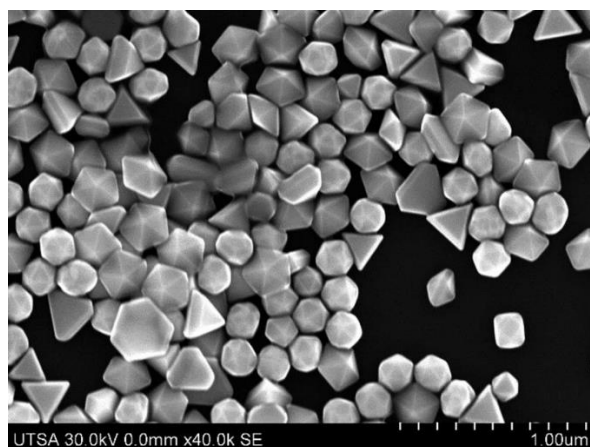

Figure 4. *SEM image of colloidal Au nanoparticles. These particles where grown from solution using polyvinylpyrrolidone (PVP), which is a widely used capping agent in colloidal synthesis[92]. The resulting particles vary in size and assume different shapes such as icosahedra, decahedra and truncated tetrahedra. Image courtesy of Plascencia-Villa et al[93].*

Here, single particle catalysis can provide invaluable insight for the understanding of catalytic processes and materials. The approach to investigate *individual* nanoparticles contrasts the more established methods for catalyst characterization, in which often ensembles of many millions of particles are investigated, which may mask the contribution of sub-populations of highly active particles, as well as of completely inactive ones, to the average[31]. In contrast, it is the goal of single particle catalysis to study structurally well-defined single particles as catalysts for a specific reaction, to draw concise structure-function correlations that can answer the question *why* specific particles have outstanding catalytic performance, and why some others do not. Answering such questions is not only relevant from an experimental perspective but also for the theoretical catalysis community, since ab-initio calculations of specific surfaces could be directly verified by experiments on defined particles[69,94]. As a consequence, the gained in-depth understanding of catalytic processes will ultimately benefit industry, as it contributes in the end to the development of highly effective catalyst materials.

Experimental methods for single particle catalysis

Given that nanoparticles are smaller than the wavelengths of visible light and that their geometrical and scattering cross sections are even smaller, it is a formidable challenge to find a type of (radiation) probe that can monitor the state of a single nanoparticle or its catalytic products. The above formulated goal of single particle catalysis has been approached via the investigation of different observables. For example, by assessing the unique characteristics of a catalytic nanoparticle itself, that is, the size, shape, crystallinity, support interaction and re-structuring under operating conditions[95]. Furthermore, focus has also been put on studying the interaction between individual particles, to investigate effects such as particle growth and shrinkage[96] in sintering process, as well as spillover of species participating in the catalytic reaction to the support or to other neighboring particles[89,97]. The actual conversion of reactants by a single nanoparticle has been investigated by monitoring the reaction products[27,62,68,69] using fluorescence quenching or mass spectrometry. The most important experimental techniques used in single particle catalysis today are summarized in **Figure 5**.

Analyte	Technique	Principle	Limitations
Particle	X-ray Microscopy	Oxidation or coordination state of the catalyst atoms detected by X-rays.	Synchrotron source required. High X-ray flux can harm sample.
Particle (surface)	Environmental Transmission Electron Microscopy (ETEM)	Special sample cells create confined high-pressure area around particle. Imaging and spectroscopy down to atomic resolution.	Limited field of view. Complex experimental infrastructure. Beam damage.
Particle (surface)	Electron energy loss Spectroscopy (EELS)	In conjunction with (E)TEM, scattered electron energy analyzed.	Limited field of view. Complex experimental infrastructure. Beam damage.
Particle (surface)	Plasmonic Nanospectroscopy	Localized surface plasmon resonance (LSPR) indicates with spectral peak shift particle change.	Requires particles of certain size and material. Readout needs correct interpretation, often involving complex simulations.
Particle Surface/ Surrounding	Tip-enhanced Raman Spectroscopy (TERS)	AFM tip used as light antenna, molecules detected via Raman-shift in probe signal.	Tip properties critical and limit reproducibility. Requires plasmonic enhancement.
Particle Surface/ Surrounding	Shell-Isolated Nanoparticle-Enhanced Raman Spectroscopy (SHINERS)	Plasmonic particle used as nanoplasmonic sensing device is isolated from actual catalyst by an inert shell.	Requires bulky Au/Ag that can influence catalyst structure. Electronic coupling can cause erroneous activity results.
Particle Surface/ Surrounding	Synchrotron-radiation-based Nanospectroscopy (SINS)	Like TERS, IR synchrotron light is collected after scattering.	Low IR scattering cross section. Synchrotron source required.
Particle Surface/ Surrounding	Surface Enhanced IR Spectroscopy (SEIRAS)	Molecular vibrations on particle enhanced by LSPR in the IR regime.	Low scattering cross sections for IR light. Requires plasmonic enhancement.
Reaction species	Single Molecule Fluorescence Microscopy	De-/Activation of a fluorescent dye caused by catalytic reaction detected.	Works only with fluorescent molecules.

Figure 5. *Overview of experimental methods in single particle catalysis.*

Those techniques include X-ray microscopy[59] that reports on the chemical (oxidation) state of the catalyst particle material by creating an image with ca. 10 nm spatial resolution[98]. Using high energy electrons, environmental transmission electron microscopy[55,99] and spectroscopy[100] (ETEM) can detect the crystalline structure and morphology of the particle at *operando* conditions with atomic resolution. If electron energy loss spectroscopy (EELS) is used in conjunction with ETEM, information about phonon excitation, band transitions and elemental composition can be gained at a sub-nm resolution[101]. Additionally, plasmonic nanospectroscopy[29,31,102] using visible light can report on changes of particle size, shape and oxidation state[30,31,33,103], and can detect oxidation-state changes of the particle surface[104] or particles in the proximity[41]. Furthermore, it can also be used to identify adsorbed species[29,34,105] and their spillover to other particles can be used for rate determination[90]. Other techniques that investigate the surface state of a catalytic particle are based on infrared spectroscopy, such as infrared nanospectroscopy[106] (SINS), surface enhanced IR absorption spectroscopy[106] (SEIRAS) and surface/tip enhanced Raman spectroscopy[40,61,107] (SERS/TERS), all analyzing which chemical species are adsorbed to the surface of the particle. The combination of SERS/TERS with plasmonic nanospectroscopy resulted in the development of Shell-Isolated Nanoparticle-Enhanced Raman Spectroscopy (SHINERS)[108].

Pioneering work in the field of single particle catalysis was done by Peng Chen et al., who demonstrated single molecule catalytic reactions over individual particles in operando conditions[109,110]. For this, they used the Au-nanoparticle-catalyzed deacetylation of amplex red by H_2O_2, generating fluorescent resorufin which became visible as distinctive emitters on the surface of the nanoparticles. The reverse principle was used by Levin et al., who used the reductive deactivation of the fluorescein emission over Au by $NaBH_4$ as a tool to characterize lithographic[68] and colloidal[69] single nanoparticles. However, both these approaches require the reactants or products to be visible by fluorescence, which limits the solute concentrations and the range of reactions that can be investigated.

This account of various approaches to single particle catalysis makes it clear that there is no single solution, and that each technique is designed to investigate a specific aspect of the catalytic function of nanoparticles. The aim of my work is to add one more solution to this toolbox: Nanochannel Scattering Microscopy/Spectroscopy (NSM/NSS).

2.2.2 Hydrogen Peroxide Decomposition

To evaluate the capabilities of NSM/NSS as method for single particle catalysis, I have chosen two model reactions: hydrogen peroxide (H_2O_2) decomposition over Pt (**Paper I**) and fluorescein reduction over Au particles (**Paper III**).

Hydrogen peroxide is a promising candidate for sustainable energy carriers in the future. It can be stored in liquid form[111] and is regarded an clean oxidant[112] that will decompose by itself when not kept in clean, low-pH conditions[113]. However, it is able to be reduced and oxidized in electrochemical applications[111], making it highly interesting for fuel cells[111] as source for electricity, as the catalysts in these devices use the decomposition of H_2O_2 to H_2O and O_2, as I will discuss below.

This catalytic reaction of H_2O_2 decomposition is quite well investigated[13,14,114–117] for various catalysts, and transitions metals from group 10 have emerged as established decomposition

catalysts, such as Pd[13,112,116] and Pt[14,85,118–121]. In the investigations leading to **Paper I**, I have focused on Pt even though Pd is more common in the earth's crust[122]. The decomposition of hydrogen peroxide on Pt surfaces can take different pathways[14], where at the end the total reaction can be summarized as follows.

$$H_2O_2 \xrightarrow{Pt} H_2O + \frac{1}{2}O_2$$
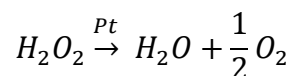
The pathways that do not use additional electrons (electrochemistry) or that do not require any other species present in the beginning other H_2O_2 and H_2O are the perhydroxyl anion-oxide, oxygen-oxide and the peroxide-oxide mechanism[14]. Focusing on the latter, as it starts with a clean, metallic Pt surface and describes the reaction as a single-site process, the pathway can be separated into two subsequent steps, as depicted in **Figure 6**.
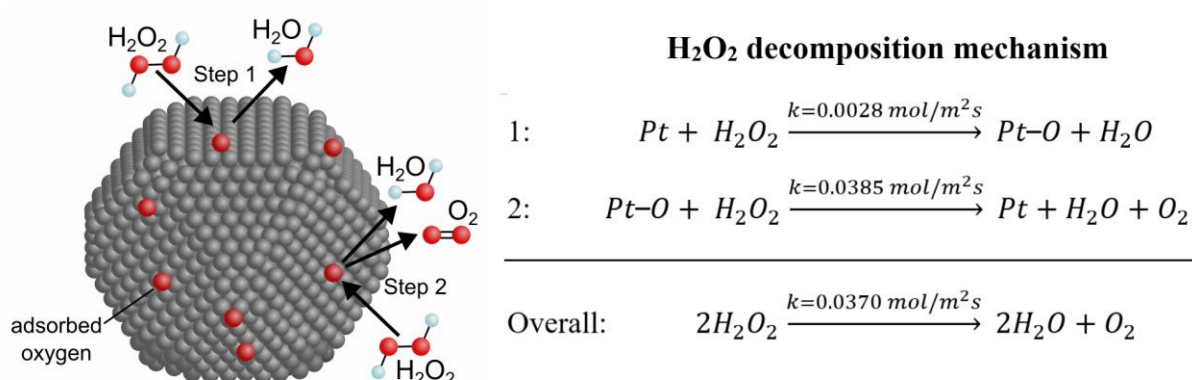

H₂O₂ decomposition mechanism

1: $Pt + H_2O_2 \xrightarrow{k=0.0028\ mol/m^2s} Pt{-}O + H_2O$

2: $Pt{-}O + H_2O_2 \xrightarrow{k=0.0385\ mol/m^2s} Pt + H_2O + O_2$

Overall: $2H_2O_2 \xrightarrow{k=0.0370\ mol/m^2s} 2H_2O + O_2$

Figure 6. *H₂O₂ decomposition on a Pt nanoparticle. The first step, the separation of one oxygen from H₂O₂ and its binding to the Pt surface is rate limiting. Figure adapted from Serra-Maia et al.*[118]

Investigations[118] into the nature of this reaction pathway have revealed that it is the first step that has the largest activation energy (20.14 kJ/mol) and that the activation energy of the second step is 4.4 times smaller (4.60 kJ/mol). Consulting the Arrhenius equation, which states that the rate of a reaction is proportional to the inverse exponential of the activation energy, makes it clear that the rate of the first step is much lower than that of the second step. It is therefore the first step, the transfer of one oxygen atom to the Pt surface, that is the rate limiting step in the overall reaction. By testing several models, Serra-Maia et al.[118] calculated the specific rates to be 0.0028 mol·m^{-2}·s for the first step and 0.0385 mol·m^{-2}·s for second step. This means that creation of surface oxide is slowing the overall reaction down but also that if oxygen is already present on the surface, the decomposition of H_2O_2 is progressing via the much faster second step of the reaction. This is important for the choice of catalyst size, as smaller nanoparticles tend to have more stable surface oxygen species than larger ones[14] due to the higher ratio of edge and corner sites. In that regard, larger Pt nanoparticles show a higher catalytic activity for H_2O_2 decomposition since the adsorbed oxygen is more readily released. This activity can be increased when the particles are pre-treated with processes that increase the surface oxide[85], for example heating in an oxygen-rich atmosphere or exposing them to highly concentrated H_2O_2. However, the conclusion that the size of the nanoparticles only needs to increase for an increase in reactivity needs to be put in perspective. First of all, for larger particles, the effectivity of material use is decreased since the surface to volume ratio decreases. Considering

kinetics, particles that are larger than 3-5 nm have a similar work function (ionization energy) as the bulk material (5.3 eV), while atomic Pt has a work function of 9 eV[14]. The same principle applies to specific sites on the nanoparticle, where sites in terraces with higher coordination have a lower binding energy for oxygen species and sites on edges and corners bind more strongly to the reactants[14,85]. This, in turn, means that smaller particles would be favorable in terms of creating adsorbed oxide as the high binding energy on the numerous uncoordinated sites helps to overcome the high activation energy of the first step, but it also means that these sites are less likely to release the products formed and create therefore a poisoned surface with fewer available reaction sites. In conclusion, the most ideal Pt particles for H_2O_2 decomposition according to Serra-Maia et al.[14,85,118,120] are below 5 nm in size and feature a surface rich in bound oxygen, that is, adsorbed oxygen Pt-O and not oxygen in the Pt lattice (Pt_xO_y).

The way in which I have investigated this catalytic reaction with the help of NSM on colloidal Pt nanoparticles trapped in individual nanochannels is described in detail in **Paper I**. **Figure 7** provides a short overview of the experimental process.
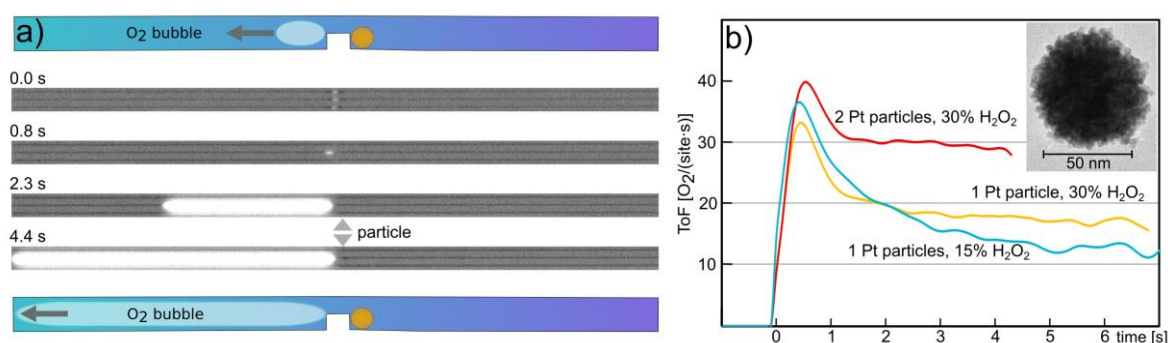

Figure 7. *Summary of the experiments in Paper I. a) A nanochannel was used as a flow reactor for this experiment, with a colloidal 70 nm Pt particle trapped at a constriction in the center of the channel. After the flushing in of a 30% or 15% H_2O_2 solution, the decomposition reaction began, creating oxygen that manifested itself as growing gas bubble in the channel, extending away from the constriction and the particle. Being clearly visible with NSM, the speed of growth of the bubble was measured, such that the gas volume produced could be derived. b) With an estimation of the particle surface and the number of reaction sites, a turn-over frequency (TOF) could be derived for single Pt particles under different conditions. The insert shows a SEM image of one particle, being comprised of smaller crystallites.*

The particles that I have used here are nominally of 70 nm diameter, but are agglomerates of smaller, 2 nm – 3 nm, crystallites which are close to the ideal particle described above for this reaction. I used here the key traits of NSM, as described in detail in **Chapter 3** below, that is, the detection and counting of the Pt particles as they enter the nanochannels and the subsequent flushing of H_2O_2 whose concentration changes I monitored by measuring the corresponding light scattering intensity changes of the nanochannel. Furthermore, I was able to quantify the growth of O_2 bubbles in the channel, since O_2 is one of the products of the H_2O_2 decomposition reaction on Pt. By evaluating the bubble volume and expansion speed over time, I could then estimate the turnover frequency (TOF) of single Pt particles. Furthermore, the observed encapsulation and reaction of a tiny reactant volume containing the catalyst particle between two O_2 bubbles sparked the idea of using nanochannels as transient batch reactors, a concept that I have implemented in **Paper III** using fluidic operations involving both liquid and gas.

2.2.3 Dye Reduction over Au Nanoparticles

Synthetic dyes are widely used in the food industry but are at the same time also investigated for their toxic and carcinogenic properties[123–127]. To this end, various methods have been proposed that can remove such harmful substances from wastewater. These methods include sorption techniques[126] and catalytic decomposition reactions[124]. In my thesis work, I have used three different dyes as model reactants for single particle catalysis in nanochannels since they are safe to handle, water soluble and provide interesting spectral fingerprints in the visible regime, which was important for the development of NSS. Hence, in this chapter, I will briefly discuss the catalytic degradation of allura red, brilliant blue and fluorescein dyes on Au surfaces. The term degradation is used to describe a general change in the molecular structure of the dye that leads to a loss of typical properties, e.g. absorption bands or fluorescent behavior. As these organic dyes are rather complex molecules, their degradation can follow various routes, being either oxidizing[124,125] or reducing[123,128] with respect to the dye molecule. The latter pathway includes a reducing agent that can donate electrons and protons, as for example sodium borohydride (NaBH$_4$) that I have used. To this end, the degradation of fluorescein[69,129] and brilliant blue[130] follows similar pathways, as both compounds experience a hydrogenation that changes the molecular structure only slightly but nonetheless disables the characteristic optical response, that is, light absorption and fluorescence emission from fluorescein, and light absorption from brilliant blue.

The process of reductive dye-hydrogenation facilitated by a Au nanoparticle catalyst and NaBH$_4$ can be described by two different pathways: electron transfer[128,129] or hydrogen transfer[69]. The first pathway requires the borohydride ion to react on the Au surface either with another borohydride ion $(2BH_4^- \rightarrow B_2H_6 + H_2)$[129] or with water $(BH_4^- + H_2O \rightarrow BO_2^- + 4H_2)$[128]. During that process, an electron is transferred to the Au particle. If a dye molecule then attaches to the nanoparticle as well, this electron is passed onto the dye molecule and opens a double bond. The injection of the electron might occur at any point of the conjugated π-system but will be directed towards an oxygen double bond in the case of fluorescein[129] or nitrogen double bond in the case of brilliant blue[128] as suggested by Wang et al.[129] Subsequently, a hydrogen from dissociated water will be added to the aromatic backbone of the molecule and complete so the hydrogenation. The second pathway requires the borohydride to first react with water $BH_4^- + H_2O \rightarrow BH_2OH + H_2 + H^+$ before the boron hydroxide is adsorbed to the Au surface[69]. Levin et al.[69] suggest that the step after the adsorption, namely the dehydrogenation, is rate-limiting for the overall reaction, and that it occurs preferably on sites with lower coordination. fluorescein, in contrast, is more readily bound to the surface of the Au catalyst such that a high dye concentrations in solution cause poisoning of the surface.[69] After one hydrogen has been separated from the boron hydroxide and diffuses across the catalyst surface, it attaches to a dye molecule bound to the surface and causes a hydrogenation there, such that the reduction of the dye is completed. A detailed analysis of the reaction paths of the fluorescein reduction reaction on Au is provided in **Paper II** and corroborated by NSS measurements in a femtoliter batch reactor hosting a single Au nanoparticle.

Allura red degradation is a reaction that, for example, has been investigated for sewage treatment purposes, since dyes of the azo group are known to persist for a long time in the environment[123–127,131]. I have worked with this reaction in various preliminary experiments that in the end have led to the results presented in **Paper III**, even though they are not included there. Even though not fully understood, it is reasonable to assume that the reaction initially

follows a similar route as described above for fluorescein and brilliant blue. This requires allura red molecules to adsorb on Au as the first step. That this happens is reasonable to assume, since brilliant blue is reported to bind to Ag nanoparticles[130], fluorescein[69,129] and nitrophenol[127,131,132] to Au nanoparticles, and since it has been shown that allura red degradation is greatly enhanced in the presence of Au nanoparticles[128]. A distinct difference between the degradation of allura red and brilliant blue/fluorescein, allura red is split into two organic acids[123], as shown in **Figure 8a**. Specifically, the central nitrogen double bond is broken when the adsorbed hydrogen from boron hydroxide or from the transferred electron on the Au attaches to dye adsorbed to the Au, such that NH_2 groups are formed. Since the distinct red color is caused by the $n - \pi^*$ transition of the azo-bond, the resulting degradation products appear colorless in solution[128].
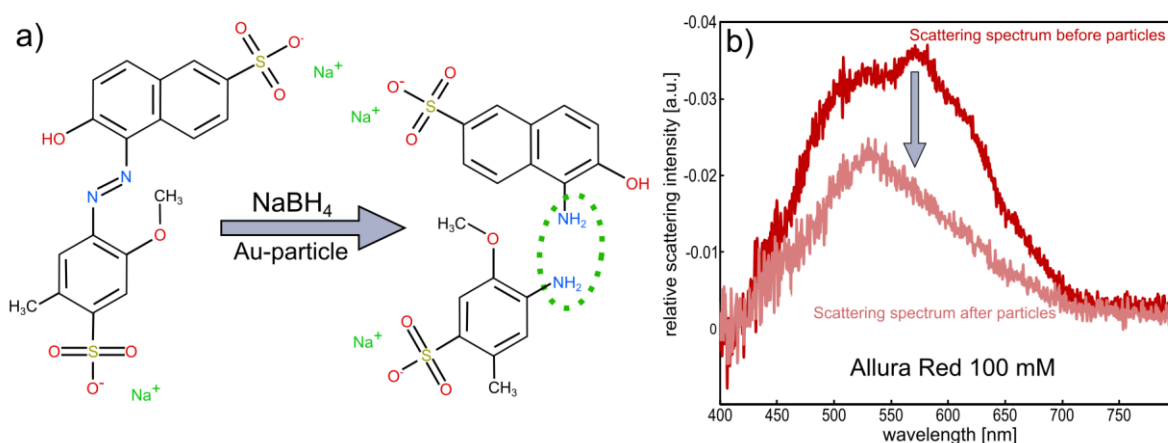

Figure 8. *Catalytic dye composition on the example of allura red. a) Schematic decomposition of allura red with $NaBH_4$ into 2-methoxy-5-methyl-aniline-4-sulfonic acid and 1-amino-2-naphthol-6-sulfonic acid on an Au catalyst[123] (structures adapted from same source). b) Some early unpublished NSS result from my thesis work in the form of scattering intensity spectra measured from two sections of a 200 nm by 200 nm nanochannel flushed with 100 mM allura red + 200 mM $NaBH_4$ solution. The channel was decorated with 100 Au particles of 50 nm diameter between the sections. A clear change in the spectral scattering response is seen after the solution has passed the Au nanoparticles, indicating the occurrence of the degradation reaction. I refer to Chapter 3.2.3 for a detailed explanation of NSS.*

In some of my early experiments, I have used this reaction to verify the catalytic activity of my Au nanoparticles and test the NSS readout (described in detail in **Chapter 3.2.3** and **Paper II**). As evident in **Figure 8b**, I was able to resolve a distinct change in the spectral fingerprint of a 100 mM allura red + 200 mM $NaBH_4$ solution flushed across 100 Au particles of 50 nm diameter arranged in a 200 nm by 200 nm nanochannel, which is a strong indication for the decomposition reaction to occur. However, while constituting encouraging preliminary results, we decided to at this point not further investigate this specific reaction for the following reasons: (i) the reduction of other dyes, such as fluorescein that I used in **Paper III**, is much better understood mechanistically[68,69,129], which is helpful when establishing a new experimental approach; (ii) the result shown above was achieved using 100 nanoparticles, which is far from the goal of single particle catalysis; (iii) the molecular extinction coefficient for allura red ($4.75 \cdot 10^4$ $M^{-1}cm^{-1}$ at 630 nm)[133] is relatively low when compared to brilliant blue (9.7 $M^{-1}cm^{-1}$ at 630 nm)[134] and fluorescein ($8.74 \cdot 10^4$ $M^{-1}cm^{-1}$ at 630 nm)[135], meaning that a higher concentration is required to achieve the same amplitude in the NSS, as shown in **Paper II**.

3 MICROSCOPY AND SPECTROSCOPY

Microscopy as such is a rather old concept used to investigate what is beyond the resolution power of the human eye, which means any structures that are smaller than 8.6 μm[136]. The earliest versions of magnifying instruments that used more than one lens were compound microscopes, with the first scientific work[136] published by Robert Hooke in 1665. These microscopes were relatively simple and used the reflected or transmitted light from the sample to generate an image. While this technique was immensely important for pioneers of biology and led to, among others, phase contrast and polarization microscopy, it had the drawback of a relatively high background brightness which made transparent structures on opaque samples difficult to image. However, reflection and transmission, as used in brightfield microscopy, are not the only interactions of light with an object. So-called dark-field microscopy makes use of the scattering of light from micro and nanoscale objects whose RI is different than that of their surroundings, which makes it both the best and simplest technique to monitor liquids and gases in transparent channels on the micro and nanoscale, which is the focus of my thesis work.

3.1 Dark-Field Scattering Microscopy

Before I introduce dark-field microscopy[70,137] as a technique to image nanofluidic structures, I will describe the experimental setup and the benefits arising from the use of dark-field microscopy. The light that is recorded from the sample is neither the light transmitted through it, nor the light that is directly reflected from its surface, it is the scattered light. As the name suggests, this light corresponds to the incident illumination redirected by a scatterer. Such a scatterer can be any object that interacts with this light. Important to note here is that scattering occurs at many angles, such that the object becomes visible from many directions, even if the incident light comes only from one direction. This is the basic principle of dark-field microscopy, where the illumination occurs at a shallow angle, such that only the scattered light is recorded with the microscope. As a result, any structures on the sample that scatter light appear bright, while the background remains dark – which is the effect behind the name of the technique. This is especially useful for seeing structures inside transparent objects, such as internal organs of biological species[138] or, as in my case, channels in SiO_2.

To make dark-field microcopy experimentally possible, a special objective with high numerical aperture is needed that illuminates the sample at a shallow angle, and at the same time collects only the scattered light. This is commonly achieved with two separate light paths through the objective, as shown in **Figure 9.** The illuminating light that is generated by a light source (halogen, LED lamp or a laser) is truncated into a ring-shape by an aperture and then directed into the outer perimeter of the objective, where a ring lens or mirror focuses this light on the same focus spot as of the imaging lens. From there, the scattered light is guided to a camera to be recorded, with the option of having a spectrometer before the camera to resolve the scattered light spectrally. This principle is the same for all microscopes I have worked on, may it be a conventional upright microscope with the objective placed above the sample or an inverted microscope with the objective underneath the sample.
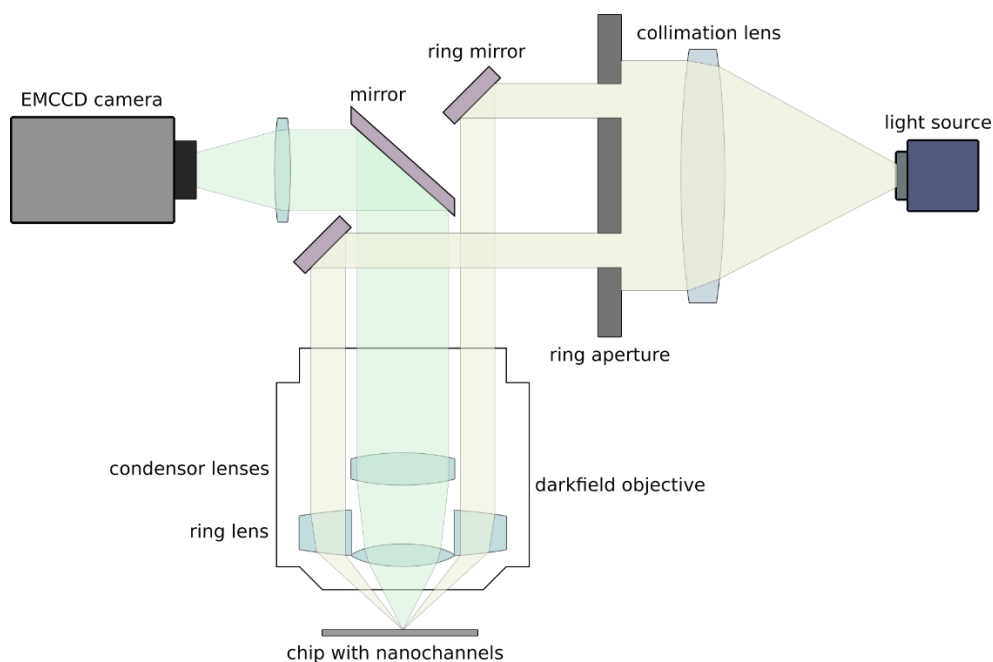
19

Figure 9. *Schematic of the dark-field microscopy setup used for NSM experiments. The camera and light source were selected to suit the demands of a specific experiment. For NSS, a spectrometer was placed in front of the camera.*

3.2 Light Scattering from Nanofluidic Channels

Scattering of electromagnetic waves from small objects is an extensive field in physics[139]. It is often separated into the different theories that describe scattering according to the size of the scattering object. At the level of the smallest objects, it is Rayleigh-theory that is used to describe the interaction of light with atoms and molecules, both being much smaller than the wavelength of the incident light. Since this type of scattering shows a distinctive dependency on the wavelength, it leads to common phenomena, such as the blue sky and colorful red and orange sunrises. Interestingly, we also find another type of scattering occurring in the sky, since clouds have a distinctive white-grey color. In contrast to the rest of the atmosphere, clouds are comprised of water droplets or ice crystals with sizes comparable to the wavelengths of sunlight. In this case, it is, therefore, Mie-scattering that describes best the scattering of electromagnetic waves from the water particles that form clouds. Mie-theory indeed predicts a nearly equal scattering intensity for all visible wavelengths, which, thus, explains the white-grey color of clouds, as well as that of milk and smoke.

In my work, as discussed above, I use nanofluidic channels to study catalysis on single nanoparticles since they: (i) offer a unique means to isolate single nanoparticles to avoid crosstalk between them, (ii) enable nanoscale control of reactant transport to and reaction product from single nanoparticles, and (iii) prevent the excessive dilution of reaction product to thereby – hopefully – make it detectable. As the focus of this chapter, I will discuss an equally important additional property of these channels that have geometrical cross sections on the same order of magnitude as the wavelengths of visible light (light is visible for the human

eye between 310 nm and 1100 nm[140]), i.e., between 100 nm and 200 nm. Hence, they interact strongly with visible light and this interaction is the basis for the NSM and NSS concepts I have developed to study catalytic reactions on single nanoparticles inside nanochannels.

To first conceptually understand these optical properties of nanochannels (before deriving more rigorously the most important formulas based on Mie-theory) let us consider scratches in a windowpane, which become clearly visible when the light scatters from them at a specific angle (**Figure 10a**). Here, the scratches are grooves filled with air, which has a RI (n) of roughly 1, in a silicon oxide (n = 1.462)[141] material. This means that this step in RI causes the light to be scattered from the SiO_2-air interface of the scratch.
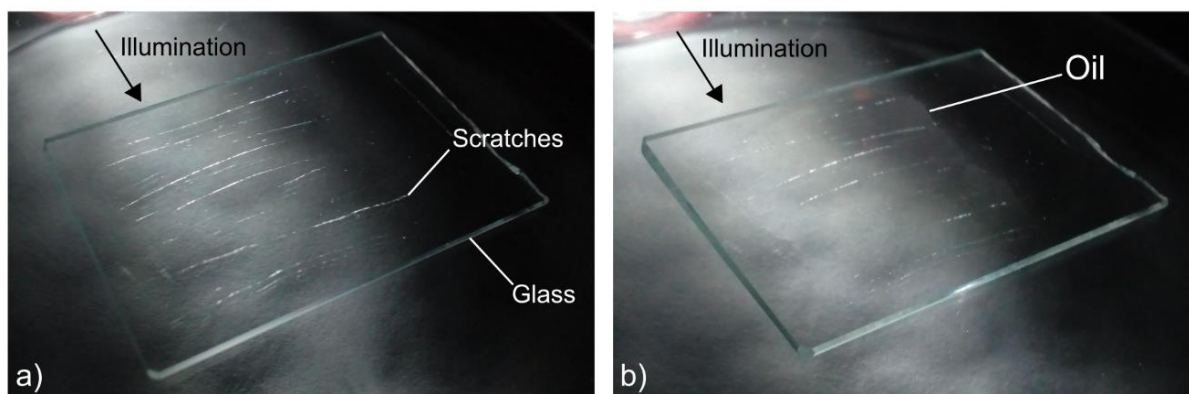

Figure 10. *Scratches in a glass surface in air and oil*. *a) The scratches in the glass (SiO_2, n =1.462)[141] surface can be seen as analogues of my nanochannels filled with air and are clearly visible to the naked eye. b) When the RI difference between content of the scratch and its surrounding is reduced, e.g., by applying rapeseed oil (n = 1.473)[142], the smaller scratches become invisible, while the scattering of the larger scratches is greatly reduced. In essence, this effect forms the basis for NSM and NSS.,*

The scattering from these scratches can be greatly diminished when they are filled with a material that has nearly the same RI as the surrounding material, i.e., glass, as I have done with rapeseed oil (n = 1.473)[142] in **Figure 10b**. Here, the difference in RI is much smaller (air – SiO_2: $\Delta n = 0.462$; oil – SiO_2: $\Delta n = 0.011$), causing the scattering of light from these scratches to greatly decrease in intensity and thus making them much less visible to the human eye. This is the very principle that is the basis for NSM and NSS, as the fluidic systems I have worked with in essence are tiny "scratches" in a glass surface that are filled with fluids of different RIs during my experiments. In the following chapter, I will describe this process in detail and present an analytical connection between RI difference and scattering cross section from elongated nanoscale objects, such as scratches or nanochannels.

3.2.1 Analytical Description of Mie-Scattering from a Nanochannel

To describe the nanochannels with rectangular cross section used in my experiments in the Mie-framework, I have approximated them as infinitely long cylinders. By doing so, I can then follow the derivation of equations that describe the scattering of light from such an object provided by Bohren and Huffman[139].

At the very start, there is the description of the incoming light as an electromagnetic wave.

$$\nabla^2 \psi + k^2 \psi = 0 \qquad\qquad \textit{Equation 1}$$

Here, ψ is the amplitude of the wave and the wavenumber $k = \frac{\omega}{c} = \omega\sqrt{\varepsilon\mu}$. Since the channel is approximated as being cylindrical, it is useful to use cylindrical coordinates, as shown in Equation 2.

$$\frac{1}{r}\frac{\partial}{\partial r}\left(r\frac{\partial \psi}{\partial r}\right) + \frac{1}{r^2}\frac{\partial^2 \psi}{\partial \phi^2} + \frac{\partial^2 \psi}{\partial z^2} + k^2 \psi = 0 \qquad\qquad \textit{Equation 2}$$

To solve the wave equation, a solution is required that can be separated into a radial, angular, and vertical part. The form of such a solution is given by Equation 3[139], where we define $\rho = r\sqrt{k^2 - h^2}$ and h is the separation constant.

$$\psi_n(r,\phi,z) = Z_n(\rho)e^{in\phi}e^{ihz} \quad (n = 0, \pm 1, \dots) \qquad\qquad \textit{Equation 3}$$
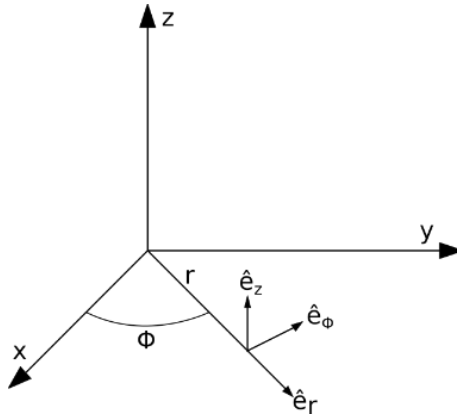

Figure 11. *The cylindrical coordinate system used for the derivations in this section.*

The linearly independent solutions to Z_n are the Bessel functions of the first and second kind, J_n and Y_n respectively, where n denotes their integral order. The harmonic functions for the cylinder that can be generated from Equation 3 are given as[139]

$$M_n = \nabla \times (\hat{e}_z\psi_n), \qquad N_n = \frac{\nabla \times M_n}{k} \qquad\qquad \textit{Equation 4}$$

when the unit vector that is parallel to the cylinder axis, $\hat{e}_z$, is taken as pilot vector. These harmonics are orthogonal to each other. If now the interaction of a plane wave $E_i = E_0 e^{ik\hat{e}_i x}$ that is incident onto a cylinder of radius a in the direction of $\hat{e}_i = -\sin\zeta\,\hat{e}_x - \cos\zeta\,\hat{e}_z$, with ζ being the angle between cylinder axis and the incident wave (see **Figure 12**) is considered, this electromagnetic wave needs to be expressed in the cylinder harmonics that are defined above. In addition, two different cases need to be investigated; one where electric field is parallel to the xz-plane and one where it is orthogonal to it.
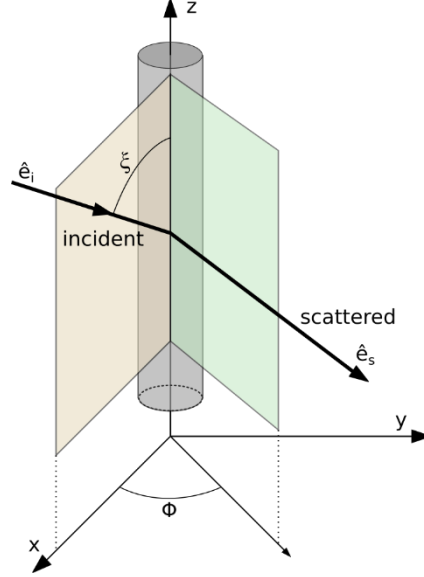
Figure 12. *Section of the infinite cylinder used to approximate a nanofluidic channel with the Poynting vector of the incident and scattered light.*

For the first case when the electric field is parallel to the xz-plane,

$$E_i = E_0(\sin\zeta\,\hat{e}_z - \cos\zeta\,\hat{e}_x)e^{-ik(r\sin\zeta\cos\phi+z\cos\zeta)} \qquad \textit{Equation 5}$$

the expansion of this field in cylinder harmonics is given as

$$E_i = \sum_{n=-\infty}^{\infty}[A_n M_n^1 + B_n N_n^1]. \qquad \textit{Equation 6}$$

It was stated above that the Bessel functions of the second kind, Y_n, are solutions to the wave equations as well. However, at this point, they must be excluded since the electric field at $r = 0$ cannot be infinite. Hence, only the Bessel functions of the first kind, J_n, remain as eligible solutions. When Equation 5 is compared with Equation 3, it is also clear that the separation constant h should be $-k\cos\zeta$. Having in this way defined the function that generates the cylinder harmonics, $J_n(kr\sin\zeta)e^{in\phi}e^{-ikz\cos\zeta}$, the steps provided by Bohren and Huffman[139] can be followed further to arrive at the following expressions for the coefficients A_n and B_n.

$$A_n = 0, \qquad B_n = \frac{E_0(-i)^n}{k\,\sin\zeta} \qquad \textit{Equation 7}$$

If then the electric field is defined as $E_n = E_0\,(-i)^n/k\sin\zeta$, the incident electromagnetic field in cylinder harmonics can now be written as

$$E_i = \sum_{n=-\infty}^{\infty} E_n N_n^1, \qquad H_i = \frac{-ik}{\omega\mu}\sum_{n=-\infty}^{\infty} E_n M_n^1. \qquad \textit{Equation 8}$$

The internal field of the cylinder in question has a similar generating function for the cylinder harmonics as the incident field, since this function is also using the Bessel functions of the first kind, and it needs to satisfy continuity at the boundary of the cylinder, such that $h = -k\cos\zeta$.

Here, it is important to introduce a relation that connects to the materials inside and outside of the nanochannel. Specifically, introducing m, which is the ratio between the RI of the material that fills the cylinder ($n_{cylinder}$; in my experiments this corresponds to a liquid or a gas) and the material the cylinder is embedded in ($n_{surrounding}$; in the experiments this will be SiO_2), as

$$m = \frac{n_{cylinder}}{n_{surrounding}}. \qquad\qquad Equation\ 9$$

Using this definition, the function that generates the internal field in the nanochannel is $J_n\left(kr\sqrt{m^2 - \cos^2\zeta}\right)e^{in\phi}e^{-ikz\cos\zeta}$, which leads to the following expansions of the internal electromagnetic field

$$E_I = \sum_{n=-\infty}^{\infty} E_n[g_n M_n^1 + f_n N_n^1], \quad H_I = \frac{-ik}{\omega\mu}\sum_{n=-\infty}^{\infty} E_n[g_n N_n^1 + f_n M_n^1]. \qquad Equation\ 10$$

The scattered field assumes subsequently a similar form

$$E_s = \sum_{n=-\infty}^{\infty} E_n[b_{n1} N_n^3 + i a_{n1} M_n^3],$$

$$\qquad\qquad Equation\ 11$$

$$H_s = \frac{ik}{\omega\mu}\sum_{n=-\infty}^{\infty} E_n[b_{n1} M_n^3 + i f a_{n1} N_n^3],$$

where the generating function $H_n(kr\sin\zeta)e^{in\phi}e^{-ikz\cos\zeta}$ is used, including the Hankel function of the first kind $H_n = J_n + iY_n$. The Bessel function of the second kind can be included since the scattered field can be considered to be an outgoing wave at large distances from the cylinder ($|\rho| \gg n^2$). Looking at the boundary conditions at $r = a$, Bohren and Huffman[139] offer the following relations for the coefficients a_n and b_n

$$a_{-n1} = -a_{n1}, \qquad b_{-n1} = -b, \qquad a_{01} = 0$$

Assuming now the common case that the incident light is normal to the cylinder axis ($\zeta = 90°$), a_{n1} vanishes, the coefficient b_n for the case of the electric field of the incident light being parallel to the xz-plane becomes the following, where $x = ka$:

$$b_{n1}(\zeta = 90°) = b_n = \frac{J_n(mx)J_n{}'(x) - mJ_n{}'(mx)J_n(x)}{J_n(mx)H_n{}'(x) - mJ_n{}'(mx)H_n(mx)} \qquad Equation\ 12$$

For the second case, where the incident electrical field is perpendicular to the xz-plane, the derivation for the coefficients that was laid out in Bohren and Huffman's book[139] follows similar steps, finally arriving at an expression for a_n under the condition of normal incidence.

$$a_{n2}(\zeta = 90°) = a_n = \frac{mJ_n{}'(x)J_n(mx) - J_n(x)J_n{}'(mx)}{mJ_n(mx)H_n{}'(x) - J_n{}'(mx)H_n(x)} \qquad Equation\ 13$$

The incident, internal and scattered electromagnetic waves can now be described in terms of cylinder harmonics and the necessary coefficients a_n and b_n are available when considering the scattering from a normally incident wave of either polarization. Therefore, the scattering cross sections of our nanochannel under the approximation that it is a cylinder of infinite length can now be calculated.
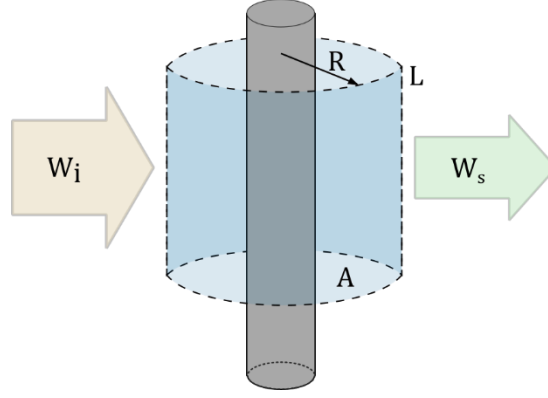
Figure 13. *Incident light W_i and its scattered part W_s, together with the integration surface around the cylinder.*

As any infinite object would have an infinite cross section, it is advised to define the cross section with regards to a certain unit length. For this purpose, a closed concentric surface is constructed around the cylindrical particle that has length L (in the direction of the z-axis) and radius R, together with a mantle surface A (**Figure 13**). This allows it to consider rates at which the incoming light is absorbed and scattered.

$$W_a = -\int_A \mathbf{S} \cdot \hat{\mathbf{n}} \, dA = W_{ext} - W_s = RL \int_0^{2\pi} (\mathbf{S}_{ext})_r \, d\phi - RL \int_0^{2\pi} (\mathbf{S}_s)_r \, d\phi \qquad \text{Equation 14}$$

The radial components of the Poynting vector $\mathbf{S}$ are used above, following the definition as the cross product of the electric and magnetic field.

$$S_{ext} = \tfrac{1}{2} \, \text{Re}(\mathbf{E}_s \times \mathbf{H}_s^*), \ \ S_s = \tfrac{1}{2} \, \text{Re}(\mathbf{E}_i \times \mathbf{H}_s^* + \mathbf{E}_s \times \mathbf{H}_i^*)$$

Starting now with the first case that we discussed above, the incident electric field being parallel to the xz-plane, we insert the corresponding series expansions (Equation 8 and Equation 11) into the formulas above and execute the integration. This results in an expression that relates the coefficients a_n and b_n to a scattering efficiency Q_{sca}. This scattering efficiency compares the scattered radiation to the actual geometric dimension the nanochannel

$$Q_{sca,p} = \frac{W_s}{2aLI_i} = \frac{2}{x}[|b_0|^2 + 2\sum_{n=1}^\infty (|b_n|^2 + |a_n|^2)]. \qquad \text{Equation 15}$$

For the second case, i.e., the electric field being orthogonal to the xz-plane, the derivation is similar and leads to the following scattering efficiency

$$Q_{sca,o} = \frac{2}{x}[|a_0|^2 + 2\sum_{n=1}^\infty (|a_n|^2 + |b_n|^2)]. \qquad \text{Equation 16}$$

If the incident light is unpolarized, which is commonly the case in experiments where continuous wave light sources are used (like in my experiments), the scattering efficiency can be written as

$$Q_{sca} = \tfrac{1}{2}(Q_{sca,p} + Q_{sca,o}).$$

Another important simplification that can be done at this point is the assumption that an object that is much smaller than the wavelength of light is considered. Specifically, if we look at x,

which is defined as $x = ka = 2\pi a/\lambda$, we see that it becomes very small since the radius a of nanochannel I typically use in my experiments is at around 70 nm and the visible light spectrum is centered around 550 nm. This enables us to use relatively simple forms[139] of the Bessel functions needed for the coefficients a_n and b_n, that is

$$J_0(z) = 1 - \frac{z^2}{4}, \qquad J_1(z) = \frac{z}{2} - \frac{z^3}{16}, \qquad Y_0(z) = \frac{2}{\pi}\ln\left(\frac{z}{2}\right), \quad Y_1(z) = -\frac{2}{\pi z} \quad .$$

Inserting those expressions in Equation 11 and Equation 12 then yields the necessary coefficients for the scattering efficiencies, provided that only the terms with the smallest degree in x are considered.

$$a_o = \frac{-i\pi x^4(m^2 - 1)}{32}, \qquad b_o = \frac{-i\pi x^2(m^2 - 1)}{4}$$

$$a_1 = \frac{-i\pi x^2}{4}\left(\frac{m^2 - 1}{m^2 + 1}\right), \qquad b_1 = \frac{-i\pi x^4(m^2 - 1)}{32}$$

Equation 17

From here, I can go back to Equations 15 and Equation 16. Using only the terms with the highest contribution, the following expressions for the scattering efficiencies for parallel and orthogonal incident light are gained.

$$Q_{sca,p} = \frac{\pi^2 x^3}{8}(m^2 - 1)^2 = \frac{\pi^2 k^3 a^3}{8}(m^2 - 1)^2$$

Equation 18

$$Q_{sca,o} = \frac{\pi^2 x^3}{4}\left(\frac{m^2 - 1}{m^2 + 1}\right)^2 = \frac{\pi^2 k^3 a^3}{4}\left(\frac{m^2 - 1}{m^2 + 1}\right)^2$$

Equation 19

These efficiencies are given with respect to the projected surface $2aL$ that the normally incident light "sees" when approaching the cylindrical nanochannel. To finally be able to write down the equations that define the nanochannel scattering cross sections, the above equations need to be multiplied by this projected surface. While doing so, the geometric nanochannel cross section, $A_\emptyset = \pi a^2$, emerges and the scattering cross sections for parallel and orthogonal polarization can be written as

$$\sigma_{sca,p} = \frac{A_\emptyset^2 k^3 L}{4}(m^2 - 1)^2$$

Equation 20

$$\sigma_{sca,o} = \frac{A_\emptyset^2 k^3 L}{2}\left(\frac{m^2 - 1}{m^2 + 1}\right)^2$$

Equation 21

If finally unpolarized light irradiation is assumed, as in my experiments, we average both scattering cross sections and arrive at Equation 22, which is the fundamental formula for NSM.

$$\sigma_{sca,u} = \frac{A_\emptyset^2 k^3 L}{4}(m^2 - 1)^2\left(\frac{1}{2} + \frac{1}{(m^2 + 1)^2}\right)$$

Equation 22

the importance of Equation 22 is given by the fact that it combines the measured scattering intensity (through the scattering cross section) via the geometry of the fluidic system (channel dimensions) to the properties of the medium inside the channel. It can be seen from this formula that a short wavelength and a large channel would, in principle, be beneficial for an improved scattering signal. On the other hand, in the context of measuring reaction product formed on a

single catalyst nanoparticle, a large channel would lead to a more diluted product concentration in the nanochannel and, thus, a reduced RI contrast, which consequently would reduce the sensitivity in that way. The ideal channel for NSM when used for single particle catalysis is therefore large enough to be a good scatterer but also small enough to keep the reaction products from one single nanoparticle concentrated. On a side note, if we assume an RI ratio of $m = 0.9$, the cross section for the parallel incident light contributes around 63% to the combined cross section, indicating thereby another way how the sensitivity could possibly be enhanced, i.e., by investing all the available light power into parallel polarized rather than unpolarized light.

3.2.2   Nanofluidic Scattering Microscopy – NSM

Liquid exchange and concentration assessment

After having laid out the basis for understanding NSM with the very simple demonstration at the start of **Chapter 3.2**, and describing it analytically in **Chapter 3.2.1**, I would now like to show a first application of NSM that I have developed. For this purpose, I use results from **Paper I**, where I used a fluidic design as shown in **Figure 16** to demonstrate the light scattering response of a nanochannel to a liquid exchange. The nanochannels used here had a 150 nm x 150 nm cross section and a total length of 340 µm, whereof 170 µm are within in the field of view of the camera. At first, the parallel nanochannels, situated between two microchannels, were filled with pure water (n = 1.333)[143]. Then, a 30 % solution of hydrogen peroxide (H_2O_2) was flushed into the nanochannels by applying a pressure of 2 bar to one inlet of one microchannel, with the result shown in **Figure 14**.
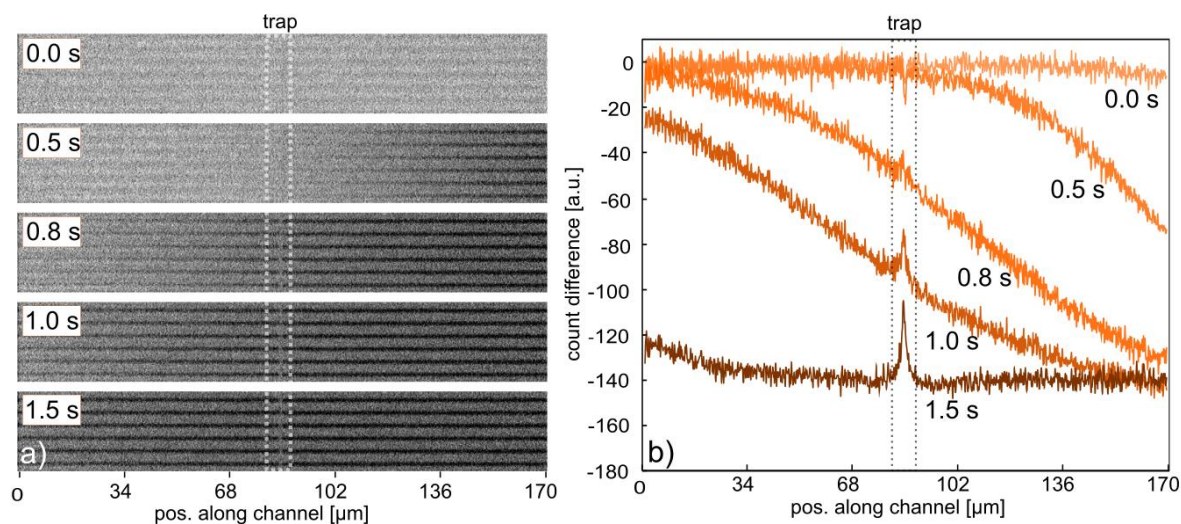

Figure 14. *Liquid exchange in nanochannels monitored by NSM. a) Series of dark-field images of six parallel nanochannels after a reference image with water-filled channels has been subtracted. The H_2O_2 entering the nanochannels can be seen as darkening of the image. b) Relative scattering intensity difference of one nanochannels along its length. At the start, the channel is water-filled (zero difference in scattering) and subsequently flushed by a 30% H_2O_2 solution by means of convective flow. The concentration front can be seen moving through the channel over time. The marked trap area is later used for colloidal particle trapping for catalysis experiments.*

From the picture series in **Figure 14a**, it is clear that replacing H_2O by a 30 % H_2O_2 solution causes the nanochannels to appear darker, meaning that the intensity of the light scattered from them has decreased. When the relative (with respect to water) intensity change is plotted for specific times along one nanochannel, as done in **Figure 14b**, more fluidic effects become visible. It can be very clearly seen that the H_2O_2 solution does not enter the nanochannel abruptly, but exhibits a stretched-out diffusion front, meaning that the transition from a pure water-filled channel to a solution-filled channel happens gradually. As the diffusion of H_2O_2 in the micro and nanochannels occurs at the same time as the convective flow caused by pressure applied to the H_2O_2 reservoir on the fluidic chip, a diffusion front in the shape of an error-function is moving through the nanochannel. A more detailed description of this process together with an assessment of the diffusion constant is given in **Paper I**. In general, when a liquid other than pure water is entering a previously water-filled nanochannel, the scattering intensity decreases if this liquid has a higher RI than water. While the analytical explanation is already given with Equation 22, I would like to visualize this phenomenon in **Figure 15**. Here, I used Equation 22 to plot the theoretical scattering cross section of a 140 nm x 140 nm nanochannel of 170 µm length that is illuminated by 550 nm light. To show the general behavior predicted by Equation 22, the RI range for the medium inside the channel is varied from 0.8 RI-units (RIU) to 2.4 RIU.
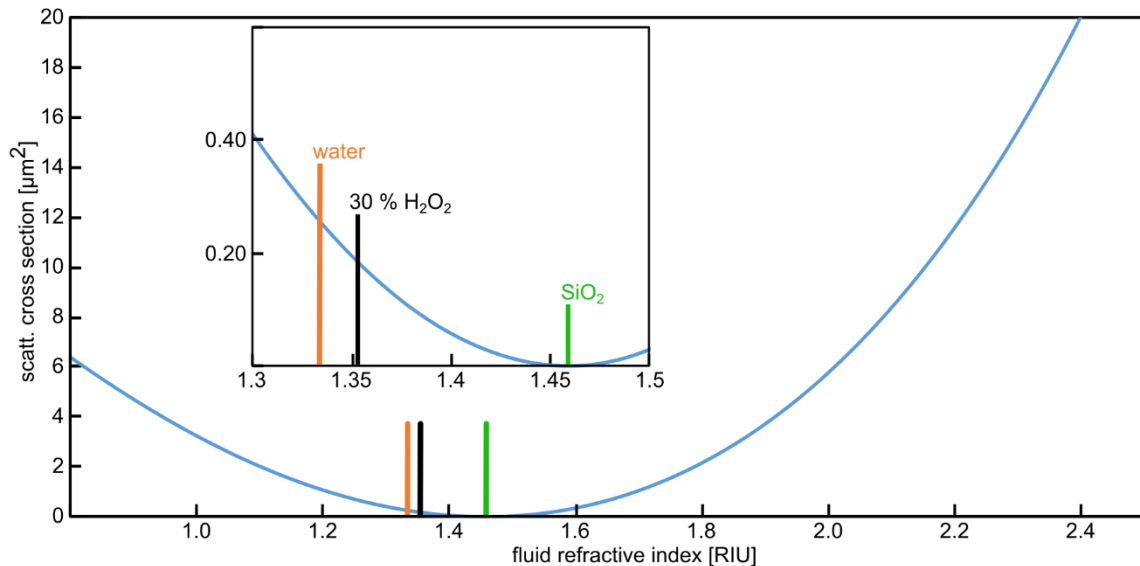

Figure 15. *Connection between fluid RI and nanochannel scattering cross section. Theoretical scattering cross section (blue) of a 150 nm x 150 nm nanochannel of 170 µm length calculated using equation 22 and plotted over a wide range of RIs for the medium inside the channel. The markers indicate the RIs for SiO$_2$ glass (n = 1.4585 RIU)[141], water (n = 1.3333 RIU)[143] and a 30% aqueous H_2O_2 solution (n = 1.3529 RIU)[144].*

The RI dependence of the calculated nanochannel scattering cross section exhibits a minimum at exactly the RI value of SiO_2 (1.4585 RIU)[141]. The explanation can be found by analyzing Equation 22 or by considering that a channel filled with SiO_2, while being also embedded in SiO_2, would be optically invisible since no light could scatter from it. Hence, its scattering cross section is zero. When the channel is filled with water (1.3333 RIU)[143], however, we see that the scattering cross section of the channel is now approx. 0.28 µm². This means that the channel will now scatter light efficiently and will become visible in an experiment, such as the

one summarized in **Figure 14**. Exchanging the liquid in the channel from pure water to an aqueous 30% H_2O_2 solution, we also change the RI to 1.3529 RIU[144], which according to Equation 22 yields a scattering cross section of 0.19 µm². This is significantly lower than for the water filled channel (see also inset in **Figure 15**) and thus the explanation for the result that we see in the measurement shown in **Figure 14**, where the scattering intensity of the water filled nanochannel is higher than for the H_2O_2 filled one. While Equation 22 is not linear over the complete RI range shown in **Figure 15**, for the small RI differences that I am considering in my work, it can be approximated as linear in a reasonable way.

Another interesting aspect is that the change of scattering cross section and scattering intensity, would be much more pronounced for liquids that have a higher RI than SiO_2, as seen for RI values above 2 in **Figure 15**. While such liquids exist (e.g. selenium monobromide[145], n = 2.02 RIU), they have significant drawbacks, such as high viscosity, and are not suited as solvent for a chemical reaction. As a similar thought, the RI of the surrounding material could be changed, such that it will have a larger difference to the RI of water. While this may be more feasible technically, it still poses the challenge of finding a material that has the same well-established properties as SiO_2 (e.g. in terms of chemical inertness) and for which micro- and nanofabrication recipes readily exist.

Particle detection and counting

Another way to use NSM is to monitor small objects in nanochannels, such as nanoparticles. After the discussion presented in section 3.2.1, it is clear that the presence of a nanoparticle inside a nanochannel also induces a (small) change in the local scattering cross section of the system. In other words, the anticipated reason why such a particle becomes visible with NSM is simply that a particle has a much higher RI compared to the liquid inside the nanochannel alone. However, this is not the full picture. Specifically, earlier research in our group found that for biological nanoparticles inside a nanofluidic channel (e.g., a protein or an extracellular vesicle) it is the interference between the scattering from the particle and the scattering from the nanochannel that creates the optical contrast[70]. In fact, this interference-based contrast is much larger than the purely RI-based one, which makes even single proteins visible in NSM.[70]

It is therefore interesting to consider the scenario for metallic nanoparticles, which also support LSPR and that leads to a strong interaction with irradiated visible light via both absorption and scattering[137,146,147]. Hence, in principle, when located inside a (light scattering) nanochannel the response of the combined system could: (i) be that the absorption of light by the metal nanoparticle simply causes a decreased scattering intensity of the combined system at the position of the particle or (ii) that the interference of light scattered by the channel and the particle creates a distinct enhanced or reduced response. Elucidating this question is part of the ongoing research in our group. In my work presented below and in **Paper I,** I used Pt nanoparticles which have a relatively weak plasmonic response that is dominated by absorption[87]. Hence, they are not readily visible in traditional dark-field microscopy as Au or Cu particles would be[148]. Notably, however, they can be made visible in nanochannels with NSM, as I show below.

In these experiments, I used nanochannels that feature a nanofabricated constriction in the center of each nanochannel (**Figure 16a**). This constriction is designed to work as a physical trap for colloidal nanoparticles flushed through the nanochannel and corresponds to a 1 µm long section of the nanochannel along which the free height is reduced to 30 nm. Hence, any

object larger than 30 nm cannot pass and will get mechanically trapped, while liquid flow through the nanochannel still is possible. The nanoparticles I used were spherical Pt colloids with a nominal diameter of 70 nm, comprised of small crystallites in the few nm size range (**Figure 16b**). Pt is reported as an excellent catalyst for H_2O_2 decomposition as discussed in section 2.2.2, on par with or even exceeding Pd in terms of activity[116]. As a first step, I verified that these particles could enter the nanochannels by means of convective flow and that my fluidic design was suitable for trapping these particles. For this, I used a fluidic chip with a glass lid only weakly bonded by polysilsesquioxane (PSQ), as developed by Levin et al.[69], to enable reopening of the chip after particle trapping to verify the number of trapped particles by electron microscopy. **Figure 16c,d** show SEM images of a single and of multiple of such Pt nanoparticle(s) captured by a nanochannel trap.
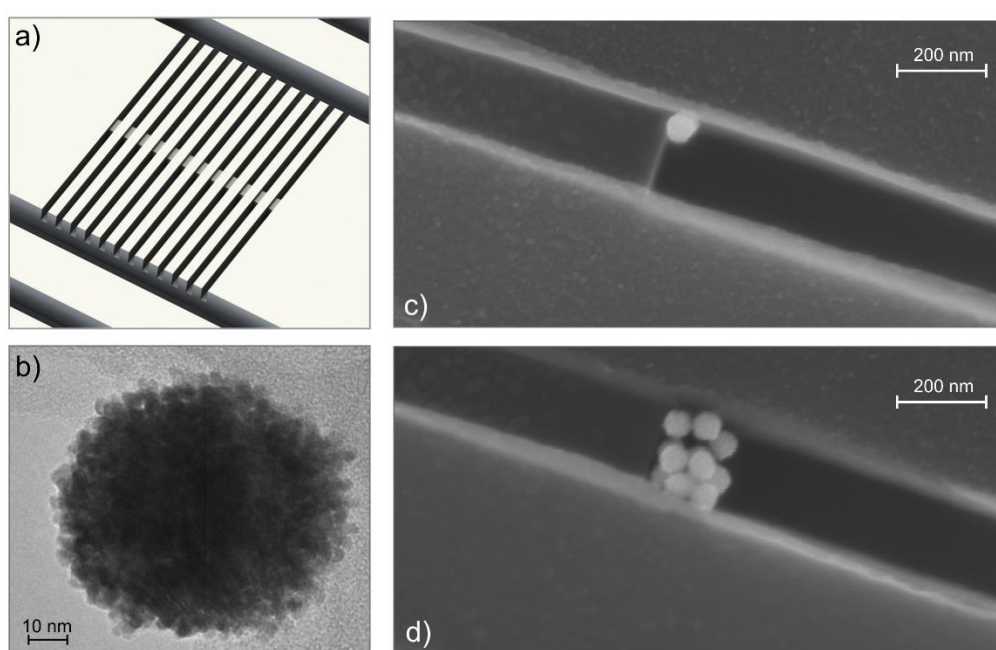

Figure 16. *Trapping of colloidal particles in nanochannels. a) Artist's rendition of nanochannels with vertical constrictions in the center that serve as traps for colloidal nanoparticles flushed through the channels. b) TEM image of a Pt particle. Note the highly structured surface due to the particle being comprised of small crystallites in the few nm size range. c) SEM image of a constriction with a single trapped colloidal Pt particle. Taking this image was possible by using polysilsesquioxane (PSQ) to reversibly bond the lid to the chip, which enabled the reopening of the chip after particle trapping and thus imaging of the trap region. d) Same as c, but with trap at which 8-9 Pt particles have accumulated.*

Since the re-openable chips with PSQ-bonded lids cannot be used for the catalysis experiments reported in **Paper I** due to leaking between nanochannels in the nanochannel array, I decided to use NSM to count Pt particle(s) trapped in each channel when the lid instead was thermally bonded onto the chip. This was of particular importance since we (i) aimed at true single particle experiments and (ii) needed to know the number of particles in each channel to be able to ultimately derive accurate reaction turnover frequencies in **Paper I**.

The first method that I have developed to see "dark" Pt particles in the channels is by taking a reference picture of the empty channel system and subtracting it from the subsequent series of pictures in the trapping experiment (**Figure 17a,b**). This method is straightforward, but it requires a very stable setup, such that the reference picture remains valid for the entire experiment. The second method that does not require an empty channel reference is based on the fact that the parallel nanochannels on my chip form a regular periodic pattern. Hence, by using a fast Fourier transform (FFT) bandpass filter and thereby eliminating the frequency belonging to the channel pattern from the picture, the particles appear as distinct dark spots since they do not periodically occur in the scattering images (**Figure 17c**). The drawback with the FFT approach is the relatively slow and computationally costly Fourier transformation. Hence, I have used the subtractive referencing method in the experiments described in **Paper I**.
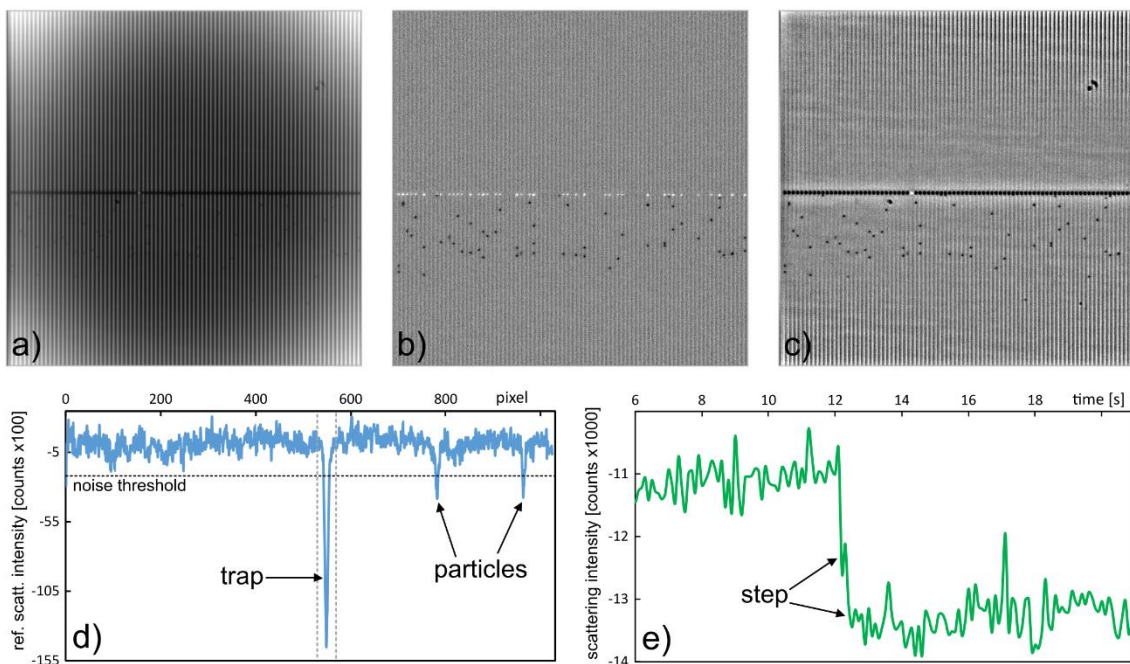

Figure 17. *Single Pt colloidal particle detection and counting. a) Raw dark-field micrograph of an empty nanofluidic system with parallel nanochannels. The dark line in the middle stems from the traps and the radial intensity gradient is the consequence of uneven illumination of the sample. b) Differential image obtained by subtracting an image of the nanochannels when the particles were pressed towards the trap (by convective flow through the channel) from an image where Pt particles are randomly diffusing inside the channel in absence of flow. This procedure reveals the particles as dark spots. Note that the white spots at the traps mark positions at which the particles were localized in the reference image. c) FFT version of the same image as in b). FFT reveals the particles since they are not part of the regular nanochannel pattern, as even more (immobilized) particles can be seen than in b). d) Counting of freely diffusing particles by detecting their (negative) scattering intensity peaks along the nanochannel. e) Counting of nanoparticles at the trap by monitoring the change of the scattering intensity at the trap area over time. The arrival of a particle at the trap causes a steplike decrease in the scattering intensity.*

With a method now at hand to resolve single Pt nanoparticles inside my nanochannels, the next step was to find a way to count them to know how many of them that are captured by each trap and thereby be able to optimize the trapping procedure towards as many single nanoparticles

in each individual nanochannel as possible. In principle, there are two possibilities to do this. The first one relies on the fact that the particles are subject to Brownian motion[149,150], which means they will move randomly in front of the trap, provided no convective flow forces them against the trap. By simply monitoring the motion of the particles over time, I can count the number of particle peaks in the scattering trace along the nanochannel (**Figure 17d**). This method requires that no particle gets immobilized at the trap because in that case they cannot be counted. The alternative way to count trapped particles is to monitor the scattering intensity at the trap area of the channel since any Pt particle arriving there will reduce the scattering intensity in a stepwise manner (**Figure 17e**). In my work, I have used this method, as it was crucial to detect any particle arriving at the trap to not misinterpret their activity.

3.2.3 Nanofluidic Scattering Spectroscopy – NSS

The Kramers-Kronig relation

In the preceding section, I outlined how white light scattering from a nanochannel depends on the difference in RI between the material inside the channel (in my case a liquid, even though gas bubbles were investigated in **Paper I**) and the material that surrounds it. However, a further interesting aspect is that the RI in general is wavelength dependent. To this end, while liquids, e.g. water, or solids, e.g. SiO_2, that are transparent to visible light exhibit RIs that are fairly smooth, if not constant, there are many systems and molecules that exhibit distinctly wavelength-dependent RIs, which is often connected to a sizable light absorption at specific wavelengths. Well-known examples are (aqueous solutions of) dyes[133], such as brilliant blue, allura red and fluorescein already discussed above in the context of catalysis, or metal complexes, which can find use as photosensitizers for catalysis[75]. Applied to my nanofluidic channels, their absorption bands lead to light scattering properties that cause a strongly modulated scattering spectrum of a channel filled with such a dye solution.

The key to understanding this effect is the Kramers-Kronig relation. In a mathematical sense, this relation connects the real and imaginary part of a complex function that is analytic in the upper half plane and vanishes sufficiently fast for large arguments[133]. In my case, this complex function is the RI, $\boldsymbol{n}(\omega) = n(\omega) + i\kappa(\omega)$, since it contains in its real part the index for diffraction and in its imaginary part the extinction coefficient. With this information at hand, the Kramers-Kronig relation can be written as[151]

$$n(\omega) - 1 = \frac{2}{\pi}\mathcal{P}\int_0^{-\infty} \frac{\omega'\kappa(\omega')}{\omega'^2 - \omega^2}d\omega' \qquad \textit{Equation 23}$$

where $\mathcal{P}$ denotes the Cauchy principal value of the integral. When now this equation is rewritten by substituting the wavelength $\lambda = 2\pi c/\omega$, the result is

$$\Delta n(\lambda) = n(\omega) - 1 = \frac{2}{\pi}\mathcal{P}\int_0^{-\infty} \frac{\kappa(\lambda')}{\lambda'\left(1 - \left(\frac{\lambda'}{\lambda}\right)^2\right)}d\lambda' \qquad \textit{Equation 24}$$

The relation between κ and the experimentally measurable absorption coefficient α is given by

$$\kappa(\lambda) = \frac{\alpha \, \lambda}{4\pi} \qquad\qquad\qquad\qquad\qquad \textit{Equation 25}$$

With this relation at hand, an experimentally determined absorption coefficient can be related to the real part of the RI, as demonstrated by Sai et al[133]. In addition, and of key importance for my work, the above means that changes in the absorption coefficient of a liquid inside a nanochannel can be measured accurately and in a spectrally resolved way by measuring the wavelength-dependent scattering intensity from this nanochannel – the essence of NSS. This, in turn, opens the possibility to identify chemical compounds inside a nanofluidic channel based on their distinct spectral "fingerprint" derived from the light scattering signature of the channel.

Connecting absorption and scattering spectra

To demonstrate the NSS concept discussed in detail in **Paper II**, I used the dye brilliant blue and analyzed the obtained results theoretically using Equation 22 in combination with Equation 24. To measure scattering spectra from only a single nanochannel, I closed the entrance slit of the spectrometer mounted on the dark-field microscope, such that only the scattering signal from this single nanochannel is recorded. To further reduce readout noise and minimize the amount of data, the whole spectrum was binned along the nanochannel. Accordingly, the scattering spectra shown in **Figure 18** for 50 mM brilliant blue aqueous solution and pure MilliQ water, respectively, correspond to the accumulated scattering intensity of the whole nanochannel.
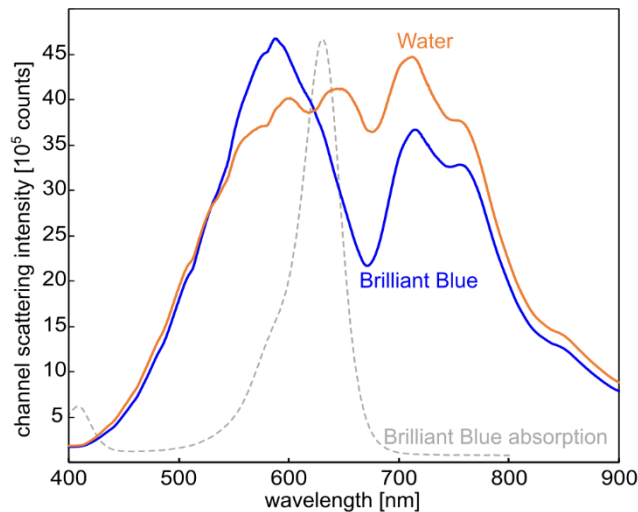

Figure 18. *Scattering spectra of a single nanochannel filled with pure water and a 50 mM brilliant blue solution. First, the scattering spectrum of a single nanochannel filled with pure MilliQ water (orange line) was measured. Subsequently, a 50 mM brilliant blue solution was flushed through the nanochannel (blue line). Also shown is the absorption spectrum of brilliant blue[133] (dashed black line) measured by standard absorption spectrophotometry (ASP).*

The presence of the dye solution in the nanochannel is reflected clearly in its scattering spectrum (**Figure 18**), where a large reduction of the scattering intensity can be seen around 670 nm, while the scattering is enhanced around 587 nm, when comparing to a water-filled channel. This is at first a somewhat puzzling result, since if it only were light absorption of the dye that is seen in the scattering spectrum, only a reduction of the scattering intensity at 620 nm would be expected. It is also remarkable that the distinct peaks appear at wavelengths where

the absorption of the dye either in- or decreases. To analyze this, I refer first to Equation 24 to derive from the absorption coefficient spectrum of the dye (**Figure 19a**) the wavelength dependent change of the RI (**Figure 19d**), as caused by the wavelength-dependent extinction of the dye solution. Subsequently, I use this RI change in Equation 22 to determine the induced change of the nanochannel scattering cross section. Now comparing the position of the positive (around 600 nm) and negative (660 nm) peaks of the scattering cross section difference ($\Delta\sigma$) shown in **Figure 19d** with the changes in the scattering intensity (**Figure 18**) induced by brilliant blue, and remembering that the scattering intensity is proportional to the scattering cross section, it is clear that the distinct absorption of the dye creates a distinct scattering spectrum, albeit indirectly via the RI. The same relation between absorption spectrum and RI, and consequently between RI and scattering cross section, can be established for virtually any species that have a distinct color in the visible regime. For completeness, I have repeated the process discussed for brilliant blue also for allura red and fluorescein (**Figure 19c-f**), yielding very similar results.
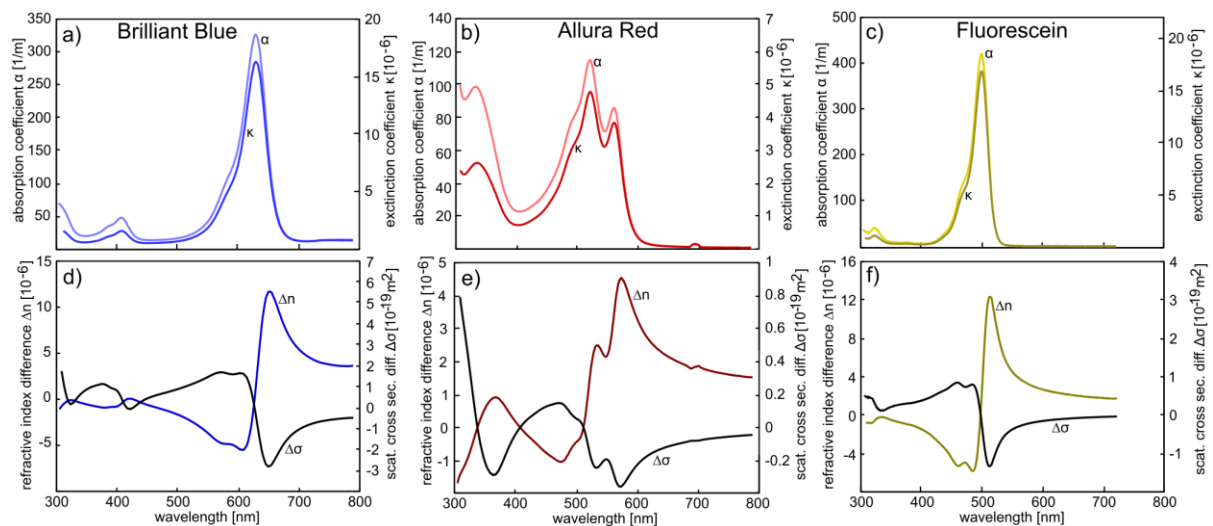

Figure 19. *Analytical transformation from absorption coefficient spectra to scattering cross section spectra for brilliant blue, allura red and fluorescein aqueous solutions. a) to c) The absorbance spectra as measured with ASP are here shown as absorption coefficient spectra, which can be calculated by dividing the measured absorbance values by the optical path through the sample solution (here 1 cm) and by log(e). The subsequent calculation of the extinction coefficient κ is done with Equation 25. d) to f) Using κ in the Kramers-Kronig relation (Equation 24) yields the change of the real part of the RI caused by the respective absorption features of each type of dye molecule in the solution. Applying then Equation 22 delivers the scattering cross section of a nanochannel filled with the corresponding dye solution. Subtracting the scattering cross section of a water-filled channel finally yields the difference in scattering cross section, Δσ, which is proportional to the observed difference in scattering intensity.*

Developing an optical referencing scheme for NSS

The most crucial part when extracting molecule-specific scattering spectra from nanochannels filled with an analyte solution is the comparison with the scattering measured from the same channel filled with the solvent, which in my case always has been MilliQ water. This is conceptually comparable with the working principle of a macroscopic absorption spectrophotometer, where first the absorption spectrum of a water-filled cuvette is recorded before the actual solution in an identical cuvette is measured, such that any contributions from any sources other than the solution itself can be excluded. The same referencing principle can be applied to NSS, only that it here must be the very same nanochannel that is compared while being water- and solution-filled. This is critical because even only very small variations in, e.g. nanochannel roughness can influence the result. Furthermore, it is beneficial if the nanochannel of interest is not moved or repositioned during the whole experiment, since even slight motion can have consequences for the resulting scattering spectra. Another point that distinguishes NSS from ASP is that due to the small scale of the whole experimental environment, it is very susceptible to drifts of the microscope stage, defocusing and fluctuations in the illumination, together with stray light from the environment, as well as temperature changes. To address these issues for ASP, split-beam spectrometers[152] (sometimes referred to dual-beam spectrometers) have been developed that split the sample beam in two, such that one beam can always be directed through a reference cuvette while the other beam is measuring the actual sample at the same time.
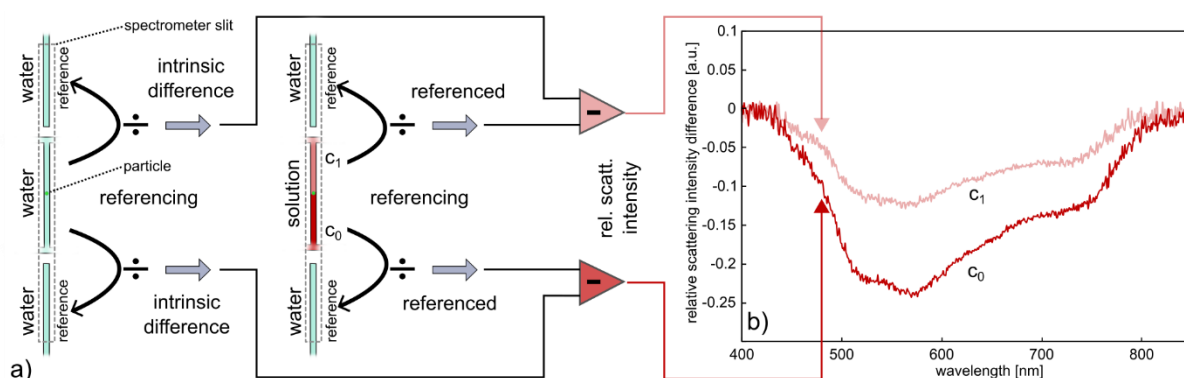

Figure 20. *Optical referencing scheme for NSS, resulting in relative scattering intensity difference spectra (RSID). a) As a first step, all nanochannels are filled with the solvent of choice (water in my case) and the spectrum from the sample channels is divided by the spectrum of the reference channels to measure the intrinsic difference between those two scatterers. The sample channels are subsequently filled with solutions of different concentrations (or different concentrations are caused by a reaction over the particle), and their spectrum is divided again by the (constant) reference spectrum. As a final step, the intrinsic difference between sample and reference channel obtained in the first step is subtracted to gain what we call the relative scattering intensity difference - RSID - spectra, here exemplified on an aqueous allura red solution.*

I have used the same principle and implemented colinear reference nanochannels that are disconnected from the actual sample nanochannels into the fluidic design. They are placed above and below the central channels (which may contain catalytic particles) as shown in **Figure 20a**, such that the lower and upper reference channels together with the central channels fit in the slit of the spectrometer. These reference channels serve the purpose of remaining filled

with a reference liquid (preferably the solute, water for the work presented in this thesis) during the entire experiment, while in the central channels the liquid/reactant solutions are exchanged. In this way, simultaneously measuring the optical response from the reference channels and the channels in which a solute is exchanged, or a catalytic reaction may occur, enables the continuous optical referencing of the reaction channels (**Figure 20b**) in the same way as in dual-beam ASP. This eliminates intensity fluctuations and drifts from the light source, as well as effects from slow microscope defocusing and background scattering from the sample signal.

Since the nanochannel that is used as reference is not the exact same channel that is used for the sample to be analyzed, the difference in scattering between this reference channel and the sample channel must be determined. To do so, the entire fluidic system of the chip, that is, both reference and reaction systems, are first filled with water to measure a scattering spectrum of all channels and channel sections of interest: (i) the upper reference channel, (ii) the section(s) of the sample channel upstream of the catalyst particle, (iii) the section of the reaction channel downstream of the particle, (iv) the lower reference channel. When subsequently comparing the scattering spectrum taken from the sample channel upstream of the particle with the upper reference channel spectrum (and likewise for the downstream fraction of the sample channel and the lower reference channel) as shown in **Figure 20a**, we obtain the intrinsic difference in light scattered from the selected fraction of the sample channel and the corresponding reference channel. In this way, during a catalysis experiment in the sample channel, all non-solution related contributions to the measured scattering spectra can be eliminated by subtracting the simultaneously measured scattering response from the reference channels adjacent to the up- and downstream fractions of the sample channel. The result of this procedure yield what we call the *"relative scattering intensity difference"* - RSID, as it displays how different the scattering intensity is for each wavelength when compared to the scattering from a water filled reference channel (**Figure 20b**). As explained when introducing the concept of NSM in **Chapter 3.2.1**, a higher concentration of a solute will cause (depending on its spectral features) an increased negative RSID amplitude. The neutral baseline is at zero, since the intrinsic difference (which is around 1) is subtracted in the evaluation. This reference scheme is used throughout **Paper II**, **III** and **IV**.

Reversing the analysis - from scattering cross section to extinction coefficient

In **Figure 19**, I demonstrated how absorbance spectrum and scattering spectrum are analytically connected. Here, I will outline the reverse process, which is analytically feasible but not without challenges. To process the measured experimental data in a mathematically feasible way, the connection between RSID and scattering cross section of the nanochannel, $\sigma_{channel}$, needs to be established first. To do this, I consider the scattered power, P_{scat}, as the product of incident intensity, $I_{incident}$, and $\sigma_{channel}$. Furthermore, we remind ourselves that the experimentally measured RSID is defined as the scattering spectra recorded from the solution-filled sample channels divided by the scattering spectra from the water-filled reference channel with the intrinsic difference spectrum subtracted. Hence, to amend this mathematically, an ideal intrinsic difference spectrum, which corresponds to 1 for all wavelength, is added to the experimental spectra (**Figure 21a-c**) as

$$RSID + 1 = \frac{P_{scat,solution}}{P_{scat,water}} = \frac{I_{incident}}{I_{incident}} \frac{\sigma_{channel,solution}}{\sigma_{channel,water}} = \frac{\sigma_{channel,solution}}{\sigma_{channel,water}} \qquad \textit{Equation 26}$$

As second step, I consider the scattering cross section, $\sigma_{channel}$, of a nanochannel as given by Equation 22 above, but as a simplification I use here only the formula for incident light that is polarized parallel to the nanochannel (Equation 20), as it is the main contributor to the scattering intensity.

$$\sigma_p = \frac{A_\emptyset^2 k^3 L}{4}(m^2 - 1)^2. \qquad \textit{Equation 27}$$

With that, the RSID can be written as a ratio of scattering cross sections, were the geometry and wavelength dependent prefactor vanishes, and were m can again be substituted with the ratio of RIs of the solution in the channel and the SiO$_2$ the channel is embedded in.

$$RSID + 1 = \frac{\sigma_{channel,p,solution}}{\sigma_{channel,p,water}} = \frac{\left(\left(\frac{n_{solution}}{n_{SiO2}}\right)^2 - 1\right)^2}{\left(\left(\frac{n_{water}}{n_{SiO2}}\right)^2 - 1\right)^2} \qquad \textit{Equation 28}$$

Solving this equation for $n_{solution}$ provides four solutions, of which I will continue with the following as it is not resulting in negative values for $n_{solution}$ and applies to the case where $n_{water} < n_{SiO2}$.

$$n_{solution} = \sqrt{\sqrt{(RSID + 1)(n_{water}^2 - n_{SiO2}^2)^2} + n_{SiO2}^2} \qquad \textit{Equation 29}$$

Using here the literature values for the RI spectra for water[153] and SiO$_2$[141], I arrive at the RI spectra for the respective solutions, as shown in **Figure 21d-f** for brilliant blue, allura red and fluorescein. It is clearly seen that the dye solutions have RIs larger than water (1.333 RIU at 600 nm).

The absorption bands of the dyes appear as deviations from the smooth, Cauchy-type curve (grey dashed line) fitted to the RI spectra. This fit is necessary for the next step of the transformation of RSID to molar extinction coefficient (ε), since only the RI features caused by the absorption bands of the dyes are of interest in the Kramers-Kronig relation (and the corresponding inverse variant) and since the RI spectrum, in addition to the features related to the absorption bands, contains contributions that are not related to absorption. Therefore, these parts need to be subtracted after using the Cauchy-fit to estimate it. The Cauchy-formula is commonly used as a simple description of the normal dispersion relation of transparent media in the visible regime[143], making it useful to separate normal from anomalous dispersion (where the latter is caused by the extinction of the dye). To do so, I need to note that due to the fact that the Kramers-Kronig relation contains an integral, the whole RI spectrum experiences a change because of the anomalous dispersion, which is most pronounced for the longer wavelengths[133]. The Cauchy-fit is therefore based on the section of the RI curve that is below 400 nm. Furthermore, to include the overall increase of the RI of the solution for all wavelengths due to the sheer presence of the dye molecules, I estimated this contribution to be 0.01 RIU and subtracted it from the initial fit (grey dashed line in **Figure 21d-f**) such that the

extracted contribution of the normal dispersion (grey line) happens to be lower than the baseline of the calculated RI spectrum of the dyes. A similar effect can be seen when measuring a transparent solution with NSS (like the solutions of H_2O_2 and NaCl in **Paper II**), where even without light absorption by the solute, the spectra showed a variance in amplitude for different concentrations.
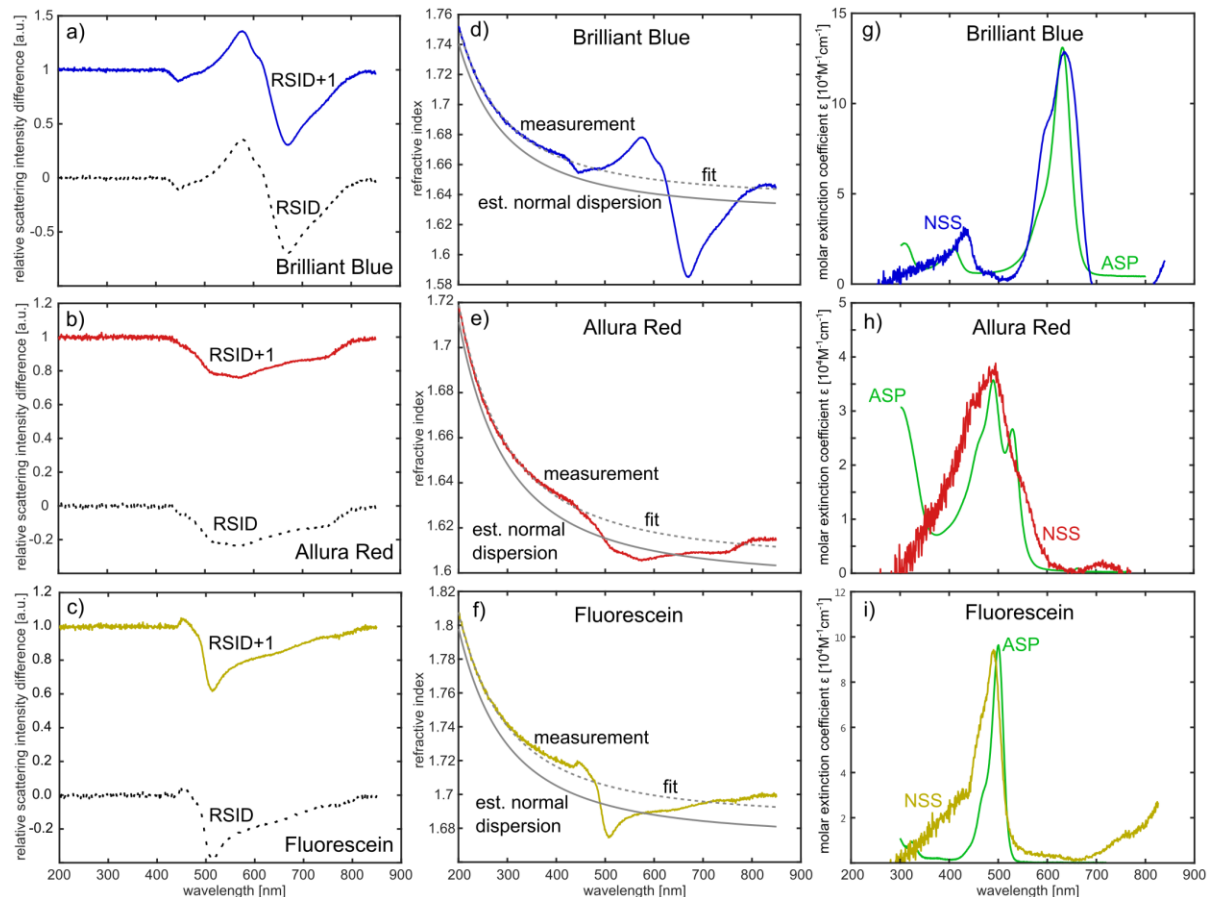

Figure 21. Translation of RSID to molar extinction coefficient. *a)-c) The RSID spectra from the NSS experiment for a 100 mM brilliant blue, allura red and fluorescein solution, respectively. The colored solid lines are RSID+1 spectra and represent the ratio of scattering cross sections, as laid out in Equation 26. d)-f) Using Equation 29, the RSID can be translated into the RI spectrum of the respective dye solution (colored lines). To extract the part of the RI spectrum that describes normal dispersion, and that is not associated with the absorption bands of the solute, a Cauchy-type fit (grey dashed line) is applied to the RI spectrum and the estimated contribution of the normal dispersion (grey line) is later subtracted from the RI curve of the solution. g)-i) Molar extinction coefficient (ε) spectra for the three dyes obtained by reverse Kramers-Kronig transformation (colored lines, Equations 30 and 31) plotted together with ε obtained for the same dyes using traditional ASP (green lines). I note the generally good agreement between NSS-based and ASP spectra. The unphysical negative molar extinction coefficients obtained by converting the brilliant blue NSS data (g) between 700 nm and 800 nm, comes most probably from the long-wavelength contribution of the anomalous dispersion to the normal dispersion that is not represented in the Cauchy-fit. The molar extinction coefficients also go below zero for all dyes below 300 nm, but here I assume that the high noise and low intensity of measured scattering is responsible for this unphysical deviation.*

38

For the dye spectra presented in **Figure 21,** the above estimate seems to be reasonable, as it is in line with my understanding of the Kramers-Kronig relation for the normal and anomalous dispersion of a dye solution and reproduces the expected result sufficiently well.

The inverse Kramers-Kronig relation for the real and imaginary part of the RI (of which the imaginary part correspond to extinction) is nearly identical in structure to **Equation 24**, except for a minus sign in front. Hence, it can be used to calculate the wavelength-dependent extinction coefficient as

$$\kappa(\lambda) = -\frac{2}{\pi} \mathcal{P} \int_0^{-\infty} \frac{\Delta n(\lambda')}{\lambda' \left(1 - \left(\frac{\lambda'}{\lambda}\right)^2\right)} d\lambda'$$

Equation 30

As the very last step, the obtained extinction coefficient spectrum, $\kappa(\lambda)$, can be transformed into $\varepsilon(\lambda)$ by using the known concentration of $c = 100\ mM$ in Equation 31 for each solution.

$$\varepsilon(\lambda) = \frac{4\pi\kappa(\lambda)}{\lambda\ c}$$

Equation 31

The final results of this calculation are shown in **Figure 21g-i**, together with $\varepsilon(\lambda)$ for the respective dyes that have been measured using ASP. The agreement is relatively good regarding the main peak positions and the maximum value of $\varepsilon(\lambda)$ for all three dyes. The values for $\varepsilon(\lambda)$ deviate from the ASP spectra slightly but I identify the main reason for this in the separation of the normal and anomalous dispersion, as explained above. Moreover, the Cauchy-fit of the RI spectrum for each respective dye solution may not represent the actual underlying normal dispersion (associated with the real part of the RI of the solution) perfectly, as it may not fully represent all involved influences of the dye extinction on the total RI of the solution. For the shorter wavelengths below 300 nm, poor signal quality due to low scattering intensity can also be considered as reason for these deviations. Furthermore, the RI of the surrounding SiO_2 plays a critical role during the calculation, as small deviations can cause a greater disagreement in the final result, since NSS is as sensitive to the RI in the channel as to the RI outside of the channel, as laid out by Equation 22 above.

4 MICRO AND NANOFLUIDICS

After having discussed single particle catalysis as well as NSM and NSS, and their potential as new experimental methods in single particle catalysis, I will in this chapter focus on the fluidics as such and on the fluidic "infrastructure" necessary to enable NSM and NSS. Specifically, I will discuss how fluids, both liquid and gas, can be controlled at the micro- and nanoscale in tiny channels nanofabricated into an oxidized silicon wafer surface in terms of flow speed, pressure and composition. Furthermore, to make theses micro- and nanofluidic systems accessible and connected to the macroscopic world, this chapter also contains a discussion of the fluidic chip holders that I have developed, spanning from early models to the fully integrated device with temperature control and electrode access that is described in detail in **Paper IV**.

4.1 Microfluidics

4.1.1 Development of Microscale Fluidic Systems

It is impossible to say when microfluidics where first used, since the flow of gas and liquids through very tiny openings is a concept that can be found ubiquitously in geological[154] and biological[155] processes, when, e.g., water transport in soil or the circulation of blood in living organisms is considered. Formally, microfluidics concerns liquid volumes in the range of 10^{-9} to 10^{-18} liters in channels with dimensions of tens to hundreds of micrometers in diameter/cross-section[156]. The active use of microfluidics in a technological sense for research and medical applications can be traced more clearly, since it has four distinct legs in the second half of the 20th century[156]. The first leg of microfluidics is rooted in microelectronics, as its success enabled the development of fabrication methods such as photolithography[157], leading to the first microfluidic devices being produced in silicon substrates before polymer substrates became the leading platform[156]. This change of substrate material was motivated by the second leg of microfluidics, which is molecular biology. The revolutionary field of genomics[158], which rose to prominence in the 1980s, required bio-compatible high-throughput devices for microanalysis and DNA sequencing. The third leg is associated with the genomics one but concerns a much more somber topic, as a series of programs was launched in the 1990s to develop field-deployable testing devices for chemical and biological weapons. The funding and initiative provided there sparked the rapid growth of academic interest in microfluidics[156]. The fourth leg is rooted in the already existing technologies that utilized microscale analysis technologies, namely capillary electrophoresis[159], liquid chromatography[160] and of course gas chromatography[161].
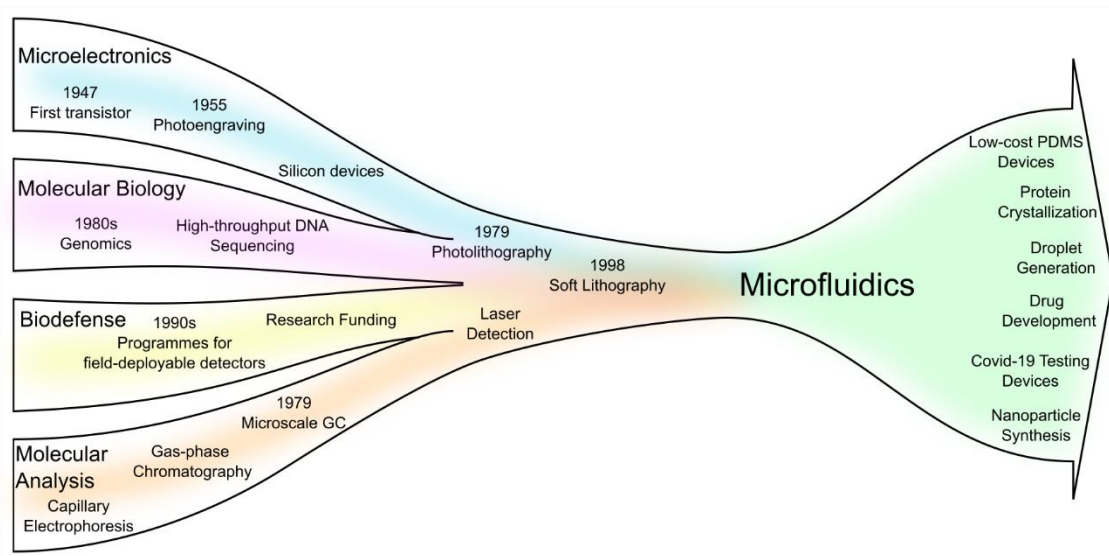
Figure 22. *Overview of the origins and applications of microfluidics. This scheme has been created with the reviews on microfluidics provided by Whitesides[156] and Niculescu et al.[162] The mentioned applications are exemplary and do not fully represent the extensive field of microfluidics.*

Microfluidics does not only reduce the sample volume, i.e., the amount of an analyte- or reactant-containing liquid required/handled by a device, it also provides unique flow characteristics. On a larger scale, the inertia of a liquid would be determining the flow behavior and create turbulent, convective flow[156]. On the microscale, however, viscosity is of greater importance, which leads to laminar flows in microscale channels. This characteristic of a controllable, laminar flow was critical to the work presented in this thesis and the attached publications – especially in **Paper I** for the assessment of flow and diffusion via NSM, in **Paper III** for the creation of a separated liquid volume, and in **Paper IV** where exchange and mixing of solutions is demonstrated. Furthermore, microfluidics offer a broad range of liquid control beyond convective flow, since for example pressure valves[163] and electro-osmotic flow[164] can be integrated into a fluidic system.

4.1.2 Applications in Biology and Chemistry

Since its emergence[162] in the 1990s, microfluidics has been introduced into various fields of research and industry. Nevertheless, it most probably has gained its most prominent foothold within biology and medicine[156,162] where the use of polymer substrates, such as Polydimethylsiloxane (PDMS), enabled rapid and low-cost fabrication[162] of relevant devices with a low threshold for prototyping. Furthermore, the usable temperature range, the optical transparency, low toxicity and high permeability to molecular oxygen and carbon dioxide[156] have made PDMS an ideal candidate for biological and medical applications. Specifically, in these fields microfluidic devices are used, e.g., for the investigation of protein crystallization[165], drug development[166], single cell/molecule manipulation[167] and droplet generation[168] to name only a few applications.

42

When it comes to applying microfluidics in chemistry, its impact has not (yet?) been as deep. George Whitesides named in his seminal review article on the topic[156] two main reasons for this: (i) microfluidic devices are not as easily adaptable as established setups such as distillation or Schlenk lines, and (ii) the often used PDMS substrate lacks chemical resistance, especially when organic solvents are considered. However, the continued improvement and development of fabrication techniques gave rise to chemical microscale reactors with higher(er) resistance that use, e.g., Teflon, stainless steel, glass and silicon-SiO_2 as substrates[169]. Enabled by this development of chemically resistant microfluidic systems, the combination of colloidal metal (catalyst) nanoparticles and microfluidics is a rapidly growing field, both in terms of particle synthesis and particle characterization. In their comprehensive review of this field, Solsona et al.[169] have listed various characterization methods for nanoparticles in microfluidics, such as mass spectrometry[102,170,171], X-ray scattering and absorption spectroscopy[20,172], plasmonic scattering spectroscopy[29,31,173] and UV-Vis spectroscopy. Furthermore, they listed a plethora of approaches that use microfluidics to synthesize colloidal metallic and non-metallic catalyst nanoparticles using either homogeneous flow, segmented flow or droplet generation as synthesis scheme. To this end, while I in my work so far have relied on nanoparticles lithographically fabricated into the fluidic system of choice (**Paper III**) or on *ex situ* synthesized colloidal particles subsequently trapped inside the fluidic system (**Paper I**), I foresee the *in situ* synthesis of catalyst particles inside fluidic structures in combination with NSM/NSS assessment of their catalytic activity as an interesting future research direction.

4.2 Nanofluidics

4.2.1 Characteristics of Nanoscale Fluidic Systems

It is logical to describe nanofluidics as the natural evolution of microfluidics in the wake of the constant improvement of micro- and nanofabrication techniques driven by Moore's law in microelectronics. Similar to microfluidics, nanofluidics describes flows in and around *nano*scale objects[174], usually defined as ranging from below 5 nm up to around few 100 nm[175]. It too can trace its origins to the late 1990s and early 2000s as discussed in reviews on the topic by Eijkel et al.[174] and Robin et al.[176]. Similar to microfluidics, the initial driving forces behind the development of this field were the desire to understand nanosize effects in biology and biophysics, such as physiology on the cellular level (ion channels, aquaporins and filtration), genetics and single molecule studies. However, the overview in **Figure 23** makes it clear that even purely physical effects, such as surface interactions and thermodynamics, are studied using nanofluidic systems, as are bio- and nanoengineering questions and chemistry on the nanoscale.
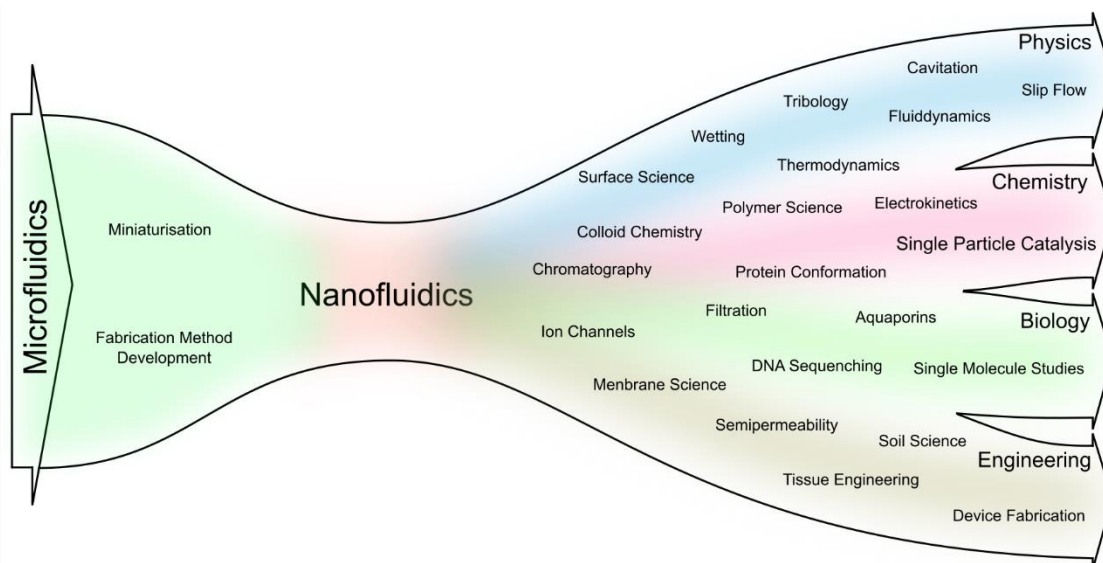
Figure 23. *Overview of the disciplines of nanofluidics. The separation into the branches of Physics, Chemistry, Biology and Engineering is not always valid, as many applications are used in an interdisciplinary context. Scheme adapted from Eijkel et al.*[174]

Importantly, however, despite nanofluidics having evolved from microfluidics it is inaccurate to describe nanofluidics just as microfluidics on a smaller scale. The reason is that at the nanoscale, a plethora of fluidic, molecular and electrostatic effects are emerging that can alter the behavior of fluids significantly[177]. This is understandable, since beyond a certain point a fluid can no longer be treated as a homogeneous bulk system but needs to be considered at the molecular level. For water as example, which has a molecule size of 3 Å, such effects can become eminent below 2 nm of pore size[178]. To this end, several length scales have been defined to categorize the effects that set nanofluidics apart from microfluidics, and I would like to showcase here a few.

The *Bjerrum-length* describes the scale at which direct electrostatic effects dominate over thermal effects. This could, for example, mean that an ion cannot enter a certain pore since its hydration layer is too big. Similarly, the *Gouy-Chapman-length* describes at which length the electrostatic wall-ion interaction overcomes thermal energy. The *Debye-length* describes the deviation of ion concentration close to a channel wall due to its charge, and it can vary between 3 Å (high ion concentrations) and 30 nm (low concentrations)[178]. These scales only consider electrostatic interactions of ions, the description of dynamic properties of the fluids, such as surface friction and slip-lengths, require an even deeper understanding of actual nano*fluidics*.

An important conclusion from the above is that the lengths scales at which these effects occur are below ~30 nm. Considering the definition of nanofluidics as structures in the size range of few 100 nm and below, this means there is a regime in which these effects are expected to be negligible, as exemplified in the excellent review by Bocquet et al. who, e.g., state that there are no deviations from the bulk Navier-Stokes equation expected for confinements larger than 1 nm, and that the Reynolds-formula and the bulk viscosity are valid down to this size regime[178]. Projected onto my work, this means that there is a window in which fluids can be controlled at the nanoscale, while still behaving bulk-like. Since the fluidic structures that I have used typically are in the 100 nm size regime, it is indeed this range that I have operated in. Accordingly, e.g., the diffusion constants determined in **Paper I** for H_2O_2 in water were

indeed found to be perfectly in line with the literature values for the bulk. This means that the use of nanochannels combined with NSM/NSS for single particle catalysis indeed is a new application of nanofluidics which, as the key point, uses the nanochannels only as a tool to confine the particles and the catalytic reaction, as well as enable the optical effects specific to NSM/NSS, without invoking significant nanoscale fluidic effects.

4.2.2 Fabrication of Fluidics in Silicon-SiO$_2$-based Substrates

In the previous section, I laid out how micro and nanofluidics emerged from, among others, silicon-based microelectronics. In the following, I will give an overview of how the fluidic SiO$_2$/Si chips that I have used in my thesis are fabricated in the clean room environment of the MC2 Nanofabrication Laboratory at Chalmers. While it is a true "luxury" to be able to design and fabricate nanofluidic devices with intricate functionalities, it does come with the significant drawback (when compared to polymer substrates) that a clean room environment with a range of specialized and delicate tools is required.

As a common denominator, all fluidic systems used and built for my work are designed as 2D-layouts, meaning that neither over- nor undercrossing of fluidic channels is possible. In the most basic version as shown in **Figure 24**, such fluidic systems feature two microfluidic channels that constitute the in- and outlet system of the chip. They are connected to the macroscopic fluidic periphery of the chip holder (**Chapter 4.3**) at their end points, and to a set of straight and parallel nanochannels in their center. In this design, the microchannels are used to transport fluids to and from the nanochannels, with one microchannel being upstream (at the entry or inlet side of the nanochannels), while the other microchannel is on the downstream side (exit or outlet of the nanochannels). On both the inlet and outlet side, they are connected to circular reservoirs that are used for filling the fluidic system with the desired liquid. Note that in this way two different liquids can be applied on either side of the nanochannels.
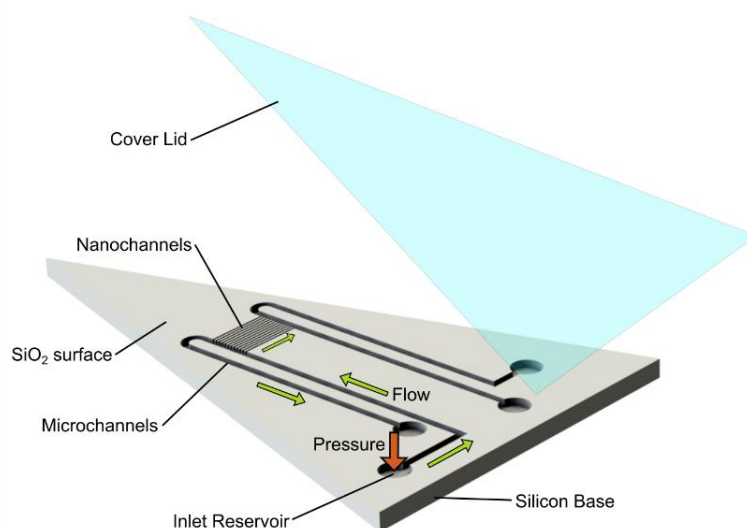

Figure 24. *Rendition of a basic nanofluidic chip. Here, four inlet/outlet areas are connected via microchannels to a set of parallel straight nanochannels located at the tip of the triangular chip comprised of a thermally oxidized silicon wafer, into whose thermal oxide the fluidic system is fabricated and hermetically sealed by a thermally bonded glass lid for optical transparency. Flow of liquids or gas is induced by pressurizing one of the reservoirs using N$_2$ gas.*

The micro- and nanofabrication approach used for all fluidic systems in this work is based on so-called nanolithography processing into thermally oxidized silicon (circular 4-inch wafers), followed by the sealing of the fluidic structures by thermally bonding glass wafers (Borofloat 33, 4 inches, 175 µm thick) onto the structured substrate (**Figure 25**). This provides both a hermetic seal and optical access (via e.g. dark-field microscopy) to the fluidic systems from the side of the lid.

The micro- and nanofabrication process consists of the following steps:

1. Silicon wafers with (100) orientation were cleaned with a standard process. For this purpose, the wafers were first treated in SC1 (5:1:1 $H_2O:NH_3OH:H_2O_2$, 80°C) for 10 minutes, rinsed in deionized water, native oxide removed with 2% HF (10 seconds), rinsed again in deionized water, then treated in SC2 (5:1:1 $H_2O:HCL:H_2O_2$, 80°C) for 10 minutes, rinsed a final time in deionized water and then spun dry.

2. The cleaned wafers were thermally oxidized in an oxidation furnace in a water atmosphere at 1050°C until an oxide thickness of 200 nm was reached.

3. In the next step, nanochannels were etched into the thermally grown oxide using reactive ion etching (RIE). For this, a 20 nm thick structured Cr layer was used as a hard mask due to its high etch resistance against the NF_3 plasma used for nanochannel etching. This mask was structured by preparing a 200nm thick layer of electron beam resist (ARP6200) in which the nanochannel pattern was written by electron beam lithography (development in o-xylene). This pattern was then transferred into the Cr- layer (the hard mask) with RIE using chlorine (Cl_2) before this mask was used for the SiO_2 etch.

4. All larger microfluidic structures were etched into the surface using RIE. For this purpose, an etching mask made of photoresist was used, which was typically structured using direct laser lithography (DLL).

5. For nanofluidic chips with lithographically placed nanoparticles (**Paper III**), the nanoparticles were defined at this stage with electron beam lithography (EBL) in a double layer of resist (copolymer and PMMA) spun onto the structured substrate, and the material of choice for the nanoparticles was deposited with electron beam evaporation through the holes in the resist mask. Finally, the resist mask was dissolved in acetone leaving only the nanoparticles at the defined positions on the substrate.

6. The substrates were thoroughly cleaned with SC1 (5:1:1 $H_2O:NH_3OH:H_2O_2$, 80°C) for 10min followed by a rinsing step in DI water and blow drying with N_2. Glass wafers of 175 µm thickness were cleaned in the same manner, O_2-plasma treated (50W RF power, 250 mTorr) together with the processed substrates.

7. The fluidic system was then hermetically sealed with the lid using fusion bonding at 550 °C for 5 h. The access holes to the microchannels were etched through the silicon wafer substrate using deep reactive ion etching (DRIE). For the fluidic chips used in **Paper II** (see **Figure 26,** Chuck D), connections to the fluidic systems were sandblasted through the cover glass before bonding. The finished wafer was then diced into single fluidic chip, with a stepped edge in the later versions (**Paper IV**).
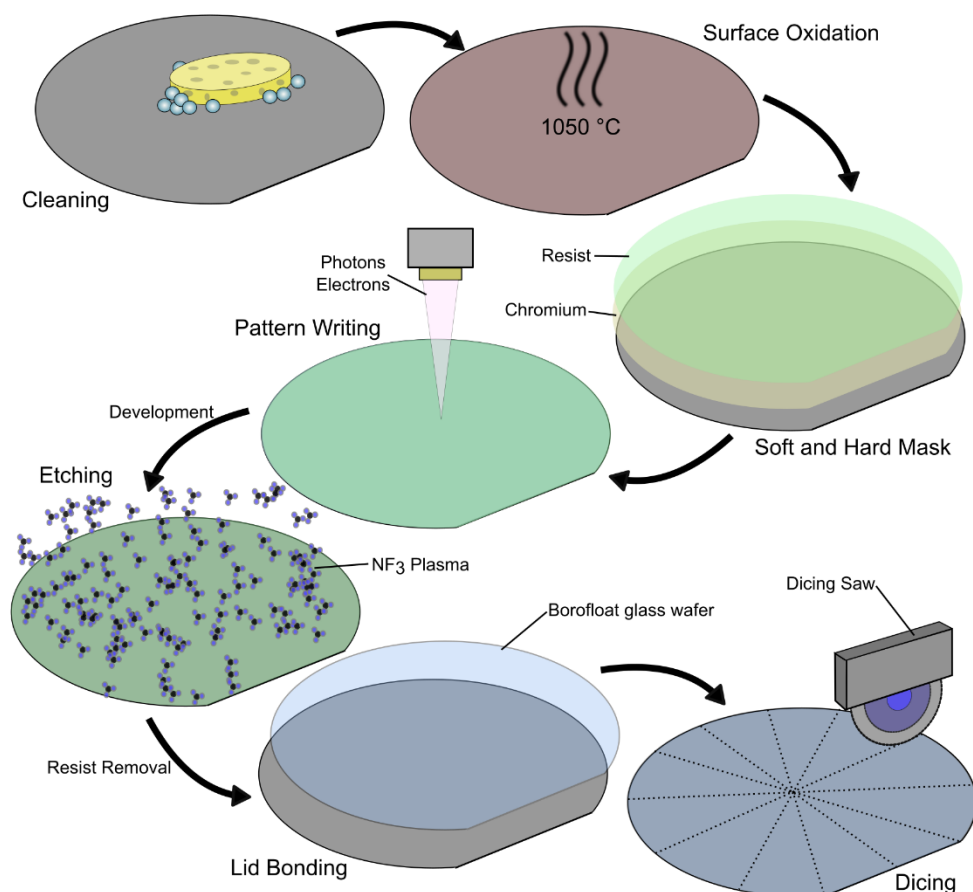
Figure 25. *Simplified scheme of fluidic chip fabrication. The 4-inch silicon wafer is first thoroughly cleaned with SC1, has its native oxide removed with 2% HF and is cleaned again with SC2. Then, a thermal oxide layer (200 nm) is grown on the surface using a furnace in wet atmosphere. Subsequently, a chromium hard mask layer is evaporated on the chip, followed by spin coating of a polymer resist layer (e.g. PMMA for electron beam lithography, 100 nm to 500 nm). The desired fluidic pattern is written in the resist by electron beam or photolithography, and subsequently transferred to the Chromium with a Chlorine etch. The pattern in the Cr hard mask is then etched into the SiO_2 using HF_3 plasma. Finally, a glass lid is thermally bonded to the wafer, and the individual fluidic chips are cut from the wafer using a dicing saw.*

4.3 Connecting Nanoscopic to Macroscopic Fluidics

4.3.1 Development of Fluidic Chip Holders

In the previous sections of this chapter, I focused on the micro- and nanofluidic structures on the silicon-based fluidic chip. However, while these chips indeed are the foundation for NSM and NSS, as well as for the single particle reactor schemes presented in this work, they are only a part of the overall experimental setup that enabled the experiments that I have performed. The device that holds these fluidic chips – the chip holder or "chuck" – is, in fact, (almost) equally important since it is its form factor and the number of fluidic connections provided that define which fluidic systems can be realized on the fluidic chip.
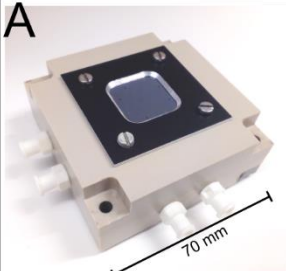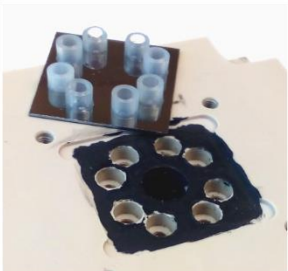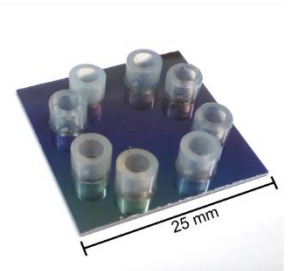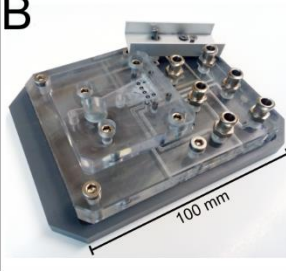
47
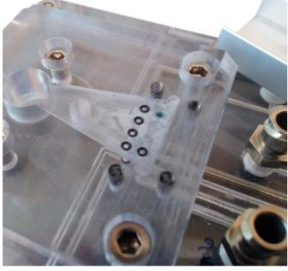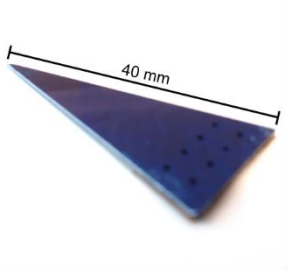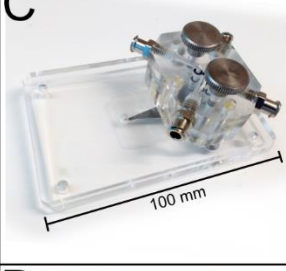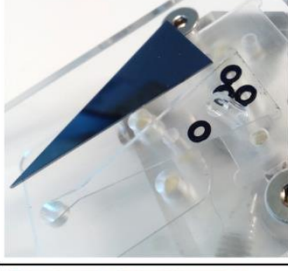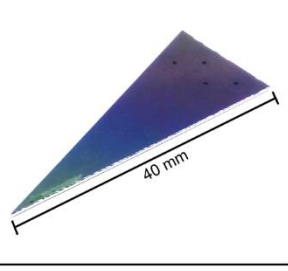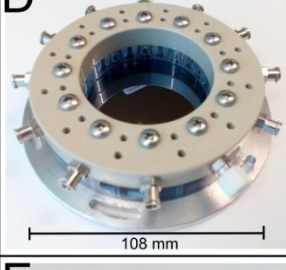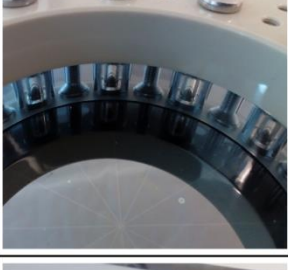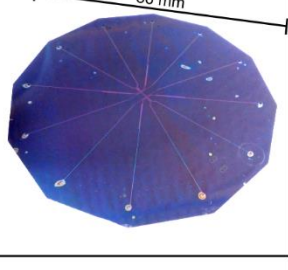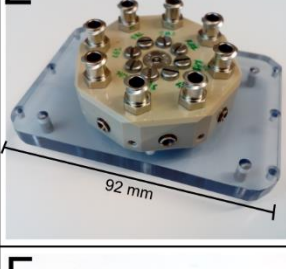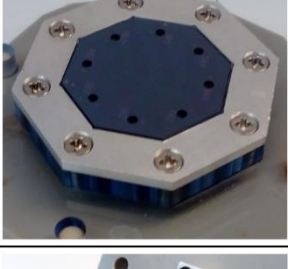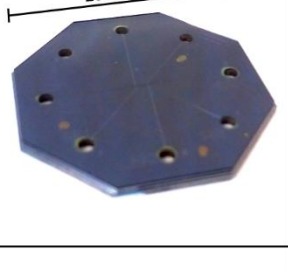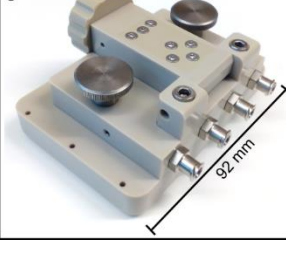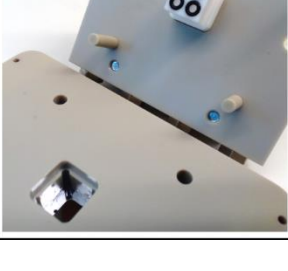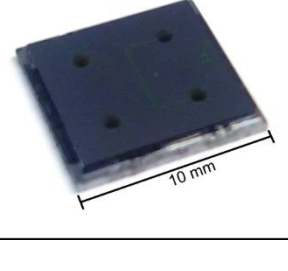
Overview	Detail	Fluidic Chip	Features
A 70 mm		25 mm	• PEEK, Aluminum • 8 connection points • Quadratic chips • 4 chips per wafer • Upright microscope • PVC reservoirs
B 100 mm		40 mm	• Polycarbonate (PC) • 8 connection points • Triangular chips • 16 chips per wafer • Upright microscope • PC reservoirs
C 100 mm		40 mm	• Polycarbonate (PC) • 4 connection points • Triangular chips • 16 chips per wafer • Inverted microscope • Glass reservoirs
D 108 mm		86 mm	• PC, PEEK, Aluminum • 12 connection points • Dodecagonal chips • 1 chip per wafer • Upright microscope • Glass reservoirs
E 92 mm		23.8 mm	• PC, PEEK, Aluminum • 8 connection points • Octgonal chips • 4 chips per wafer • Inverted microscope • Glass reservoirs
F 92 mm		10 mm	• PEEK, Teflon • 4 connection points • Quadratic chips • 52 chips per wafer • Inverted microscope • Teflon reservoirs

Figure 26. *Overview of chip holders used during my thesis.* *Key features are listed. All designs were for Si/SiO₂ fluidic chips.*

48

While the most advanced chuck I have developed is discussed in detail in **Chapter 5** and **Paper IV**, I would like to use this section to provide an overview of the chip holders that I have used throughout my thesis work, and how they have evolved from each other, to note down the key insights I have gained along the way.

Figure 26 summarizes the fluidic chip holder designs that I have worked with in this thesis, except for the newest one presented in **Paper IV**. Chuck A is our earliest design, where we used PVC-reservoirs glued to the backside of the fluidic chip to establish a leak-tight connection to the rest of the chuck. While principally functioning well, the glueing procedure is inconvenient. Hence, from chuck B forward, we used O-rings instead to make it easier to exchange the fluidic chips. The chips now also had a triangular shape to increase the chip yield per 4-inch silicon wafer to 16. In chuck B, the fluidic chip rests in a socket that also houses the eight O-rings that seal the connection between the micro- and the macrochannels in the polycarbonate (PC) part of the chuck (PC was chosen due to ease of machining and optical transparency) at the positions of the total eight connection points. The necessary mechanical pressure is provided by a metal bar screwed across the lower end of the chip. The exchange of liquids is enabled by detaching the upper part of the chuck together with the chip to access the liquid reservoirs integrated in the chuck. However, since the reservoirs also were machined in PC, the main drawback of this chuck was its incompatibility with organic solvents[179].

Chuck C was built for an inverted microscope (rather than an upright one as in the case of chuck B), which as the main implication meant the chip could remain in place while liquids were exchanged. Furthermore, we reduced the number of fluidic connection points to four to enable the use of larger (and thus easier to handle) O-rings. Two additional major development steps were implemented: (i) the chip could remain in position on the microscope table while the liquids in the reservoirs are exchanged and (ii) the reservoirs were small glass tubes inserted into the PC-body of the chuck (see detail picture for Chuck C in **Figure 26**) to increase chemical robustness. With this chuck, I performed the measurements for **Paper I**.

The next model, Chuck D, was a clear commitment to increasing the functionality of the fluidic system(s) on the chip, and it was designed to be compatible with an upright optical microscope that is equipped not only with a camera but also a spectrometer, as necessary for NSS. We achieved this by arranging 12 connection points with large glass tube reservoirs in a circular fashion, and by providing access to each of these reservoirs individually via an opening that can be sealed by a screw to enable pressurizing the connection point via a side port. I used this chuck for the measurements performed for **Paper II**, since the 12 connection points enabled the introduction of the optical referencing scheme for NSS explained in section 3.2.3. As its main limitation, this chuck was designed for fluidic chips that encompassed an entire 4-inch wafer, which dramatically reduced the yield of the nanofabrication.

Chuck E can be seen as a downscaled version of Chuck D using the same type of reservoir but adapted for use on an inverted microscope. It features only 8 connection points per octagonal fluidic chip. However, since the chips as such therefore can be made significantly smaller, four chips now fit on a 4-inch wafer and thus increase the fabrication yield. Furthermore, here we introduced one important new feature to the fluidic chip design – a stepped edge. This made it possible to clamp the chip on this edge and thereby create an unobstructed surface in the focal plane of the microscope objective. This detail is important since it significantly decreases the

risk of collision between chip and objective and enables the inspection of the whole fluidic system under the microscope. The measurements in **Paper III** were performed with this chuck.

The next step in chuck development, Chuck F, was driven by the need to access the liquid reservoirs at the connection points even more easily, while significantly increasing the stepped edge chip yield per 4-inch wafer to 52. This was achieved by dramatically shrinking the size of the chips to 10 mm x 10 mm, and by reducing the number of connection points per chip to four. Furthermore, the chuck itself was machined in highly chemically resistant PEEK and designed such that it features an easy-to-open lid with an integrated Teflon block that holds the O-rings and liquid reservoirs with pressure connections. While I have not used this chuck actively in my work, it is widely used by my colleagues in the group and its development was instrumental for arriving at the last design of the highly integrated chuck I have developed and present in detail in **Chapter 5** and **Paper IV**.

As a final note regarding previous chuck development, I would like to highlight that the later designs are built with an inverted microscope in mind. The advantage of an inverted microscope is primarily that the backside of the fluidic chip is freely accessible, e.g. not obstructed by the objective, illumination path and eyepiece, which greatly expands the possibilities of chuck design. In such chucks, the liquid containing reservoirs are placed above the connection points of the chip, such that gravity works in favor when solutions are introduced or exchanged. Furthermore, having the channel side of the fluidic chip face down means that the connection points can be etched in from the backside of the Si-chip, which creates cleaner openings to the fluidic chip, preventing thereby clogging, as discussed further below.

This overview showcases that the development of any micro- and nanofluidic technology not only involves the design of the fluidics themselves but also of the necessary macroscopic periphery systems integrated in the chip holder, and how they mutually influence each other. To this end, while I was not deeply involved in the design of the chucks presented above, they were crucial for the development and understanding of fluidic systems of my thesis, and "culminated" in the development of my own chip holder presented in **Paper IV**. This chuck, as point of comparison, enables the use of 10 mm x 10 mm step edge chips with 12 connection points, as well as their temperature control and connection to electrodes to establish electric field across the fluidic system. It is discussed in detail in **Chapter 5**.

4.3.2 Challenges Along the Way

While the papers included in this thesis present in-depth the most important positive results of my work and the knowledge gained from them, I find it of equal importance to communicate here some of the key challenges I faced along the way. Specifically, I will briefly discuss: (i) thin-film interference effects caused by the Si/SiO$_2$ chip design and (ii) clogging of fluidic channels.

Thin-film interference in Si/SiO₂ fluidic chips

The key ingredient in Si/SiO$_2$ fluidic chips is the thermal oxide layer on the Si wafer, into which the fluidic system is fabricated. As long as no dark-field optical microscopy/spectroscopy measurements are concerned, the thickness of this oxide layer will essentially only be determined by the targeted depth of the fluidic system. However, as soon as light is irradiated onto such chips, interference effects between light scattered from the SiO$_2$-channel and reflected from the Si-SiO$_2$ interface must be considered if the thickness of the thermal oxide is on the order of the wavelengths of visible light. This becomes clear when comparing two dark-field scattering spectra measured from a 150 nm by 150 nm channel etched into 2 µm and 200 nm thick thermal oxide, respectively (**Figure 27a**). The comparison reveals a distinct fringe-like modulation of the scattered light intensity in the case of the 2 µm thick oxide, whereas the channel scattering spectrum measured for 200 nm thick SiO$_2$ essentially only contains the spectral feature characteristic for the halogen light source used for illumination, modulated by the optical components of the microscope. To substantiate this, I also calculated how the amplitude of vertically incident white light (λ = 300 nm to 800 nm) is modified by thin-film interference following Gungor et. al.[180], assuming n = 3.88 as the RI of silicon[181] while neglecting its extinction, and n = 1.4585 as the RI[141] of SiO$_2$, for 2 µm and 200 nm thick SiO$_2$ films on Si without nanochannels (**Figure 27c**). The theoretically obtained fringe pattern matches quite well with the experimental data for 2 µm thick oxides and also corroborates the absence of a distinct interference peaks in the wavelength range of interest for my experiments, i.e., between 450 and 800 nm, for the case of 200 nm thick oxide. As a consequence of this analysis, we eventually opted for 250 nm oxide thickness for the fluidic chips used in my work, since it constitutes the best compromise between suppressing interference modulation of the light scattering intensity from my samples and enabling the targeted 200 nm fluidic system depth.

As a final note, I want to mention that this interference effect not only constitutes a problem but that it potentially can be actively explored to, e.g., suppress and enhance specific wavelengths of light scattered from a nanofluidic surface, for example when specific nanoparticles or dyes with distinct absorption bands are to be investigated. This may yield an interesting application in the future.
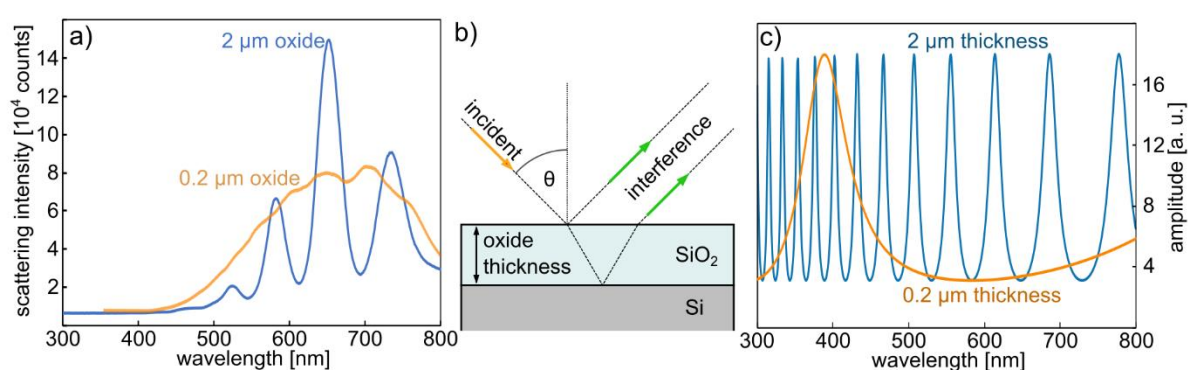

Figure 27. *Thin-film interference on fluidic SiO₂-Si chips. a) Nanochannel scattering spectra for a water-filled nanochannel etched into 2 µm thick SiO₂ (blue line) and etched into 0.2 µm SiO₂ (orange line). b) Schematic depiction of the principle of thin film interference. c) Calculated fringe patterns for SiO₂ layers of 2 µm and 200 nm thickness on a Si surface (without nanochannel).*

Mitigating micro- and nanochannel clogging

The obstruction of fluid flow through micro and nanochannels is known as clogging and highly detrimental to any fluidic experiment. Usually, it renders the fluidic chip useless, even though it might be possible to remove the clogging by applying high pressures to enforce flushing out of the clog, by flushing with organic solvents to potentially dissolve organic contamination, or by soaking the fluidic chip in harsh chemicals such as "Piranha" solution, a mixture of H_2O_2 and H_2SO_4[182]. Since clogging is a constant worry in the fluidics field, it has sparked specific investigations, as for example the studies by Dersoir et al.[183] and Massenburg et al.[184]

In my work, nanochannel clogging issues have occurred multiple times and differently for different experiments and chip designs. Compared to other studies, however, I had one particular advantage and that is that NSM/NSS enabled me to directly see any particles or contamination inside the fluidic system, as previously discussed in section 3.2.2. This is seen in **Figure 28a**, where in many of the otherwise continuous 200 nm x 200 nm cross section nanochannels bright spots appear at certain positions, which means that they are partly or fully blocked. The image shown here is from a series of tests for **Paper III**, where a 50 mM fluorescein solution was mixed with a HCl solution at a pH of 1.3 in the nanochannels. This caused a decrease in fluorescein solubility, leading to the precipitation of protonated fluorescein in the nanochannels, which could be removed again by continuous flushing with water.
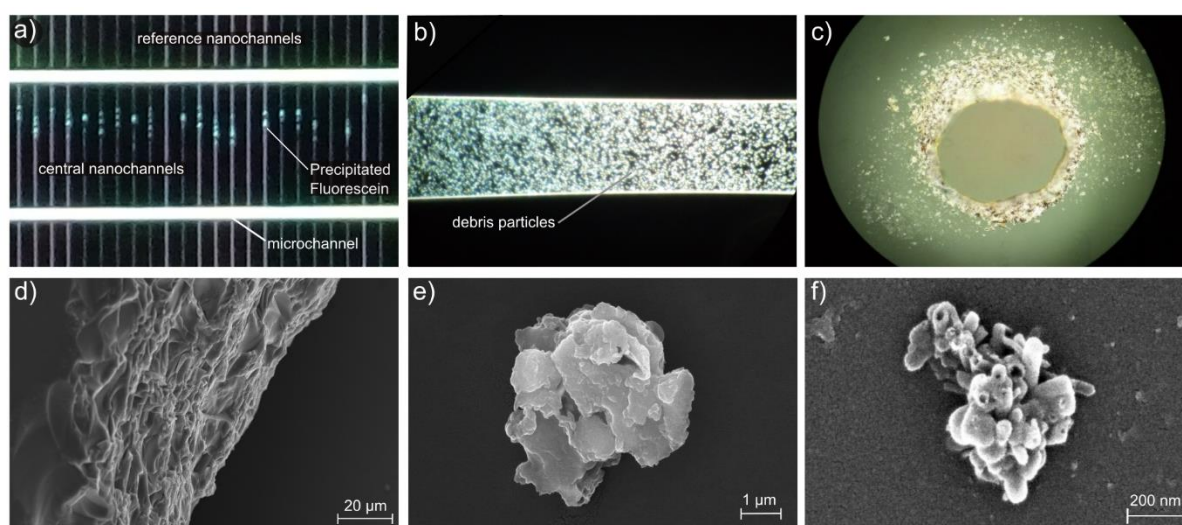
Figure 28. *Clogging of nano and microchannels. a) Dark-field image of a nanochannel reference system (cf. **Figure 20**) where the upper microchannel is filled with a 50 mM fluorescein solution, while the lower microchannels contain diluted HCl at pH 1.3. The mixing of the two solutions caused the fluorescein to precipitate in the nanochannels. b) Dark-field image of a microchannel (50 μm by 1.2 μm), filled with a large number of "debris" particles. c) Dark-field image of the sandblasted inlet hole in the glass lid that reveals its rough and cracked surface. d) SEM image of the side wall of an inlet hole that was sandblasted through the Borofloat 33 cover glass used to seal the chip. e, f) SEM images of examples of particles found in the inlet holes.*

While it indeed is the nanochannels that are most prone to clogging, it also may happen in the larger microchannels (**Figure 28b**). Such an example occurred during the experiments for **Paper II**, with "debris" particles appearing in large numbers in the microfluidic inlet system

after a certain time of chip usage. While other samples never had shown any signs of this type of clogging this severe case occurred when using chips fabricated for Chuck D shown in **Figure 26**.

A detailed and systematic search for the origin of the debris particles eventually identified the inlet holes of the chip sandblasted through the glass lid as the culprit (**Figure 28c**). This sandblasting step was necessary because the construction of Chuck D (cf **Figure 26**) required the connection points to the fluidic system to be on the same side of the chip as the micro- and nanochannels. Since the material of the lid bonded to this side was Borofloat 33, and since no laser-assisted etching[185,186] was available in the clean-room facilities, a mechanical method such as sandblasting had to be used. Corresponding SEM images revealed that the walls of the cylindrical hole had a very rough structure (**Figure 28d**). Furthermore, SEM images of debris particles extracted from a chip revealed a structure reminiscent of shattered amorphous material, such as glass (**Figure 28e**), with various shapes and sizes, where the smallest particles were in the size range of 400 nm to 200 nm (**Figure 28f**). Furthermore, I had observed that the largest number of particles occurred after a chip had not been used for a while, indicating that the debris had accumulated over time in the inlet holes.

This finding influenced significantly our further work and development on all levels, as it essentially aggravated the use of Chuck D with 12 connection points for further experiments. Specifically, it sparked the development of the chip holder discussed in detail in **Chapter 5** and **Paper IV**, and locked fluidic chip fabrication to designs where the connection holes are wet-etched through the bulk of the Si substrate from the backside, rather than sandblasted through the glass lid. Consequently, this also advertised the use of inverted microscopes such that the inlet holes in the Si would face upward, while the glass lid providing optical access to the fluidic system faces downward. The following and last chapter of this work is therefore dedicated to summarizing my development of (i) a new fluidic chip design; (ii) a corresponding versatile chip holder, where the learnings presented in this chapter are implemented.

5 EXPERIMENTAL SETUP DEVELOPMENT

In the previous chapters of this thesis, I laid out the principles of heterogenous catalysis, which I aimed to investigate (**Chapter 2**), the method I have developed to investigate single catalytic nanoparticles in nanochannels (**Chapter 3**), and the basics of micro and nanofluidics needed to operate the experimental setup (**Chapter 4**). In this final chapter, this is combined to create a versatile fluidics platform enabling a continued investigation of individual nanoparticles for catalysis with a broad range of experimental options. This includes the chuck itself, as well as the microscopy setup used for future experiments.

5.1 Framework of Requirements and Limitations

The task of creating a new fluidic platform that not only enables NSM/NSS, but also combines all the positive features of the chucks shown in the previous chapter while extending the experimental capabilities can be seen as the search for the optimum between what is desired and what is possible. To illustrate this in detail, I will list here the main boundary conditions.

Requirements to the new setup

1. <u>Silicon-based micro and nanofluidic chips</u>. The experience of nearly a decade[102] concerning fabrication strategies for fluidic systems in this substrate has given my group the necessary insight to realize new and complex designs. A fluidic system embedded in SiO_2 has the necessary chemical inertness while the transparent lid enables the use of optical microscopy and spectroscopy.

2. <u>Chip format of 10 mm by 10 mm.</u> This size allows the fabrication of up to 52 fluidic chips per 4-inch wafer, while still being big enough to house multiple fluidic systems. Furthermore, we aim to make this a standard size, at least within our group.

3. <u>12 fluidic connection points.</u> While working with various chuck designs, it became evident that the more functional and complex fluidic systems required more than just 4 connection points per system. A higher number of connections unlocks a much greater number of possible fluidic designs, may it be reference systems (**Paper II**) or mixing of solutions on chip (**Paper IV**).

4. <u>Use of an inverted dark-field microscope.</u> To allow comfortable access to the fluidic chip and have the fluid-containing reservoirs above the chip, an inverted microscope has proven to be beneficial. This also means that the connection holes in the chip can be etched from the backside, minimizing the risk of clogging as explained in section 4.3.2. This microscope needs also to be very stable for long-term measurements.

5. <u>Integration of temperature control.</u> The main purpose of the new setup is the investigation of single particle catalysis, where the ambient temperature plays a critical role for the energy landscape of a catalytic reaction. Furthermore, biological applications, such as protein folding, or diffusion in nanochannels are fascinating prospects to be investigated at different temperatures.

6. <u>Implementation of electric fields.</u> Nearly all species in a fluidic system (in the liquid phase) carry a charge, may it be metal nanoparticles or ions of solutes. The spatial control of these (as already shown in **Paper IV**) is very promising in terms of particle placement, electrophoresis in nanochannels[187], electro-osmotic flow[188] and even field effect nanofluidics[189].

Limitations to the new setup

1. <u>Size of commercially available O-rings.</u> The sealing of the connection between the chip holder and the fluidic chip itself is best done with O-rings, which can be produced in different materials depending on the desired chemical resistance. These O-rings can readily be bought from a range of suppliers, but only down to a certain minimum size. This determines how the connections can be arranged on the fluidic chip.

2. <u>Length of available syringe needles.</u> The best way we have found to place a sufficient amount (several microliters) of solution in the reservoirs of the chip is by using blunt syringe needles that can be bought in large quantities. But since they are not produced with research in mind, but rather for medical applications, the range of choice is limited when it comes to length and diameters, especially for blunt needles.

3. <u>Means to heat or cool the setup.</u> While a fluidic system can be heated relatively easily with an electric heater placed on the chip[32], the options for cooling are limited. The components commonly used for this in small-scale setups are Peltier-elements. They create sufficient temperature gradients but generate a large amount of excess heat due to their electric current based principle.

4. <u>Individual access to the reservoirs.</u> Some experiments require parts of the fluidic system to stay pressurized while liquids in others are exchanged, for example to avoid contamination by back-flow. Access to the reservoirs must be simple and preferably possible with one hand.

5. <u>Size constraints of the microscope table.</u> The chip holder needs to fit in the sample frame of the inverted microscope (see **Paper IV** for details), which limits the possibilities of the construction.

6. <u>Choice of materials.</u> The materials that are in contact with chemicals need to be resistant to them while also mechanically stable. Parts of the chip holder need to able to transport heat away from the Peltier elements.

7. <u>Manufacturability.</u> While the conceptualization is a rather creative process, the realization is bound to the available machining techniques and manufacturers.

5.2 Creation of a New Setup

5.2.1 Developing a Multifunctional Fluidic Chip Holder

The constraints listed above necessitated the modeling of a series of chip holder prototypes that each by itself could fulfill the requirements and were feasible from a manufacturing point of view. However, the need for simplification required a continuous remodeling and rethinking of the chuck. Below, I list the most important development steps that I have taken, as documentation of my research but also as possible alternatives should the set of requirements and limitations change in future chuck designs.

The first draft of a new chuck shown in **Figure 29** resembles in structure Chuck E and F (**cf. Figure 26**) as there are separate access (green) and pressure (cyan) ports for each of the 12 connection points on the fluidic chip. In this draft, the access points are arranged on the edges of the backside of the fluidic chip, 3 connections per side. The main invention step here was the use of angled access channels (and with that reservoirs) above the chip.
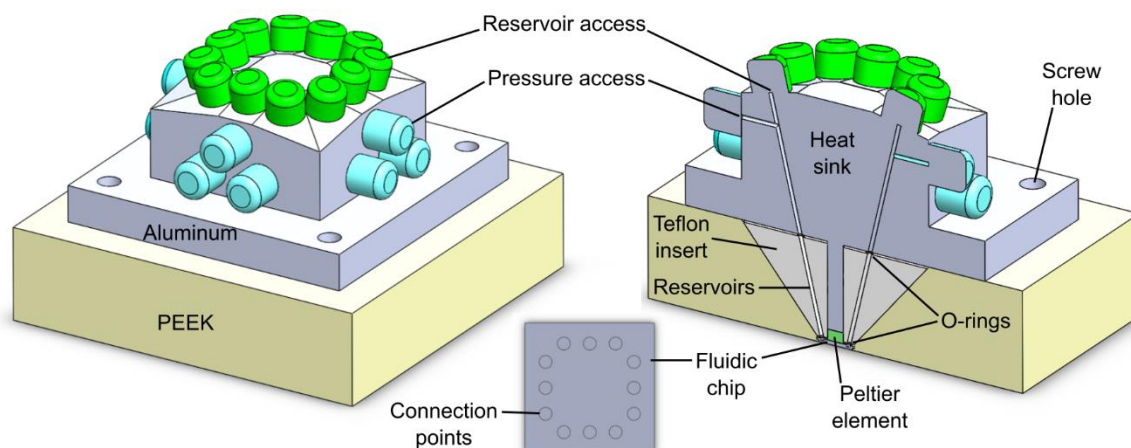
Figure 29. *Chip holder development stage 1.*

This was motivated by the idea to use Luer-lock connections between the chuck and the pressure tubes (as for all other chuck models so far) and as cap for the access channels. However, the number of connections and the size requirement of the Luer-lock connectors demanded more space on top of the chuck. At the same time, the angle of the access channel needed to be as close as possible to 90° to enable a good fit of the circular O-rings between chuck and chip. The reservoirs were supposed to be embedded in a separate Teflon part (for chemical inertness), which was situated above the chip. The temperature control would be enabled by one or two small Peltier elements placed directly on the backside of the fluidic chip (hence the arrangement of the connection points) whose excess heat would be transferred into the aluminum block that houses the Luer connections, which would work in this way as heat sink. Electric fields could be applied to the connection points via long electrodes inserted through the access holes. This first chuck version had three drawbacks: (i) liquid exchange would require blunt syringe needles that were not available at a sufficient length, (ii) the Peltier elements (even though available at this size) would have caused spatial problems with their wiring and (iii) the access holes. These holes are defined by two angles in space and would need to align with close to micrometer precision across three parts in the chuck, that is, the top part with the connections, the reservoir part and the fluidic chip. Given their length and diameter, this was deemed not feasible during discussions with the manufacturer.
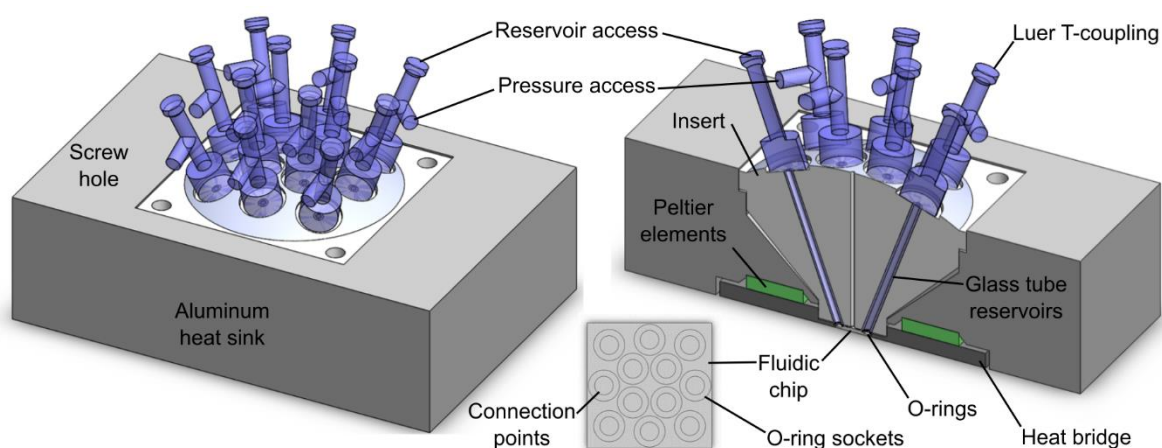

Figure 30. *Chip holder development stage 2.*

The second version of the chuck shown in **Figure 30** retained the concept of angled access holes, but the part that held the Luer-connections and the part with the liquid reservoirs above the chip were merged into one to reduce the alignment challenge. The primary innovation step hereby was the repositioning of the Peltier elements away from the chip by introducing a metal frame in which the fluidic chip would sit and that also would work as a heat conductor (heat bridge). Consequently, the base of the chuck, fashioned in aluminum, would be the heat sink. The removal of the Peltier element from the chip allowed the connection points to be repositioned and increased in size, which also influenced the arrangement of the Luer connectors at the top of the chuck. The appliance of pressure would then happen via Luer T-couplings that would allow access to the reservoirs with the pressure tubes staying connected. The reservoirs were envisioned to be inserted glass tubes, providing excellent chemical resistance. The problems with this chuck version remained to be (i) the angled access holes for the reasons named above and (ii) the relatively complicated central part of the chuck with geometries that are difficult to manufacture.
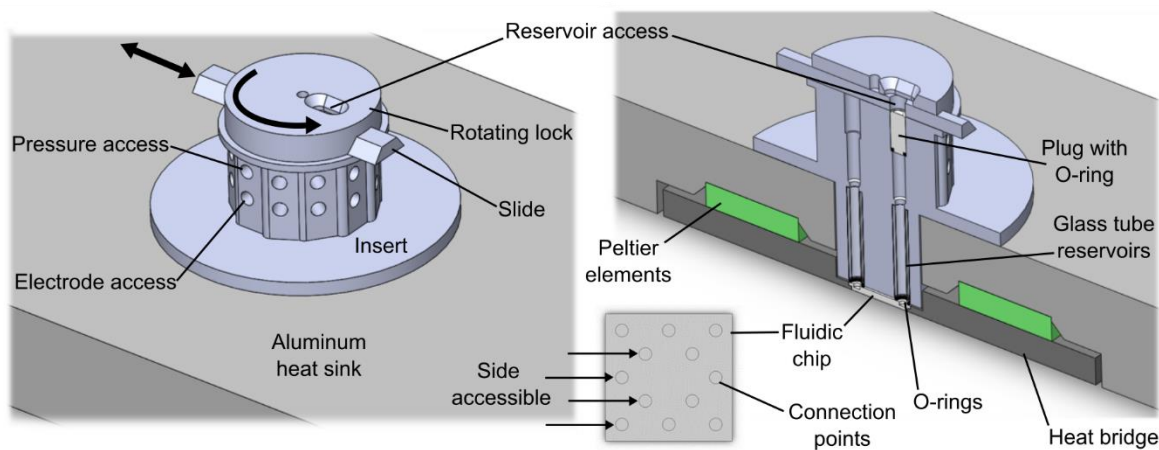
Figure 31. *Chip holder development stage 3.*

This next version (**Figure 31**) kept the principle of the fluidic chip placed in a heat bridge but saw the connection hub totally remodeled. The principle of straight, vertical access holes was enforced here, leading to the problem of how the access holes could be closed to allow pressure to be applied. For this, I thought of a rotating and sliding lock permanently attached to the upper part of the chuck. With this, any access hole could be selected and opened, albeit only one at a time. Sealing of the holes would be possible with a tight enough rotation lock or plugs being set into the access holes. Electrodes and pressure could then enter the reservoirs from the side, which again consisted of inserted glass tubes sealed with O-rings against the fluidic chip. To enable such an access to the reservoirs from the side, the connection points on the chip were once again rearranged, now in a square packing formation. The main drawback of this chuck model was clearly the very complicated locking mechanism, that would have been difficult to keep tight.

Figure 32. *Chip holder development stage 4.*

As shown in **Figure 32**, version 4 was a radical redesign of the chuck. The ideas kept from previous versions where (i) the placement of the fluidic chip in a heat conducting part (heat bridge) with the Peltier elements now placed vertically on the side between the inner heat bridge and the outer frame and (ii) the arrangement of the connection points on the fluidic chip. The idea to access these points via horizontal channels from the side was the basis for a tota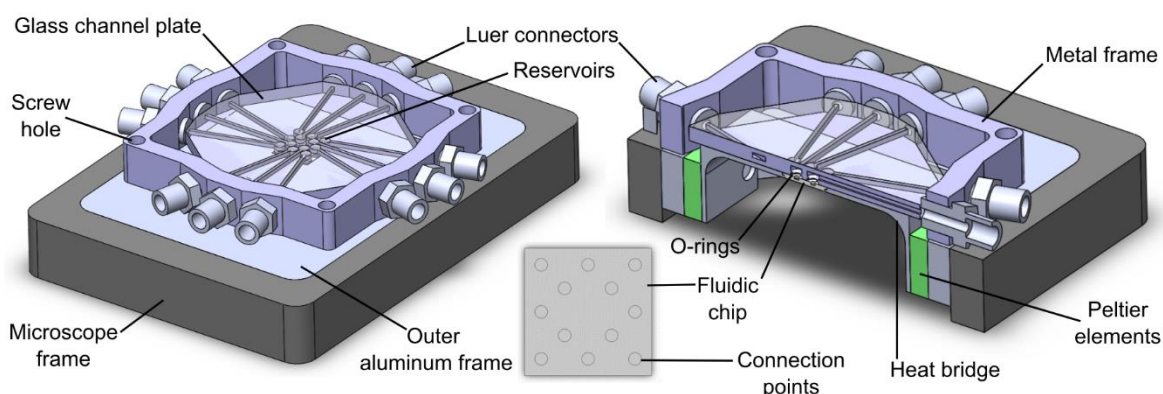l reorientation of the access channels and reservoirs. They were now placed in a horizontal plane just above the backside of the chip, such that there was just enough space for the O-rings. Additionally, they were angled again, but now only in one plane, which made manufacturing easier. Additionally, they were situated in a separate glass channel plate, which was thought to be manufactured like the fluidic chip itself, and which could be replaced separately when needed. The Luer-Lock connectors were placed in an outer frame and would hold the channel plate as they would be screwed in. As an additional benefit and due to the transparency of the channel plate, a facile visual check of the reservoirs and chip connection points would be possible. The model shown in **Figure 32** has also already been adapted to the frame on the table of the inverted microscope (section 5.2.2). While meeting all our requirements and indeed being possible to manufacture, two problems remained. (i) While the reservoirs above the chip could be filled with long (blunt or pointed) syringe needles through the Luer-connectors, the liquid would not be placed in the holes of the chip, but up to 1.5 mm above. This could cause air being trapped between the inserted solution and the chip which would need to be pressed through the fluidic system at first, which can take several minutes even a high applied pressure. (ii) The channel plate would need to be placed rather exactly and firmly, to align with the connection points on the chip but also provide mechanical support for the pressure needed to seal the O-rings. Furthermore, the outer frame with the Luer-connectors has a very specific geometry and the long channels in the thin channel plate are difficult to manufacture. Also, the material of the channel plate is critical, as it needs to be chemically inert while being mechanically robust, transparent and easy to machine. The heat bridge below the chip is relatively large when compared to the fluidic chip, such that more Peltier elements are needed to cool or heat this large volume, which would require a larger heat sink or secondary cooling.
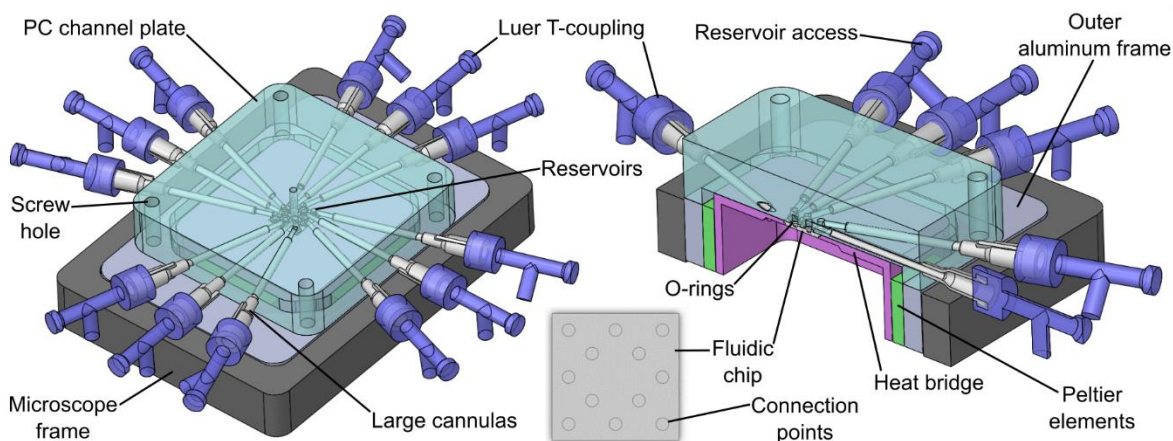
Figure 33. *Chip holder development stage 5.*

The (as of yet) final version of the chip holder is shown in **Figure 33** and explained in much greater detail in **Paper IV,** where I also in detail tested its functions after successfully having manufactured it. This version is very similar to the previous one and has, apart from a simplified geometry of the heat bridge, only one major change concerning the aforementioned channel plate and the Luer-connectors. These parts have been merged into one, such that the mechanical stability of the part that seals the connection to the fluidic chip via the O-rings is ensured. This also decreases the manufacturing effort and complexity of this part, making it easier to create a replacement or different version. Notable is the choice of Luer-connectors. While version 4 was using metal Luer connectors with metric threads, in this version the connection from the 2 mm wide access channels to the Luer-Lock system is simply enabled by using large cannulas for syringes who already have a Luer-Lock adapter at one end. These cannulas are glued into the new channel plate using the outer part of the access channels, such that the syringe needle for liquid exchange (or a long electrode) can be entered into the reservoirs through this cannula. To apply pressure, the idea of using Luer-T-couplings is recycled from version 2. All in all, this solution indeed satisfies all the criteria listed in section 5.1. Nonetheless, it may not be the last version of this kind of fluidic chip holder that we build since there are some features that still could be improved, most of them concerning the channel plate. Among them are:

1. The material of the channel plate. The currently used polycarbonate has a relatively low glass transition temperature[190] of around 150 °C, which limits the temperature range for experiments. It is also incompatible with organic solvents, such as ethanol and acetone[179]. Glass would be optimal but is complicated to manufacture.
2. Inserted cannulas work fine but show signs of mechanical weakness to the torque applied when handling the Luer-connector. Full stainless-steel cannulas with three of them per side linked via a metal bar could solve this problem.
3. The entrapment of air above the holes of the chip when filling the reservoirs with liquids for the first time. This causes delays when starting experiments and also means that subsequent exchange of liquids requires long flushing times to fully remove the previous solution from the reservoir.

5.2.2 Inverted Dark-Field Microscope Setup

The fluidic chip with its nanochannels is indisputably the core of NSM/NSS and its design defines the specific experiment. The chip holder as described above dictates the parameters and variables of the experiment and influences the fluidic design. However, the foundation of any experiment is the instrument used for recording the data, which in my case was either an upright or an inverted dark-field microscope. While such instruments are commercially available, they do not fully satisfy the needs for stability, customizability and nanometer position control. Therefore, I also have been involved in putting together and inverted optical microscope setup optimized for NSM (**Figure 35**).
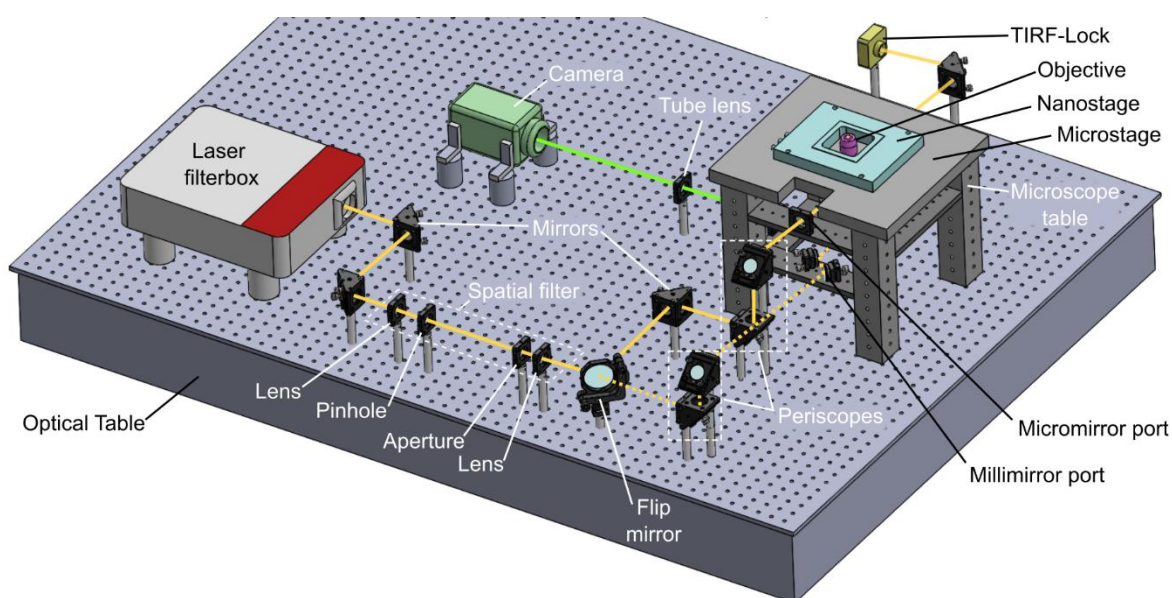
Figure 34. *Inverted dark-field microscope for NSM. The base of this setup is a RM21 with a micro and nanostage from Mad City Labs. The light source is a NKT SuperK supercontinuum laser that generates a broad spectrum via nonlinear effects in a long fiber, such that specific wavelengths can be selected with the filter box mounted on the table. The spatial filter produces a cleaned gaussian beam profile[191]. The scattered light from the sample is recorded with an Andor Zyla 4.2 Plus camera. The illumination path is marked in yellow, with the dashed line indicating the alternative path to the objective (see* **Figure 35***), the green path is the scattered light used to create an image on the camera.*

The base for this instrument is a RM21 Advanced Microscope from Mad City Labs, Madison, Wisconsin, USA. It consists primarily of a four-legged microscope table which carries a micrometer stage operated by a worm drive and a nanometer stage on top using Piezo-elements for positioning, which enables the microscope stage position control to have a spatial resolution of 0.4 nm. The objective lens of the microscope sits in this table under the sample position (see **Figure 34**), such that the sample can be manipulated from above. The light for the illumination is provided by a NKT Varia tunable filter box that allows the selection of wavelengths between 400 nm and 840 nm from a supercontinuum generated by a non-linear optical fiber. The beam of the selected wavelength is directed through a spatial filter to create an even, gaussian beam profile and with that an even illumination of the sample. The light is then directed to two

periscopes, which allow the use of an oil-immersion objective (for example a Nikon MRD01691) or a dark-field objective (for example a Nikon MUE61500) by redirecting the light to small mirrors placed under the respective objectives. **Figure 35** illustrates the light paths for these two cases, which shows that the oil-immersion objective can be used as dark-field objective when the incident light is entering the back-end of the objective at the very edge of the lens. This approach is commonly used for total internal reflection (TIRF) applications[192].
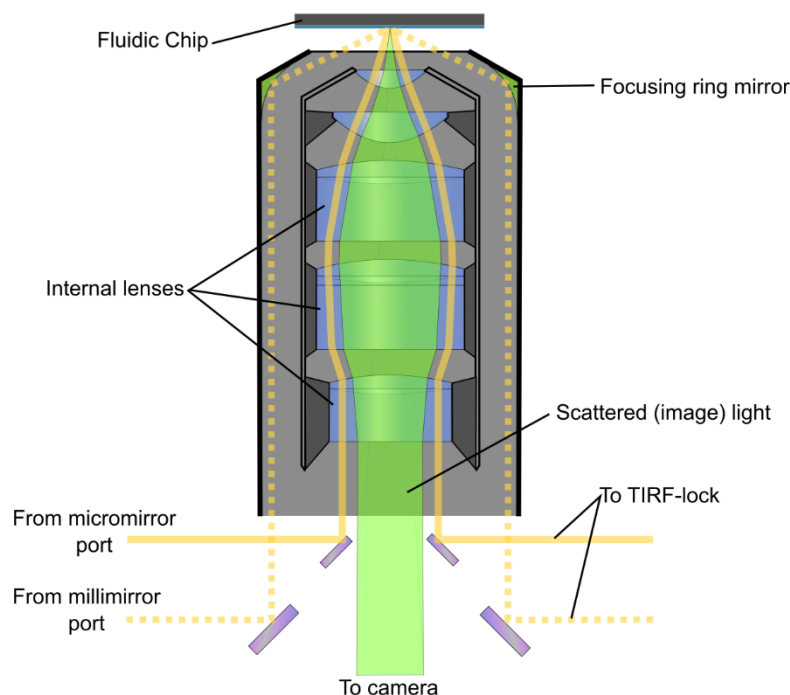
Figure 35. *Light path for an TIR/dark-field objective.* *In this schematic view, both objective types have been joined into one. The continuous yellow line indicates the light path for an TIR objective, where the incident light enters the objective through the same lenses used for image generation from the scattered light (green). Upon exiting the objective, the light is then reflected from the sample and re-enters the objective. The dashed yellow line is the incident light path for a dark-field objective, which often features a separate illumination channel. Here, the light is focused onto the sample via a ring mirror but has also a symmetrical entry and exit path. In both cases, the reflected light can be used to monitor the focus via a TIRF-lock device[193].*

The beam that is reflected from the sample (for both objectives) can be used in a TIRF-Lock[193] (**Figure 34**) that tracks focus drifts during the measurement and corrects them automatically with the help of the nanostage. The light that is scattered from the sample is directed via the objective lens, a mirror and the tube lens onto the chip of an Andor Zyla 4.2 plus CMOS camera, that can record 4.2 megapixel images at 100 fps. This camera was chosen for its outstanding dynamic range, which means that small signal changes can be better detected in a relatively strong signal, as required for NSM and NSS. The overall scattered intensity of a nanochannel is, depending on its geometrical cross section, always stronger than the changes induced by RI changes, such that the ability of the camera to detect small changes in a strong signal defines the resolution of NSM, e.g., in terms of solute concentration in a nanochannel, as of relevance for my work.

In summary, this new microscopy setup dedicated to NSM is the result of the learnings gathered during the work presented in this thesis and the attached papers. While I have been able to already use it for the functionality tests of the new chuck discussed in **Paper IV**, it is still under ongoing development. Once it is fully functional its nanometer-precise sample control, high stability and ultrafast image acquisition possibility combined with the temperature control and electric fields offered by the new chuck, it has great potential to further advance our efforts in single particle catalysis and beyond.

6 SUMMARY AND OUTLOOK

The aim of my work presented in this thesis was to develop and demonstrate an experimental technique with which single, catalytically active nanoparticles could be studied without the need for any direct signal from the particle itself or any indirect probes, such as fluorescence. It is my hope that this thesis, and the results presented in the attached papers, have convinced the reader that I was successful in this quest.

The importance of my mission is given by the facts that (i) nanoparticles produced for catalysis are inherently diverse in their shape and size, and with that in their activity/selectivity, and (ii) that nanoparticles used as catalysts in industry are in the size range of 10 nm or below[63–65], making it therefore challenging to investigate them individually with conventional methods. The background in nanofluidic systems and their fabrication provided by my research group has sparked the idea to use a nanoscale object that is easily visible in a dark-field microscope for this purpose, that is, a nanochannel inside which we can place single catalyst nanoparticles. The underlying physical principle is Mie-scattering from sub-wavelength objects, which connects the scattered intensity of light from a nanochannel to the difference in RI between the fluid in the channel and the surrounding material. Using this dependence of the scattering on the RI difference and changes therein, a new analysis method for femto- to attoliter solution volumes emerged – NSM.

Exploring this method, I laid out analytically how changes in the RI of the nanochannel cause changes in its light scattering intensity. Subsequently, I applied this principle experimentally to detect different concentrations of H_2O_2 in water, and even the diffusion of the former into the latter, using NSM of a single nanochannel (**Paper I**). Furthermore, I demonstrated in the same publication that NSM can be used to detect and count single colloidal Pt particles trapped in a nanochannel, and that these particles can be used for a catalytic reaction. As Pt is a known catalyst for the decomposition[14,85,118–121] of H_2O_2 into H_2O and O_2, my experiments revealed that the colloidal particles generate O_2 in the gas phase in the nanochannels, meaning that the created reaction product became clearly visible with NSM since its RI was greatly different from the surrounding SiO_2. The analysis of the expansion speed of the O_2 bubbles formed, revealed intrinsic differences between individual colloidal particles, and was used to estimate a turnover frequency (TOF) for specific nanoparticles concerning this catalytic reaction. Furthermore, this experiment demonstrated that parallel nanochannels in the field of view of the microscope are ideal to conduct parallel assessments of isolated single catalyst particles at the same conditions. It also showcased that the confinement in a nanochannel indeed is beneficial for the sensitivity of NSM, as reactants and products are not diluted.

Paper II is a significant expansion of the capabilities of NSM, as I demonstrate that spectrally resolving light scattered from nanochannels in NSS essentially enables vis-spectroscopy from femto- to attoliter volumes, similar to well established absorption spectrophotometry used for macroscopic sample volumes. From a mechanistic perspective, the specific light absorption of a molecule causes a corresponding change in the absolute RI, as these two items are connected via the Kramers-Kronig relation that allows the calculation of the real part of the RI from the imaginary part (containing the extinction coefficient) and vice versa. In combination with Mie-theory, I was thus able to extract the molar extinction coefficient (ε) spectra of brilliant blue, allura red and fluorescein from the NSS measurements. In addition, both **Paper I** and **Paper**

II featured experiments that showed a nearly linear relation between the scattering intensity and solute concentration, advertising NSM and NSS as ideal tools for the investigation of molecular changes induced by catalysis on single particles. From the fluidics side, **Paper II** introduced reference nanochannels that made NSS comparable to dual-beam ASP, as they provided a constant point of reference during the spectroscopic scattering measurements, reducing in this way the influence of mechanical drifts and straylight.

Paper III is the culmination of my adventures into nanofluidics and single particle catalysis, as it not only features referenced NSS as method for data acquisition, but it also describes a new and unique use of micro- and nanofluidics to create isolated single-particle batch reactors. This was done by first flushing the nanofluidic system with the reactant solution before a stream of inert gas in the microchannels separated the solution-filled nanochannels from the larger bulk of the solution. In this way, I was able to study the catalytic reduction of fluorescein over a single Au nanoparticle in the presence of sodium borohydride ($NaBH_4$). The spectral resolution provided by NSS allowed a detailed assessment of the different phases of the reaction, and I, e.g., found that the pH in the closed volume of the batch reactor undergoes drastic changes reflected in substantial spectral shifts the scattering peak of the fluorescein NSS spectrum.

With the main goal of my thesis thereby essentially achieved twice, i.e., for H_2O_2 decomposition single trapped colloidal Pt particles in **Paper I** and for fluorescein decomposition on a single Au particle made by electron-beam lithography in **Paper III**, the focus was set on the optimization of the methodology I now have established, by developing a dedicated multifunctional chip holder and dark-field microscopy setup. The chip holder is featured and tested in **Paper IV**, where I demonstrated that we now could regulate the temperature of the fluidic system to investigate, e.g. the temperature dependence of diffusion processes in nanochannels, and that we can apply electric fields to influence the mobility of charged solute species. Furthermore, the fluidic chip design introduced in **Paper IV** had 12 fluidic connection points, which enabled an unparalleled control of the flow of solutions in the micro and nanochannels, with the effect that I was able to exchange and mix two solutions of brilliant blue and fluorescein at will and measure the state of mixing using NSS. Due to the small size of the chips, they also provide a high fabrication yield of 52 chips per 2-inch wafer, which both reduces cost of the entire concept and increases the experimental throughput since the availability of chips is no longer limiting.

Outlook

This thesis presented the development of NSM/NSS for single particle catalysis, starting from the basics of heterogeneous catalysis and ending with the implementation of a new experimental setup. This order might be reversed when future tasks are concerned.

By that I mean that the first goal in the future should be the complete implementation of all learnings and features presented in this thesis and the accompanying papers into the new setup. Especially of interest is here the enabling of spectrally resolved measurements for NSS on the new setup, to have the full capacity of the new microscope available when conducting, for example, experiments with single particle batch reactors, as presented in **Paper III**. Connected to this is of course the full utilization of the new chuck. This could possibly lead to a version 6 that is very close to version 5 presented in **Paper IV** but has the current drawbacks mentioned in section 5.2.1 amended.

From there, the full potential of a fluidic SiO_2/Si chip could be unlocked. This includes the utilization of the 12 connection points provided on each chip to create new micro and nanofluidic systems, adapted to specific experiments. I see great potential in the parallel arrangements of identical but separated nanochannels to provide scalable single particle activity assessment. Furthermore, the idea of implementing accompanying but separated fluidic systems (as used for the reference scheme shown in **Figure 20**) could lead to interesting fluidic switching or flow control, as done in established microfluidics with pressure valves[163] or field effect nanofluidics[189]. Also, multi-phase flows could become very interesting, as they already helped to create batch reactors from nanochannels using liquid and gas flows in concert, as demonstrated in **Paper III**. Would this approach be combined with droplet generation in nanochannels, a high-throughput single particle characterization could be possible, where droplets of reactant solution can be passed over catalytic particles in rapid succession while the solution is analyzed via NSM/NSS.

Furthermore, I would like to highlight that it is currently not possible for us to structurally characterize the lithographic or colloidal nanoparticles placed in the nanochannels. In other words, we know only from analogues investigated on open surfaces how they are expected to look like. While this is sufficient for proof-of-principle experiments, if true single-particle structure function correlations are to be investigated with NSM and NSS, it is critical that the particles in the channel can be structurally characterized before, after and during the reaction. For this, it would be immensely helpful to implement the approaches from ETEM into the fluidic chips by fabricating electron-transparent membranes (e.g. carbon or silicon nitride) at the particle position. This appears to be within reach as nanochannel-like devices are already in use in the field of in situ TEM to study materials in the liquid and gas phase[52,194,195]. In addition to TEM, it would also be great to enable measurements using electromagnetic radiation other than visible light, as for example X-ray approaches have already been demonstrated with in-situ nanoreactors using a commercial available MEMS chips[20]. Members of my research group have already performed first tests of particle-decorated fluidic chips at the MAX IV synchrotron facility.

Apart from the experimental techniques used to characterize catalytic particles, it is of course the particle itself that is of interest. Here, NSM/NSS offers a larger sample range as it is not dependent on specific particle properties. Since no plasmonic response is required, metals other than Au, Ag or Cu can be investigated, as shown for Pt in this work. It also makes it possible to study oxide nanoparticles of, for example, Cu, Fe, Co and Ti[196]. For the same reasons, NSM/NSS will hopefully enable the study of smaller single particles, down to the sub-10 nm size regime, which is the one that is truly technically relevant for industrial applications. I envision this to be possible with the help of nanoscale batch reactors as introduced in **Paper III**, since in this way even the smallest particle can be given enough time to create a detectable change in the RI of the nanochannel.

One specifically interesting idea in this regard could be the colloidal growth of nanoparticles onto nanofabricated seeds that have been placed in the nanochannels. This has been demonstrated on open surfaces[197] and would combine the best of two worlds, i.e., colloidal synthesis and nanofabrication. In this way, it could open new avenues for the investigation of structure-function correlations in catalysis at the single nanoparticle level.

On the smallest scale, that is the actual catalytic reaction performed on the surface of the catalyst, the options for future investigations are extensive as well. The reactions presented in this thesis and in **Paper I** and **III**, namely H_2O_2 decomposition and dye reduction, have been fruitful as model systems for the demonstration of NSM/NSS. The path taken with the former to investigate future energy carriers is nowadays more relevant than ever in the creation of a sustainable society. Apart from H_2O_2, it is of course H_2 that is a very promising candidate in a renewable energy landscape. For this, catalysts are needed that can work in electrolyzers[198–200] to generate H_2, and in fuel cells[201,202] to generate electricity.

In general, I see a broad range of future applications connected to NSM/NSS when the investigation of individual, catalytically active nanoparticles is considered. My methods have the potential to become a great addition to the toolbox of single particle techniques that enable the high-throughput and highly parallelized assessment catalytic activity/selectivity of single nanoparticles. With that, a deeper understanding of the correlation between particle structure and function could be achieved, which hopefully in the long term will lead to the development of better and technologically relevant catalyst materials.

ACKNOWLEDGEMENTS

There are many people that deserve my gratitude for providing the necessary assistance that I needed to stay on track but also to stay happy and healthy.

Of all people, it is my main supervisor Christoph that I need to thank. I would not be in this fortunate situation that I am in now, if you had not accepted me into your group and given me the opportunity to develop my ideas and myself as a person. Thank you for putting up with me, your enthusiasm in an inspiration!

Thanks to my examiner Henrik, not only for his feedback on this thesis but also for the support provided over the years. You are the good soul that keeps the Chemical Physics division together.

A big thanks goes out to my co-supervisor Joachim, as he provided me with the necessary (fluidic) platform to conduct my research. I enjoyed our conversations and regular exchange of chips. I hope that you will have the chance to expand your fabrication to the truly macroscopic world.

Thanks also to my office mate Lova for the nice discussions about everything. I will hopefully pick up Yoga again.

Thanks to Carl for providing the electron microscopy skills that gave my work an extra touch. We need to get a round together again sometimes.

A big thanks in general to the whole Langhammer group and everyone at Chemical Physics for the private and professional discussions at the lunch table and the help provided.

Additionally, thanks to Björn who inspired me to take on a very interesting and wholesome hobby.

In the end, my heartfelt thanks to my family, I am forever in debt to your priceless advice. Thank you for supporting me in my career choices and making it possible to have a place of my own.

BIBLIOGRAPHY

1. Kummer, J. T. Catalysts for automobile emission control. *Prog. Energy Combust. Sci.* **6**, 177–199 (1980).

2. Corma, A. Attempts to Fill the Gap Between Enzymatic, Homogeneous, and Heterogeneous Catalysis. *Catal. Rev.* **46**, 369–417 (2004).

3. Fulhame, E. *An essay on combustion, with a view to a new art of dying and painting. Wherein the phlogistic and antiphlogistic hypotheses are proven erroneous*. (J. Cooper, 1794).

4. Berzelius, J. J. Årsberättelsen om framsteg i fysik och kemi. (1835).

5. Catalyst Market Size, Share & Trends Analysis Report By Raw Material (Chemical Compounds), By Product by Application (Heterogeneous, Homogeneous), By Region, And Segment Forecasts, 2024 - 2030. *Gd. View Res.* **978**-**1**–**6803**, (2024).

6. Chorkendorff, I. & Niemantsverdriet, J. W. *Concepts of modern catalysis and kinetics*. (Wiley-VCH, 2007).

7. Haber, F. & Le Rossignol, R. Über die technische Darstellung von Ammoniak aus den Elementen. *Zeitschrift für Elektrochemie und Angew. Phys. Chemie* **19**, 53–72 (1913).

8. Abe, J. O., Popoola, A. P. I., Ajenifuja, E. & Popoola, O. M. Hydrogen energy, economy and storage: Review and recommendation. *Int. J. Hydrogen Energy* **44**, 15072–15086 (2019).

9. Leeuwen, P. W. N. M. *Homogeneous Catalysis - Understanding the Art*. (Springer Dordrecht, 2004).

10. Jha, M. K. *et al.* Review on hydrometallurgical recovery of rare earth metals. *Hydrometallurgy* **165**, 2–26 (2016).

11. Cheng, N., Zhang, L., Doyle-Davis, K. & Sun, X. Single-Atom Catalysts: From Design to Application. *Electrochem. Energy Rev.* **2**, 539–573 (2019).

12. Jamkhande, P. G., Ghule, N. W., Bamer, A. H. & Kalaskar, M. G. Metal nanoparticles synthesis: An overview on methods of preparation, advantages and disadvantages, and applications. *J. Drug Deliv. Sci. Technol.* **53**, 101174 (2019).

13. Plauck, A., Stangland, E. E., Dumesic, J. A. & Mavrikakis, M. Active sites and mechanisms for H2O2 decomposition over Pd catalysts. *Proc. Natl. Acad. Sci. U. S. A.* **113**, E1973–E1982 (2016).

14. Serra-Maia, R. *et al.* Mechanism and Kinetics of Hydrogen Peroxide Decomposition on Platinum Nanocatalysts. *ACS Appl. Mater. Interfaces* **10**, 21224–21234 (2018).

15. Gao, W., Hood, Z. D. & Chi, M. Interfaces in Heterogeneous Catalysts: Advancing Mechanistic Understanding through Atomic-Scale Measurements. *Acc. Chem. Res.* **50**, 787–795 (2017).

16. An, K. & Somorjai, G. A. Size and Shape Control of Metal Nanoparticles for Reaction Selectivity in Catalysis. *ChemCatChem* **4**, 1512–1524 (2012).

17. Yang, F., Deng, D., Pan, X., Fu, Q. & Bao, X. Understanding nano effects in catalysis. *Natl. Sci. Rev.* **2**, 183–201 (2015).

18. Willets, K. A. & Van Duyne, R. P. Localized Surface Plasmon Resonance Spectroscopy and Sensing. *Annu. Rev. Phys. Chem.* **58**, 267–297 (2007).

19. Koper, M. T. M. Structure sensitivity and nanoscale effects in electrocatalysis. *Nanoscale* **3**, 2054–2073 (2011).

20. Fam, Y. *et al.* A versatile nanoreactor for complementary in situ X-ray and electron microscopy studies in catalysis and materials science. *J. Synchrotron Radiat.* **26**, 1769–1781 (2019).

21. Hartman, T., Geitenbeek, R. G., Wondergem, C. S., Van Der Stam, W. & Weckhuysen, B. M. Operando Nanoscale Sensors in Catalysis: All Eyes on Catalyst Particles. *ACS Nano* (2020).

22. Meirer, F. & Weckhuysen, B. M. Spatial and temporal exploration of heterogeneous catalysts with synchrotron radiation. *Nat. Rev. Mater.* **3**, 324–340 (2018).

23. Vicente, R. A., Neckel, I. T., Sankaranarayanan, S. K. R. S., Solla-Gullon, J. & Fernández, P. S. Bragg Coherent Diffraction Imaging for In Situ Studies in Electrocatalysis. *ACS Nano* **15**, 6129–6146 (2021).

24. Cordes, T. & Blum, S. A. Opportunities and challenges in single-molecule and single-particle fluorescence microscopy for mechanistic studies of chemical reactions. *Nat. Chem.* **5**, 993–999 (2013).

25. Zhou, X. *et al.* Quantitative super-resolution imaging uncovers reactivity patterns on single nanocatalysts. *Nat. Nanotechnol.* **7**, 237–241 (2012).

26. Zhou, X., Choudhary, E., Andoy, N. M., Zou, N. & Chen, P. Scalable Parallel Screening of Catalyst Activity at the Single-Particle Level and Subdiffraction Resolution. *ACS Catal.* **3**, 1448–1453 (2013).

27. Chen, P. *et al.* Spatiotemporal catalytic dynamics within single nanocatalysts revealed by single-molecule microscopy. *Chem. Soc. Rev.* **43**, 1107–1117 (2014).

28. Andoy, N. M. *et al.* Single-Molecule Catalysis Mapping Quantifies Site-Specific Activity and Uncovers Radial Activity Gradient on Single 2D Nanocrystals. *J. Am. Chem. Soc.* **135**, 1845–1852 (2013).

29. Alekseeva, S., Nedrygailov, I. I. & Langhammer, C. Single Particle Plasmonics for Materials Science and Single Particle Catalysis. *ACS Photonics* **6**, 1319–1330 (2019).

30. Albinsson, D. *et al.* Copper catalysis at operando conditions—bridging the gap between single nanoparticle probing and catalyst-bed-averaging. *Nat. Commun.* **11**, 4832 (2020).

31. Liu, S. *et al.* In Situ Plasmonic Nanospectroscopy of the CO Oxidation Reaction over Single Pt Nanoparticles. *ACS Nano* **13**, 6090–6100 (2019).

32. Albinsson, D. *et al.* Operando detection of single nanoparticle activity dynamics inside a model pore catalyst material. *Sci. Adv.* **6**, eaba7678 (2020).

33. Albinsson, D. *et al.* Shedding Light on CO Oxidation Surface Chemistry on Single Pt Catalyst Nanoparticles Inside a Nanofluidic Model Pore. *ACS Catal.* **11**, 2021–2033 (2021).

34.   Larsson, E. M., Langhammer, C., Zorić, I. & Kasemo, B. Nanoplasmonic Probes of Catalytic Reactions. *Science (80-.).* **326**, 1091–1094 (2009).

35.   Dahlin, A. B., Tegenfeldt, J. O. & Höök, F. Improving the Instrumental Resolution of Sensors Based on Localized Surface Plasmon Resonance. *Anal. Chem.* **78**, 4416–4423 (2006).

36.   Taylor, A. B. & Zijlstra, P. Single-Molecule Plasmon Sensing: Current Status and Future Prospects. *ACS Sensors* **2**, 1103–1122 (2017).

37.   Klein Moberg, H., Nedrygailov, I. I., Albinsson, D., Fritzsche, J. & Langhammer, C. Deep-learning enabled online mass spectrometry of the reaction product from a single catalyst nanoparticle. *Nat. Portf.* **In Review**, (2024).

38.   Etchegoin, P. G. & Le Ru, E. C. A perspective on single molecule SERS: Current status and future challenges. *Phys. Chem. Chem. Phys.* **10**, 6079–6089 (2008).

39.   Ding, S. Y., You, E. M., Tian, Z. Q. & Moskovits, M. Electromagnetic theories of surface-enhanced Raman spectroscopy. *Chem. Soc. Rev.* **46**, 4042–4076 (2017).

40.   van Schrojenstein Lantman, E. M., Deckert-Gaudig, T., Mank, A. J. G., Deckert, V. & Weckhuysen, B. M. Catalytic processes monitored at the nanoscale with tip-enhanced Raman spectroscopy. *Nat. Nanotechnol.* **7**, 583–586 (2012).

41.   Langhammer, C., Larsson, E. M., Kasemo, B. & Zorić, I. Indirect Nanoplasmonic Sensing: Ultrasensitive Experimental Platform for Nanomaterials Science and Optical Nanocalorimetry. *Nano Lett.* **10**, 3529–3538 (2010).

42.   Dong, J.-C. *et al.* Direct In Situ Raman Spectroscopic Evidence of Oxygen Reduction Reaction Intermediates at High-Index Pt(hkl) Surfaces. *J. Am. Chem. Soc.* **142**, 715–719 (2020).

43.   Swearer, D. F. *et al.* Heterometallic antenna-reactor complexes for photocatalysis. *Proc. Natl. Acad. Sci. U. S. A.* **113**, 8916–8920 (2016).

44.   Antosiewicz, T. J., Wadell, C. & Langhammer, C. Plasmon-Assisted Indirect Light Absorption Engineering in Small Transition Metal Catalyst Nanoparticles. *Adv. Opt. Mater.* **3**, 1591–1599 (2015).

45.   Zhou, L. *et al.* Light-driven methane dry reforming with single atomic site antenna-reactor plasmonic photocatalysts. *Nat. Energy* **5**, 61–70 (2020).

46.   Vadai, M., Angell, D. K., Hayee, F., Sytwu, K. & Dionne, J. A. In-situ observation of plasmon-controlled photocatalytic dehydrogenation of individual palladium nanoparticles. *Nat. Commun.* **9**, 1–8 (2018).

47.   Hansen, T. W. & Wagner, J. B. Catalysts under Controlled Atmospheres in the Transmission Electron Microscope. *ACS Catal.* **4**, 1673–1685 (2014).

48.   Dunn, G. *et al.* Graphene-Sealed Flow Cells for in Situ Transmission Electron Microscopy of Liquid Samples. *ACS Nano* **14**, 9637–9643 (2020).

49.   van der Wal, L. I., Turner, S. J. & Zečević, J. Developments and advances in in situ transmission electron microscopy for catalysis research. *Catal. Sci. Technol.* **11**, 3634–3658 (2021).

50. Yokosawa, T., Alan, T., Pandraud, G., Dam, B. & Zandbergen, H. In-situ TEM on (de)hydrogenation of Pd at 0.5-4.5bar hydrogen pressure and 20-400°C. *Ultramicroscopy* **112**, 47–52 (2012).

51. Giorgio, S. *et al.* Environmental electron microscopy (ETEM) for catalysts with a closed E-cell with carbon windows. *Ultramicroscopy* **106**, 503–507 (2006).

52. Creemer, J. F. *et al.* Atomic-scale electron microscopy at ambient pressure. *Ultramicroscopy* **108**, 993–998 (2008).

53. Williamson, M. J., Tromp, R. M., Vereecken, P. M., Hull, R. & Ross, F. M. Dynamic microscopy of nanoscale cluster growth at the solid-liquid interface. *Nat. Mater.* **2**, 532–536 (2003).

54. Kraus, T. & de Jonge, N. Dendritic Gold Nanowire Growth Observed in Liquid with Transmission Electron Microscopy. *Langmuir* **29**, 8427–8432 (2013).

55. Vendelbo, S. B. *et al.* Visualization of oscillatory behaviour of Pt nanoparticles catalysing CO oxidation. *Nat. Mater.* **13**, 884–890 (2014).

56. Ghosh, T. *et al.* Periodic structural changes in Pd nanoparticles during oscillatory CO oxidation reaction. *Nat. Commun.* **13**, 2041–1723 (2022).

57. Boyes, E. D., Lagrow, A. P., Ward, M. R., Mitchell, R. W. & Gai, P. L. Single Atom Dynamics in Chemical Reactions. *Acc. Chem. Res.* **53**, 390–399 (2020).

58. Sambur, J. B. & Chen, P. Approaches to single-nanoparticle catalysis. *Annu. Rev. Phys. Chem.* **65**, 395–422 (2014).

59. Xu, W., Zhang, Y. & Chen, T. Single particle nanocatalysis: Fundamentals and applications. in *Single Particle Nanocatalysis: Fundamentals and Applications* 1–289 (2019).

60. Hartman, T., Geitenbeek, R. G., Wondergem, C. S., van der Stam, W. & Weckhuysen, B. M. Operando Nanoscale Sensors in Catalysis: All Eyes on Catalyst Particles. *ACS Nano* **14**, 3725–3735 (2020).

61. Hartman, T., Wondergem, C. S., Kumar, N., van den Berg, A. & Weckhuysen, B. M. Surface- and Tip-Enhanced Raman Spectroscopy in Catalysis. *J. Phys. Chem. Lett.* **7**, 1570–1584 (2016).

62. Chen, P., Xu, W., Zhou, X., Panda, D. & Kalininskiy, A. Single-nanoparticle catalysis at single-turnover resolution. *Chem. Phys. Lett.* **470**, 151–157 (2009).

63. Tsung, C.-K. *et al.* Sub-10 nm Platinum Nanocrystals with Size and Shape Control: Catalytic Study for Ethylene and Pyrrole Hydrogenation. *J. Am. Chem. Soc.* **131**, 5816–5822 (2009).

64. Freund, E., Lynch, J. & Szymanski, R. Small particles in the field of industrial supported catalysts. *Ultramicroscopy* **20**, 107–118 (1986).

65. Farrauto, R. J. Industrial Catalysis: A Practical Guide BT - Handbook of Industrial Chemistry and Biotechnology. in (eds. Kent, J. A., Bommaraju, T. V & Barnicki, S. D.) 1995–2035 (Springer International Publishing, 2017).

66. Cuenya, B. R. Synthesis and catalytic properties of metal nanoparticles: Size, shape, support, composition, and oxidation state effects. *Thin Solid Films* **518**, 3127–3150 (2010).

67. Bacsa, W., Bacsa, R. & Myers, T. Microscopic Origin of the Index of Refraction. in *Optics Near Surfaces and at the Nanometer Scale* 65–83 (Springer International Publishing, 2020).

68. Levin, S. *et al.* A nanofluidic device for parallel single nanoparticle catalysis in solution. *Nat. Commun.* **10**, 4426 (2019).

69. Levin, S. *et al.* Nanofluidic Trapping of Faceted Colloidal Nanocrystals for Parallel Single-Particle Catalysis. *ACS Nano* **16**, 15206–15214 (2022).

70. Špačková, B. *et al.* Label-free nanofluidic scattering microscopy of size and mass of single diffusing molecules and nanoparticles. *Nat. Methods* **19**, 751–758 (2022).

71. Swapnasrita, S. *et al.* Unravelling CO oxidation reaction kinetics on single Pd nanoparticles in nanoconfinement using a nanofluidic reactor and DSMC simulations. *Chem. Eng. Sci. X* **9**, 100088 (2021).

72. Ostwald, W. Vorträge und Diskussionen von der 73. Naturforscherversammlung zu Hamburg: Über Katalyse. *Phys. Zeitschrift* **14**, 313–322 (1902).

73. Seo, C. S. G. & Morris, R. H. Catalytic Homogeneous Asymmetric Hydrogenation: Successes and Opportunities. *Organometallics* **38**, 47–65 (2019).

74. Piontek, A., Bisz, E. & Szostak, M. Iron-Catalyzed Cross-Couplings in the Synthesis of Pharmaceuticals: In Pursuit of Sustainability. *Angew. Chemie Int. Ed.* **57**, 11116–11128 (2018).

75. Dierks, P. *et al.* Ground- and Excited-State Properties of Iron(II) Complexes Linked to Organic Chromophores. *Inorg. Chem.* **59**, 14746–14761 (2020).

76. Haber, F. & Koenig, A. Wissenschaftliche Übersichten: Oxydation des Luftstickstoffes. *Zeitschrift für Elektrochemie und Angew. Phys. Chemie* **16**, 11–25 (1910).

77. Leigh, G. J. Haber-Bosch and Other Industrial Processes BT - Catalysts for Nitrogen Fixation: Nitrogenases, Relevant Chemical Models and Commercial Processes. in (eds. Smith, B. E., Richards, R. L. & Newton, W. E.) 33–54 (Springer Netherlands, 2004).

78. Arrhenius, S. Über die Dissociationswärme und den Einfluss der Temperatur auf den Dissociationsgrad der Elektrolyte. **4U**, 96–116 (1889).

79. Deutschmann, O., Knözinger, H., Kochloefl, K. & Turek, T. Heterogeneous Catalysis and Solid Catalysts. in *Ullmann's Encyclopedia of Industrial Chemistry* (2009).

80. Che, M. Nobel Prize in chemistry 1912 to Sabatier: Organic chemistry or catalysis? *Catal. Today* **218–219**, 162–171 (2013).

81. Nakaya, Y. & Furukawa, S. Catalysis of Alloys: Classification, Principles, and Design for a Variety of Materials and Reactions. *Chem. Rev.* **123**, 5859–5947 (2023).

82. Hughes, A. E., Haque, N., Northey, S. A. & Giddey, S. Platinum Group Metals: A Review of Resources, Production and Usage with a Focus on Catalysts. *Resources* vol. 10 (2021).

83. Taylor, H. S. & Armstrong, E. F. A theory of the catalytic surface. *Proc. R. Soc. London. Ser. A, Contain. Pap. a Math. Phys. Character* **108**, 105–111 (1997).

84. Zhang, Y. *et al.* Sensing the Charge State of Single Gold Nanoparticles via Work Function Measurements. *Nano Lett.* **15**, 51–55 (2015).

85. Serra-Maia, R., Winkler, C., Murayama, M., Tranhuu, K. & Michel, F. M. Abundance and Speciation of Surface Oxygen on Nanosized Platinum Catalysts and Effect on Catalytic Activity. *ACS Appl. Energy Mater.* **1**, 3255–3266 (2018).

86. Talapin, D. V, Lee, J.-S., Kovalenko, M. V & Shevchenko, E. V. Prospects of Colloidal Nanocrystals for Electronic and Optoelectronic Applications. *Chem. Rev.* **110**, 389–458 (2010).

87. Sui, M., Kunwar, S., Pandey, P. & Lee, J. Strongly confined localized surface plasmon resonance (LSPR) bands of Pt, AgPt, AgAuPt nanoparticles. *Sci. Rep.* **9**, 16582 (2019).

88. Munnik, P., de Jongh, P. E. & de Jong, K. P. Recent Developments in the Synthesis of Supported Catalysts. *Chem. Rev.* **115**, 6687–6718 (2015).

89. Karim, W. *et al.* Catalyst support effects on hydrogen spillover. *Nature* **541**, 68–71 (2017).

90. Collins, S. S. E., Cittadini, M., Pecharromán, C., Martucci, A. & Mulvaney, P. Hydrogen Spillover between Single Gold Nanorods and Metal Oxide Supports: A Surface Plasmon Spectroscopy Study. *ACS Nano* **9**, 7846–7856 (2015).

91. Yakoumis, I., Moschovi, A. M., Giannopoulou, I. & Panias, D. Real life experimental determination of platinum group metals content in automotive catalytic converters. *IOP Conf. Ser. Mater. Sci. Eng.* **329**, 12009 (2018).

92. Koczkur, K. M., Mourdikoudis, S., Polavarapu, L. & Skrabalak, S. E. Polyvinylpyrrolidone (PVP) in nanoparticle synthesis. *Dalt. Trans.* **44**, 17883–17905 (2015).

93. Plascencia-Villa, G., Mendoza-Cruz, R., Bazán-Díaz, L. & José-Yacamán, M. Gold Nanoclusters, Gold Nanoparticles, and Analytical Techniques for Their Characterization BT - Nanoparticles in Biology and Medicine: Methods and Protocols. in (eds. Ferrari, E. & Soloviev, M.) 351–382 (Springer US, 2020).

94. Reuter, K. Ab Initio Thermodynamics and First-Principles Microkinetics for Surface Catalysis. *Catal. Letters* **146**, 541–563 (2016).

95. Kim, B. H. *et al.* Critical differences in 3D atomic structure of individual ligand-protected nanocrystals in solution. *Science (80-.).* **368**, 60–67 (2020).

96. Hansen, T. W., DeLaRiva, A. T., Challa, S. R. & Datye, A. K. Sintering of Catalytic Nanoparticles: Particle Migration or Ostwald Ripening? *Acc. Chem. Res.* **46**, 1720–1730 (2013).

97. Hao, R., Fan, Y., Howard, M. D., Vaughan, J. C. & Zhang, B. Imaging nanobubble nucleation and hydrogen spillover during electrocatalytic water splitting. *Proc. Natl. Acad. Sci. U. S. A.* **115**, 5878–6588 (2018).

98. Grunwaldt, J.-D. & Schroer, C. G. Hard and soft X-ray microscopy and tomography in catalysis: bridging the different time and length scales. *Chem. Soc. Rev.* **39**, 4741–4753 (2010).

99. Chee, S. W., Arce-Ramos, J. M., Li, W., Genest, A. & Mirsaidov, U. Structural changes in noble metal nanoparticles during CO oxidation and their impact on catalyst activity. *Nat. Commun.* **11**, (2020).

100. Su, D. Advanced electron microscopy characterization of nanomaterials for catalysis. *Green Energy Environ.* **2**, 70–83 (2017).

101. Egerton, R. F. Electron energy-loss spectroscopy in the TEM. *Reports Prog. Phys.* **72**, 16502 (2009).

102. Fritzsche, J. *et al.* Single Particle Nanoplasmonic Sensing in Individual Nanofluidic Channels. *Nano Lett.* **16**, 7857–7864 (2016).

103. Albinsson, D. *et al.* Operando detection of single nanoparticle activity dynamics inside a model pore catalyst material. *Sci. Adv.* **6**, eaba7678 (2020).

104. Stewart, M. E. *et al.* Nanostructured Plasmonic Sensors. *Chem. Rev.* **108**, 494–521 (2008).

105. Novo, C., Funston, A. M. & Mulvaney, P. Direct observation of chemical reactions on single gold nanocrystals using surface plasmon spectroscopy. *Nat. Nanotechnol.* **3**, 598–602 (2008).

106. Wu, C.-Y. *et al.* High-spatial-resolution mapping of catalytic reactions on single particles. *Nature* **541**, 511–515 (2017).

107. Bonhommeau, S., Cooney, G. S. & Huang, Y. Nanoscale chemical characterization of biomolecules using tip-enhanced Raman spectroscopy. *Chem. Soc. Rev.* **51**, 2416–2430 (2022).

108. Zhang, H., Duan, S., Radjenovic, P. M., Tian, Z.-Q. & Li, J.-F. Core–Shell Nanostructure-Enhanced Raman Spectroscopy for Surface Catalysis. *Acc. Chem. Res.* **53**, 729–739 (2020).

109. Shen, H., Zhou, X., Zou, N. & Chen, P. Single-Molecule Kinetics Reveals a Hidden Surface Reaction Intermediate in Single-Nanoparticle Catalysis. *J. Phys. Chem. C* **118**, 26902–26911 (2014).

110. Zhou, X., Xu, W., Liu, G., Panda, D. & Chen, P. Size-Dependent Catalytic Activity and Dynamics of Gold Nanoparticles at the Single-Molecule Level. *J. Am. Chem. Soc.* **132**, 138–146 (2010).

111. McDonnell-Worth, C. J. & MacFarlane, D. R. Progress towards direct hydrogen peroxide fuel cells (DHPFCs) as an energy storage concept. *Aust. J. Chem.* **71**, 781–788 (2018).

112. Menegazzo, F., Signoretto, M., Ghedini, E. & Strukul, G. Looking for the "dream catalyst" for hydrogen peroxide production from hydrogen and oxygen. *Catalysts* **9**, (2019).

113. Nicoll, W. D. & Smith, A. F. Stability of Dilute Alkaline Solutions of Hydrogen Peroxide. *Ind. Eng. Chem.* **47**, 2548–2554 (1955).

114. Hart, A. B. & Ross, R. A. Catalytic Decomposition of Hydrogen Peroxide Vapour by Equimolar Mixed Oxides. *Nature* **193**, 1175–1177 (1962).

115. Robbins, J. P. *et al.* Dependence of Hydrogen Peroxide Decomposition on the Size of Catalytic Gold Nanoparticles. in *25th North American Catalysis Society Meeting* 2 (NAM, 2017).

116. Bianchi, G., Mazza, F. & Mussini, T. Peroxide Solutions on Platinum , Iridium , Palladium and Gold Surfaces *. *Electrochim. Acta* **7**, 457–473 (1962).

117. Liu, J., Wei, X., Wang, X. & Liu, X. W. High-yield synthesis of ultrathin silica-based nanosheets and their superior catalytic activity in H2O2 decomposition. *Chem. Commun.* **47**, 6135–6137 (2011).

118. Serra-Maia, R., Rimstidt, J. D. & Michel, F. M. Kinetic Effect of Surface Chemisorbed Oxygen on Platinum-Catalyzed Hydrogen Peroxide Decomposition. *Catal. Letters* **151**, 138–146 (2021).

119. Yi, L. *et al.* Carbon-Supported Bimetallic Platinum–Iron Nanocatalysts: Application in Direct Borohydride/Hydrogen Peroxide Fuel Cell. *ACS Sustain. Chem. Eng.* **6**, 8142–8149 (2018).

120. Serra-Maia, R. *et al.* Effect of particle size on catalytic decomposition of hydrogen peroxide by platinum nanocatalysts. *J. Catal.* **373**, 58–66 (2019).

121. Chen, W. & Qu, B. Investigation of a platinum catalyst supported on a hydrogen peroxide-treated carbon black. *Int. J. Hydrogen Energy* **35**, 10102–10108 (2010).

122. Rudnick, R. & Gao, S. Composition of the Continental Crust. Treatise Geochem 3:1-64. *Treatise on Geochemistry* 1–64 (2003).

123. Esmaeili, S. *et al.* Degradation products of the artificial azo dye, Allura red, inhibit esterase activity of carbonic anhydrase II: A basic in vitro study on the food safety of the colorant in terms of enzyme inhibition. *Food Chem.* **213**, 494–504 (2016).

124. Salem, M. A., Al-Ghonemiy, A. F. & Zaki, A. B. Photocatalytic degradation of Allura red and Quinoline yellow with Polyaniline/TiO2 nanocomposite. *Appl. Catal. B Environ.* **91**, 59–66 (2009).

125. Salem, M. A., Abdel-Halim, S. T., El-Sawy, A. E. H. M. & Zaki, A. B. Kinetics of degradation of allura red, ponceau 4R and carmosine dyes with potassium ferrioxalate complex in the presence of H2O2. *Chemosphere* **76**, 1088–1093 (2009).

126. Torres-Pérez, J., Medellín-Castillo, N. & Reyes-López, S. Y. α and γ Alumina Spheres for Azo Dye (Allura Red) Removal from Aqueous Media. *Adsorpt. Sci. Technol.* **2022**, (2022).

127. Ansar, S. M. *et al.* Removal of Molecular Adsorbates on Gold Nanoparticles Using Sodium Borohydride in Water. *Nano Lett.* **13**, 1226–1229 (2013).

128. Alle, M., Lee, S. H. & Kim, J. C. Ultrafast synthesis of gold nanoparticles on cellulose nanocrystals via microwave irradiation and their dyes-degradation catalytic activity. *J. Mater. Sci. Technol.* **41**, 168–177 (2020).

129. Wang, X., Pauli, J., Niessner, R., Resch-Genger, U. & Knopp, D. Gold nanoparticle-catalyzed uranine reduction for signal amplification in fluorescent assays for melamine and aflatoxin B1. *Analyst* **140**, 7305–7312 (2015).

130. Al-Shehri, A. S., Zaheer, Z., Alsudairi, A. M. & Kosa, S. A. Photo-oxidative Decolorization of Brilliant Blue with AgNPs as an Activator in the Presence of K2S2O8and NaBH4. *ACS Omega* **6**, 27510–27526 (2021).

131. Lin, C., Tao, K., Hua, D., Ma, Z. & Zhou, S. Size effect of gold nanoparticles in catalytic reduction of p-nitrophenol with NaBH4. *Molecules* **18**, 12609–12620 (2013).

132. Neal, R. D., Inoue, Y., Hughes, R. A. & Neretina, S. Catalytic Reduction of 4-Nitrophenol by Gold Catalysts: The Influence of Borohydride Concentration on the Induction Time. *J. Phys. Chem. C* **123**, 12894–12901 (2019).

133. Sai, T., Saba, M., Dufresne, E. R., Steiner, U. & Wilts, B. D. Designing refractive index fluids using the Kramers-Kronig relations. *Faraday Discuss.* **223**, 136–144 (2020).

134. Chebotarev, A. N., Bevziuk, K. V, Snigur, D. V & Bazel, Y. R. The brilliant blue FCF ion-molecular forms in solutions according to the spectrophotometry data. *Russ. J. Phys. Chem. A* **91**, 1907–1912 (2017).

135. Seybold, P. G., Gouterman, M. & Callis, J. Calorimetric, photometric and lifetime determinations of fluorescence yields of fluorescein dyes. *Photochem. Photobiol.* **9**, 229–242 (1969).

136. Hooke, R. *Micrographia : or some physiological descriptions of minute bodies made by magnifying glasses. With observations and inquiries thereupon.* (Jo. Martyn, Ja. Allestry, London, 1665).

137. Wang, H., Zhang, T. & Zhou, X. Dark-field spectroscopy: Development, applications and perspectives in single nanoparticle catalysis. *J. Phys. Condens. Matter* **31**, (2019).

138. Huisken, J., Swoger, J., Del Bene, F., Wittbrodt, J. & Stelzer, E. H. K. Optical Sectioning Deep Inside Live Embryos by Selective Plane Illumination Microscopy. *Science (80-.).* **305**, 1007–1009 (2004).

139. Bohren, C. F. & Huffman, D. R. Rayleigh-Gans Theory. *Absorpt. Scatt. Light by Small Part.* 158–165 (2007).

140. Sliney, D. H. What is light? the visible spectrum and beyond. *Eye* **30**, 222–229 (2016).

141. Malitson, I. H. Interspecimen Comparison of the Refractive Index of Fused Silica. *J. Opt. Soc. Am.* **55**, 1205–1209 (1965).

142. Wesołowski, M. & Erecińska, J. Thermal analysis in quality assessment of rapeseed oils. *Thermochim. Acta* **323**, 137–143 (1998).

143. Bashkatov, A. N. & Genina, E. A. Water refractive index in dependence on temperature and wavelength: A simple approximation. *Proc. SPIE* 393–395 (2003).

144. Giguère, P. A. & Geoffrion, P. Refractive index of hydrogen peroxide solutions . A revision. *Can. J. Res.* **27b**, 168–173 (1949).

145. Anderson, B. W. & Payne, C. J. Liquids of High Refractive Index. *Nature* **133**, 66–67 (1934).

146.   Liu, M. *et al.* Dark-field microscopy in imaging of plasmon resonant nanoparticles. *Colloids Surfaces B Biointerfaces* **124**, 111–117 (2014).

147.   Weilin Xu, Yuwei Zhang, T. C. Surface Plasmon Resonance Spectroscopy for Single Particle Nanocatalysis/Reaction. in *Single Particle Nanocatalysis* 145–179 (2019).

148.   Langhammer, C., Kasemo, B. & Zorić, I. Absorption and scattering of light by Pt, Pd, Ag, and Au nanodisks: Absolute cross sections and branching ratios. *J. Chem. Phys.* **126**, (2007).

149.   Michaelides, E. E. Brownian movement and thermophoresis of nanoparticles in liquids. *Int. J. Heat Mass Transf.* **81**, 179–187 (2015).

150.   Yesibolati, M. N. *et al.* Unhindered Brownian Motion of Individual Nanoparticles in Liquid-Phase Scanning Transmission Electron Microscopy. *Nano Lett.* **20**, 7108–7115 (2020).

151.   Kramers-Kronig Relations and Sum Rules in Linear Optics. in *Kramers-Kronig Relations in Optical Materials Research* 27–48 (Springer Berlin Heidelberg, 2005).

152.   Gore, M. Spectrophotometry and Spectrofluorimetry: A Practical Approach. (2000).

153.   Hale, G. M. & Querry, M. R. Optical Constants of Water in the 200-nm to 200-μm Wavelength Region. *Appl. Opt.* **12**, 555–563 (1973).

154.   Jahanbakhsh, A., Wlodarczyk, K. L., Hand, D. P., Maier, R. R. J. & Maroto-Valer, M. M. Review of Microfluidic Devices and Imaging Techniques for Fluid Flow Study in Porous Geomaterials. *Sensors* vol. 20 (2020).

155.   Beebe, D. J., Mensing, G. A. & Walker, G. M. Physics and Applications of Microfluidics in Biology. *Annu. Rev. Biomed. Eng.* **4**, 261–286 (2002).

156.   Whitesides, G. M. The origins and the future of microfluidics. *Nature* **442**, 368–373 (2006).

157.   Ito, T. & Okazaki, S. Pushing the limits of lithography. *Nature* **406**, 1027–1031 (2000).

158.   Basha, I. H., Ho, E. T., Yousuff, C. M. & Hamid, N. H. Towards Multiplex Molecular Diagnosis—A Review of Microfluidic Genomics Technologies. *Micromachines* vol. 8 (2017).

159.   Voeten, R. L. C., Ventouri, I. K., Haselberg, R. & Somsen, G. W. Capillary Electrophoresis: Trends and Recent Advances. *Anal. Chem.* **90**, 1464–1481 (2018).

160.   François, I., Sandra, K. & Sandra, P. Comprehensive liquid chromatography: Fundamental aspects and practical considerations—A review. *Anal. Chim. Acta* **641**, 14–31 (2009).

161.   Stock, R. & Rice, C. B. F. Gas Chromatography BT - Chromatographic Methods. in 177–278 (Springer US, 1974).

162.   Niculescu, A.-G., Chircov, C., Bîrcă, A. C. & Grumezescu, A. M. Fabrication and Applications of Microfluidic Devices: A Review. *International Journal of Molecular Sciences* vol. 22 (2021).

163. Unger, M. A., Chou, H.-P., Thorsen, T., Scherer, A. & Quake, S. R. Monolithic Microfabricated Valves and Pumps by Multilayer Soft Lithography. *Science (80-.).* **288**, 113–116 (2000).

164. Oh, K. W. Lab-on-chip (LOC) devices and microfluidics for biomedical applications. in *Woodhead Publishing Series in Biomaterials* 150–171 (Woodhead Publishing, 2012).

165. Maeki, M., Yamaguchi, H., Tokeshi, M. & Miyazaki, M. Microfluidic Approaches for Protein Crystal Structure Analysis. *Anal. Sci.* **32**, 3–9 (2016).

166. Liu, Y., Sun, L., Zhang, H., Shang, L. & Zhao, Y. Microfluidics for Drug Development: From Synthesis to Evaluation. *Chem. Rev.* **121**, 7468–7529 (2021).

167. Yin, H. & Marshall, D. Microfluidics for single cell analysis. *Curr. Opin. Biotechnol.* **23**, 110–119 (2012).

168. Zhu, P. & Wang, L. Passive and active droplet generation with microfluidics: a review. *Lab Chip* **17**, 34–75 (2017).

169. Solsona, M. *et al.* Microfluidics and catalyst particles. *Lab Chip* **19**, 3575–3601 (2019).

170. Bu, Y., Niemantsverdriet, J. W. H. & Fredriksson, H. O. A. Cu Model Catalyst Dynamics and CO Oxidation Kinetics Studied by Simultaneous in Situ UV-Vis and Mass Spectroscopy. *ACS Catal.* **6**, 2867–2876 (2016).

171. Yu, X.-Y. In situ, in vivo, and in operando imaging and spectroscopy of liquids using microfluidics in vacuum. *J. Vac. Sci. Technol. A* **38**, 40804 (2020).

172. Ghazal, A. *et al.* Recent advances in X-ray compatible microfluidics for applications in soft materials and life sciences. *Lab Chip* **16**, 4263–4295 (2016).

173. Zhdanov, V. P., Zorić, I. & Kasemo, B. Plasmonics: Heat transfer between metal nanoparticles and supporting nanolayers. *Phys. E Low-Dimensional Syst. Nanostructures* **46**, 113–118 (2012).

174. Eijkel, J. C. T. & Berg, A. van den. Nanofluidics: what is it and what can we expect from it? *Microfluid. Nanofluidics* **1**, 249–267 (2005).

175. Daiguji, H. Nanofluidics. in *Comprehensive Nanoscience and Technology* 315–338 (Academic Press, 2011).

176. Robin, P. & Bocquet, L. Nanofluidics at the crossroads. *J. Chem. Phys.* **158**, 160901 (2023).

177. Schoch, R. B., Han, J. & Renaud, P. Transport phenomena in nanofluidics. *Rev. Mod. Phys.* **80**, 839–883 (2008).

178. Bocquet, L. & Charlaix, E. Nanofluidics, from bulk to interfaces. *Chem. Soc. Rev.* **39**, 1073–1095 (2010).

179. Jankowski, P., Ogończyk, D., Lisowski, W. & Garstecki, P. Polyethyleneimine coating renders polycarbonate resistant to organic solvents. *Lab Chip* **12**, 2580–2584 (2012).

180. Gungor, T., Gungor, E. & Saka, B. Fast and interference fringe independent optical characterization of zinc oxide nano thin films using model-based genetic algorithm for optoelectronic applications. *Nanomater. Nanotechnol.* **6**, 1–7 (2016).

181. Aspnes, D. E. & Studna, A. A. Dielectric functions and optical parameters of Si, Ge, GaP, GaAs, GaSb, InP, InAs, and InSb from 1.5 to 6.0 eV. *Phys. Rev. B* **27**, 985–1009 (1983).

182. Bhalla, V., Carrara, S., Stagni, C. & Samorì, B. Chip cleaning and regeneration for electrochemical sensor arrays. *Thin Solid Films* **518**, 3360–3366 (2010).

183. Dersoir, B., de Saint Vincent, M. R., Abkarian, M. & Tabuteau, H. Clogging of a single pore by colloidal particles. *Microfluid. Nanofluidics* **19**, 953–961 (2015).

184. Massenburg, S. S., Amstad, E. & Weitz, D. A. Clogging in parallelized tapered microfluidic channels. *Microfluid. Nanofluidics* **20**, 94 (2016).

185. Bischof, D., Kahl, M. & Michler, M. Laser-assisted etching of borosilicate glass in potassium hydroxide. *Opt. Mater. Express* **11**, 1185–1195 (2021).

186. Chen, L. & Yu, D. Investigation of low-cost through glass vias formation on borosilicate glass by picosecond laser-induced selective etching. *J. Mater. Sci. Mater. Electron.* **32**, 16481–16493 (2021).

187. Napoli, M., Eijkel, J. C. T. & Pennathur, S. Nanofluidic technology for biomolecule applications: a critical review. *Lab Chip* **10**, 957–985 (2010).

188. Alizadeh, A., Hsu, W.-L., Wang, M. & Daiguji, H. Electroosmotic flow: From microfluidics to nanofluidics. *Electrophoresis* **42**, 834–868 (2021).

189. Prakash, S. & Conlisk, A. T. Field effect nanofluidics. *Lab Chip* **16**, 3855–3865 (2016).

190. Sehrawat, M. *et al.* Glass Transition Temperature Measurement of Polycarbonate Specimen by Dynamic Mechanical Analyser Towards the Development of Reference Material. *MAPAN* **37**, 517–527 (2022).

191. Celliers, P. M. *et al.* Spatial filter pinhole for high-energy pulsed lasers. *Appl. Opt.* **37**, 2371–2378 (1998).

192. Poulter, N. S., Pitkeathly, W. T. E., Smith, P. J. & Rappoport, J. Z. The Physical Basis of Total Internal Reflection Fluorescence (TIRF) Microscopy and Its Cellular Applications BT - Advanced Fluorescence Microscopy: Methods and Protocols. in 1–23 (Springer New York, 2015).

193. Nong, D. *et al.* Integrated multi-wavelength microscope combining TIRFM and IRM modalities for imaging cellulases and other processive enzymes. *Biomed. Opt. Express* **12**, 3253–3264 (2021).

194. Van Omme, J. T. *et al.* Liquid phase transmission electron microscopy with flow and temperature control. *J. Mater. Chem. C* **8**, 10781–10790 (2020).

195. Pu, S., Gong, C. & Robertson, A. W. Liquid cell transmission electron microscopy and its applications. *R. Soc. Open Sci.* **7**, (2020).

196. Pal, J. & Pal, T. Faceted metal and metal oxide nanoparticles: design, fabrication and catalysis. *Nanoscale* **7**, 14159–14190 (2015).

197. Preston, A. S., Hughes, R. A., Demille, T. B., Rey Davila, V. M. & Neretina, S. Dewetted nanostructures of gold, silver, copper, and palladium with enhanced faceting. *Acta Mater.* **165**, 15–25 (2019).

198. Shiva Kumar, S. & Himabindu, V. Hydrogen production by PEM water electrolysis – A review. *Mater. Sci. Energy Technol.* **2**, 442–454 (2019).

199. Ursua, A., Gandia, L. M. & Sanchis, P. Hydrogen Production From Water Electrolysis: Current Status and Future Trends. *Proc. IEEE* **100**, 410–426 (2012).

200. Chi, J. & Yu, H. Water electrolysis based on renewable energy for hydrogen production. *Chinese J. Catal.* **39**, 390–394 (2018).

201. Staffell, I. *et al.* The role of hydrogen and fuel cells in the global energy system. *Energy Environ. Sci.* **12**, 463–491 (2019).

202. Edwards, P. P., Kuznetsov, V. L., David, W. I. F. & Brandon, N. P. Hydrogen and fuel cells: Towards a sustainable energy future. *Energy Policy* **36**, 4356–4362 (2008).